Experimental Methodologies to Study Fretting Fatigue Damage and Crack Initiation

Saosometh Chhith

Promotoren: prof. dr. ir. W. De Waele, prof. dr. ir. P. De Baets
Proefschrift ingediend tot het behalen van de graad van
Doctor in de ingenieurswetenschappen: werktuigkunde-elektrotechniek

UNIVERSITEIT
GENT

Vakgroep Elektrische Energie, Metalen, Mechanische Constructies en Systemen
Voorzitter: prof. dr. ir. L. Dupré
Faculteit Ingenieurswetenschappen en Architectuur
Academiejaar 2017 - 2018

ISBN 978-94-6355-071-0
NUR 978, 950
Wettelijk depot: D/2017/10.500/106

Promotors

Prof. dr. ir. Wim De Waele

Prof. dr. ir. Patrick De Baets

Ghent University

Faculty of Engineering and Architecture

Department of Electrical Energy, Metals, Mechanical Constructions and Systems

Examination Committee

Prof. Gert De Cooman (Chair)

Prof. Roumen Petrov

Prof. Gábor Kalácska

Dr. Reza Hojjati Talemi

Prof. Dieter Fauconnier (Secretary)

Research Institute

Ghent University

Faculty of Engineering and Architecture

Department of Electrical Energy, Metals, Mechanical Constructions and Systems

Laboratory Soete

Technologiepark 903

B-9052 Zwijnaarde

Belgium

Tel. +32 9 331 04 76

Fax. +32 9 331 04 90

Saosometh.Chhith@ugent.be

www.soetelaboratory.ugent.be

"Dare to Change"

……

Acknowledgements

Human rights are great but it is even better to have human responsibilities in a society. I believe that to upgrade human rights to human responsibilities is to cultivate virtue whose mother is gratitude. At the beginning of this dissertation, I would like to express my gratitude (to any extent) for everything I have faced during the period of my PhD.

First of all, I would like to express my sincere thanks to the European Union for organizing multiple Erasmus Mundus projects for non-European students to experience education, research, and daily life in Europe. Particularly, I myself got the chance under Techno II program found by Université Paul Sabatier de Toulouse and other partner universities. The grant was not possible without Ghent University as a host, so thanks to my two promoters, Prof. Wim De Waele and Prof. Patrick De Baets for accepting me as a PhD student in their department. Besides, Prof. De Waele has spent time and patience to guide, follow up, and clarify the objectives of the project throughout the whole period. I have been impressed and inspired by problems solving and critical thinking skills of Prof. De Baets some of which I could learn and use in time of subsequent difficulties. Furthermore, the two professors offered a financial support for one semester each during the fourth year after the Techno II scholarship was finished at the end of the first three years.

I am in debt of gratitude to my colleagues at the Soete Laboratory for giving any needed assistance.

- Wouter Ost for putting in order the hydraulic system, a discussion on machining feasibility, and for training and fixing the MTS software.
- Johan Van Den Bossche for machining all the required specimens and an idea for optimizing the fretting fatigue test rig to apply a better normal load.
- Hans Van Severen for a lot of practical works related to ESH 100 kN machine like changing the grips, frequent assemble and dismantle the fretting fixture.

- Chris Bonne for preparing the strain gauge, training an electric generator for testing the triggering system of the infrared camera and fixing other electronic components.
- Jonathan Vancoillie for managing the server, softwares and internet of all the computers in the laboratory.
- Georgette D'Hondt for assisting most of the administrative work.

Thanks to my research fellows: Diego, Jules, Sameera, Kaveh, Adam, Klara, Levente, Kannaki, Vannessa, Hannan, Jacob, Yeczain, Tongyan, Nahuel, Timothy, Koen, Stijn, Jan, Dieter, Karen, Phuc, Loc, Truong, Cuong, Nadeem, Zaman, Reza, Saeedeh, Ni, Jeff, and Kyvia for sharing different cultures, scientific discussions, several trips and social activities.

The experimental work could not be finalized without the assistance of Michel De Waele and Gert Oost at the Belgian Welding Institute for performing the optical microscopy during crack inspection of the samples. This includes cutting, grinding, polishing, and measuring the crack length.

I am very grateful to an exchange PhD student, Mr. Mizukami Koichi, from Tokyo Institute of Technology for giving a guidance on conventional lock-in signal processing. The discussion has led to explore the other algorithms in the signal processing world.

I would like to thanks the Institute of Technology of Cambodia and the Ministry of Education, Youth, and Sports of Cambodia for giving me a break permit to continue the PhD study.

Finally, thanks to my whole family: parents (Mr. POR Bunhak and Mrs HENG Vary), grandparents, siblings, all relatives, and all the Cambodian people for their loving kindness and sincere compassion. I could keep my motivation and commitment to challenge the difficulties only due to their presence and sacrifice.

Saosometh Chhith *Ghent, 2017*

Summary

Fretting, a problem of multiaxial stress and steep stress gradient in the vicinity of a contact zone, is a complex damage process characterized by a combination of wear, corrosion and cracking. Fatigue lifetime can be significantly reduced when it is combined with fretting. Fretting originates from micro-slip induced by two connected surfaces subjected to vibration. This has been found to happen for mechanical joints such as bolts, rivets, dovetails, etc. Laboratory simulation of the phenomenon is done on the basis of coupon scale experiments (a standard dog-bone specimen against a fretting pad) to develop analytical and numerical models for understanding and describing the mechanics of fretting fatigue. Even though the most common contact type in real fretting fatigue problems is a complete contact, typically a Hertzian contact is used for the coupon scale test because of available contact solutions. More specifically, it is a line contact when the specimen contact surface is plane and the pad contact surface is cylindrical. A pronounced size effect has been observed in laboratory tests for several metals like high strength steel, aluminium alloy and titanium alloy. The size effect refers to a shift in lifetime from a few hundred thousand cycles to infinite below a certain contact area despite the fact that the stress magnitude is kept constant.

Fretting fatigue lifetime is divided into two main proportions: crack initiation and crack propagation. It is much more challenging to understand the initiation stage than the propagation stage, as the damage process takes place in a closed contact between two interacting bodies where sensors cannot be installed, and optical techniques cannot be used for visualization. Analytical and numerical models for prediction of crack initiation lifetime are typically validated based on total lifetime, measured during the experiment, from which crack propagation time determined from scanning electron microscope (SEM) analysis or from an analytical solution is subtracted. Those models can also be validated based on a destructive method which requires the test to be stopped followed by an inspection of the sample with microscopy. However, this method does not allow the test to be continued if a crack is not found. To the author's best knowledge, only the potential drop and X-ray techniques allow to detect a short crack down to $50\ \mu m$ and 100

μm, respectively. In addition to the experimental difficulty, the size effect raises several questions on the validity of the developed models for crack initiation that are mostly based on a multiaxial fatigue parameter which is a stress-based approach. On the other hand, once a crack is initiated to a certain length, a fracture mechanics based approach allows to determine the stress intensity factor at the crack tip so the crack propagation of fretting fatigue becomes similar to plain fatigue.

Infrared thermography is utilized as contactless and on-line technique to tackle the experimental challenge. It has been evaluated as the best candidate among other non-destructive techniques to detect hidden fretting damage in riveted lap joints, and its potential to study material behaviour under different types of cyclic load has been reported. The temperature response of materials subjected to cyclic loads can be decomposed into three contributions: self-heating of the materials, the first harmonic, and the second harmonic. The first harmonic corresponds to the linear response, i.e. purely thermoelastic effect. The temperature rise of the specimen expressed by the second harmonic is created by the inelastic or non-linear effect due to damage of the material. A clear relationship between the temperature rise of materials and their fatigue limit as well as their *S-N* curve has been demonstrated. Generation of heat caused by crack initiation also influences the stabilized mean temperature regime during fatigue tests. Instead of using the temperature rise of the material, i.e. the *D.C.* component, the *A.C.* components of the temperature response are also linked to damage and crack initiation time in both plain fatigue and plain fretting tests.

Two methodologies are developed based on infrared thermography. The first one is an off-line method for rapid determination of the fretting fatigue limit. The second one is an on-line detection methodology for fretting fatigue crack initiation. Fretting fatigue tests are performed using an optimized in-house test set-up and monitored by an infrared camera. In the first methodology, a stepwise block loading is adopted from a plain fatigue approach. The temperature at four regions of interest on the specimen surface for each loading block is analysed in the frequency domain with a Matlab FFT algorithm. Two important regions are the left and right contact zones, while the other two regions are references above and below the contact zones. The duration of the test is rather short; only a few hours. The highest loading block for which the corresponding second harmonic effect at either region of interest is not present is considered to be the fretting fatigue limit. For the second methodology, fretting fatigue tests are run until crack initiation is indicated on-line. Initiation is defined to correspond to an increase of the thermoelastic temperature amplitude from the horizontal stabilized regime with a value larger than the filtered signal-to-noise level of *2 mK*. This parameter is extracted on-line from raw temperature data of the four regions of interest with a lock-in or FFT algorithm available in Matlab. The data is acquired on-line with a Matlab script of the current infrared camera model, ImageIR8300. The evolution of the first harmonic temperature amplitude

contains three stages: running-in, stabilization, and crack propagation. The test needs to be stopped immediately after the stabilization for off-line crack inspection.

The fretting fatigue limit of two metals, an aluminium alloy and a cold drawn structural steel, is rapidly determined based on the second harmonic effect. These limits are verified to correspond to infinite lifetime, i.e. the specimens remain intact at 10^7 *cycles* in separate tests. The moment of crack initiation can be determined on-line by the thermoelastic temperature amplitude, and the corresponding crack length is in the range of *130-220 μm*. The crack initiation and propagation times can be discriminated by using the evolution of the thermoelastic effect and continuing the test until final rupture of the specimen. For both materials, the proportion, N_i/N_f, is around *60 %* in average. The on-line crack detection method is applied to fretting fatigue of the aluminium alloy with a change of contact type from line to elliptical contact. The detection threshold is found to be around *200 μm*.

The two methodologies are extended to fatigue tests of a bent high strength steel specimen with very satisfactory results. The fatigue limit of the bent specimen can be determined rapidly based on the second harmonic effect, and the crack initiation time is measured on-line with a detection threshold of *54 μm*. This thermographic method is shown to offer better accuracy than the conventional method used which is based on monitoring the cross-head displacement of the testing machine.

The thermographic methodologies give promising results to study fretting fatigue damage and crack initiation. For the fatigue limit determination, it saves a lot of time and specimens compared to the conventional method. The accuracy can be further improved by narrowing down the difference in stress level of the loading blocks. A step beyond the state of the art for infrared thermography is the on-line data acquisition and processing for crack initiation detection. The detection threshold is within the range reported for an off-line technique based on SEM, but larger than the potential drop technique. However, the experimental preparation is very simple compared to the potential drop method which sometimes requires complex calibration. The detection threshold can also be further improved with a better lens and changing the fatigue ratio to *R=-1*. In addition to that, the thermographic methodologies can be easily extended to fretting fatigue of different materials and contact types and even to fatigue tests of the bent specimen. The experimental results in this thesis can be used to extend the understanding of the mechanics of fretting fatigue, particularly the crack initiation stage and the size effect.

Samenvatting

(Dutch Summary)

Fretting vermoeiing, een probleem van multiaxiale spanning en een steile spanningsgradiënt in de nabijheid van de contactzone, is een complex schadeproces dat wordt gekenmerkt door een combinatie van slijtage, corrosie en scheuren. Vermoeiingslevensduur kan aanzienlijk worden verminderd in combinatie met fretting. Fretting vermoeiing is afkomstig van micro-slip tussen twee aaneengesloten oppervlakken als een gevolg van trillingen. Dit schadefenomeen werd vastgesteld voor diverse mechanische verbindingen zoals bouten, klinknagels, zwaluwstaart-verbindingen, enz. Simulatie van dit fenomeen op labo-schaal gebeurt typisch op basis van coupon experimenten (fretting pad in contact met een gestandaardiseerd vermoeiingsspecimen) met het doel om analytische of numerieke modellen te ontwikkelen die toelaten om de mechanica van fretting vermoeiing te beschrijven. Hoewel het meest voorkomende contacttype in ingenieurstoepassingen een volledig contact is, wordt typisch een Hertziaans contact gebruikt voor de coupon test omwille van beschikbare vergelijkingen voor het contactprobleem. Meer specifiek betreft het een lijncontact wanneer het contactvlak van het proefstuk vlak is en dit van de pad cilindrisch. In laboproeven werd een uitgesproken schaaleffect waargenomen voor verschillende metalen zoals hoogwaardig staal, aluminium- en titaniumlegering. Het schaaleffect verwijst naar een plotse toename in levensduur van een paar honderdduizend cycli tot oneindig onder een bepaalde contactgrootte, dit ondanks het feit dat de spanning constant is gehouden.

De levensduur in fretting vermoeiing kan opgedeeld worden in twee delen: scheurinitiatie en scheurpropagatie. Het is veel uitdagender om de initiatiefase te bestuderen in vergelijking met de voortplantingsfase. Dit omdat het schadeproces plaatsgrijpt in een gesloten contact waar sensoren niet kunnen worden geïnstalleerd en welke niet toelaat om optische technieken in te zetten voor visualisatie van het schadeproces. Analytische en numerieke modellen voor het voorspellen van initiatie-levensduur worden typisch gevalideerd op basis van de totale levensduur, gemeten tijdens het

experiment, waarvan de tijd voor scheurpropagatie, bepaald op basis van SEM-onderzoek of op basis van een analytische oplossing, wordt afgetrokken. Deze modellen kunnen ook worden gevalideerd op basis van een destructieve methode waarbij de test wordt gestopt, gevolgd door een inspectie van het specimen met behulp van microscopie. Deze methode laat echter niet om de test verder te zetten als er geen scheur is gevonden. Voor zover de auteur heeft kunnen achterhalen, laat enkel de potentiaalval-methode toe om een korte scheur, tot 50 µm, te detecteren. Naast de experimentele uitdagingen, roept ook het schaaleffect meerdere vragen op omtrent de juistheid van de ontwikkelde modellen voor scheurinitiatie die meestal spanningsgebaseerd zijn. Daarentegen, zodra een scheur een bepaalde lengte bereikt, is het mogelijk om op basis van de breukmechanica een spanningsintensiteitsfactor te berekenen, en wordt de scheurpropagatie in fretting vermoeiing vergelijkbaar met conventionele vermoeiing.

In dit werk wordt infrarood thermografie gebruikt als contactloze en on-line techniek om de experimentele uitdagingen aan te pakken. In de literatuur werd deze techniek beoordeeld als de best mogelijke niet-destructieve techniek om verborgen fretting schade in geklonken verbindingen te detecteren. Ook is de mogelijkheid om materiaalgedrag onder verschillende types cyclische belasting te bestuderen uitgebreid gerapporteerd. De temperatuurontwikkeling in materialen die onderworpen zijn aan cyclische belasting kan worden opgedeeld in drie bijdragen: zelfopwarming, eerste harmonische en tweede harmonische. De eerste harmonische komt overeen met de lineaire respons, ofwel puur thermoelastisch effect. De temperatuurstijging van het specimen uitgedrukt door de tweede harmonische is het inelastisch of niet-lineair effect ten gevolge van schade aan het materiaal. Er is door meerdere onderzoekers aangetoond dat er een duidelijk verband bestaat tussen de temperatuurstijging van materialen en hun vermoeiingslimiet, alsook hun S-N-curve. Opwekking van warmte veroorzaakt door scheurinitiatie beïnvloedt ook de gestabiliseerde waarde van de gemiddelde temperatuur tijdens vermoeiingsproeven. In plaats van gebruik te maken van de temperatuurstijging van het materiaal, dat wil zeggen de D.C.-component, kunnen ook de A.C.-componenten van het temperatuurverloop gekoppeld worden aan schade en tijd voor scheurinitiatie in zowel pure vermoeiing als pure fretting.

Twee methodologieën op basis van infrarood thermografie werden ontwikkeld. De eerste is een off-line methode voor het versneld bepalen van de fretting-vermoeiinglimiet. De tweede is een on-line methode voor de detectie van scheurinitiatie in fretting vermoeiing. Fretting vermoeiingsproeven zijn uitgevoerd met behulp van een geoptimaliseerde proefstand en een infrarood camera voor monitoring. In de eerste methode wordt een stapsgewijze blokbelasting opgelegd, zoals eerder toegepast voor conventionele vermoeiing. Een analyse van de temperatuur in vier interessegebieden aan het oppervlak van het specimen is uitgevoerd in het frequentiedomein met behulp van een Matlab FFT-algoritme en dit voor elke

blokbelasting. De twee belangrijkste zones bevinden zich ter hoogte van het linker en rechter contact, terwijl de andere twee zones gekozen werden voor referentiemetingen boven en onder de contactzones. De duur van het volledige experiment is slechts een paar uur. De maximale belasting waarvoor het tweede harmonische effect in een interessegebied niet aanwezig is, wordt beschouwd als de fretting-vermoeiinglimiet. Voor de tweede methodologie zijn de vermoeiingsproeven uitgevoerd tot het ogenblik van on-line indicatie van scheurinitiatie. Het initiatiecriterium is gedefinieerd als het ogenblik waarop een toename in amplitude van de thermo-elastische temperatuur (in gestabiliseerd regime) wordt vastgesteld die groter is dan het gefilterde signaal-over-ruis niveau gelijk aan 2 mK. Deze parameter wordt on-line bepaald uit de onbewerkte temperatuurdata van de vier interessegebieden op basis van een lock-in of FFT-algoritme beschikbaar in Matlab. De evolutie van de amplitude van de eerste harmonische bevat drie fasen: aanloop, stabilisatie en scheurpropagatie. Onmiddelijk na de stabilisatie moet de test gestopt worden voor off-line inspectie.

De fretting-vermoeiinglimiet van twee metalen, een aluminiumlegering en een koudgetrokken staal is versneld bepaald op basis van de tweede harmonische. Er is aangetoond dat deze limieten corresponderen met een oneindige levensduur, d.w.z. de specimens blijven intact na 107 cycli. Het moment van scheurinitiatie kan on-line bepaald worden op basis van de amplitude van de thermo-elastische temperatuur en de corresponderende scheurlengte varieert van 130 tot 220 µm. De duur voor scheurinitiatie en -propagatie kunnen bepaald worden door analyse van de evolutie van het thermo-elastisch effect tot de uiteindelijke breuk van het specimen. Voor beide metalen is de verhouding Ni/Nf gemiddeld ongeveer 60%. De on-line methode voor scheurdetectie methode is toegepast om fretting vermoeiing van de aluminiumlegering te bestuderen in het geval van een elliptisch contact. De drempelwaarde van de scheurinitiatie is bepaald op ongeveer 200 µm.

Het toepassingsgebied van de twee methodologieën is met succes uitgebreid tot vermoeiingsproeven op gebogen specimens vervaardigd uit hoog-sterkte staal. De vermoeiingslimiet van deze gebogen proefstukken kan versneld bepaald worden op basis van de tweede harmonische. Het moment voor scheurinitiatie is on-line bepaald en correspondeert met een drempelwaarde gelijk aan 54 µm. Er is bewezen dat deze thermografische methode een betere nauwkeurigheid biedt dan een eerder toegepaste methode op basis van een analyse van de zuigerverplaatsing van de proefmachine.

De ontwikkelde methodologieën op basis van infrarood thermografie blijken veelbelovend om schade en scheurinitiatie in fretting vermoeiing te bestuderen. Voor de bepaling van de vermoeiingslimiet kan men veel tijd en proefstukken besparen in vergelijking met conventionele methodes. De nauwkeurigheid kan nog verder worden verbeterd door het verschil in spanningsniveau tussen de verschillende blokbelastingen te verkleinen. Een

stap verder dan de huidige praktijk voor infrarood thermografie is de mogelijkheid voor online data-acquisitie en verwerking voor detectie van scheurinitiatie. De gevonden drempelwaardes voor minimale scheurlengte liggen binnen het bereik gerapporteerd voor een off-line techniek op basis van SEM onderzoek, maar zijn hoger dan deze op basis van potentiaalval. De voorbereiding van de experimenten is echter heel eenvoudig in vergelijking met de potentiaalval-methode die eerder complexe kalibratie vereist. De drempelwaarde kan nog verbeterd worden door gebruik te maken van een betere lens en door de vermoeiingsproeven uit te voeren met een spanningsverhouding gelijk aan -1. Daarnaast kan het toepassingsgebied van de thermografische methodologieën gemakkelijk uitgebreid worden tot fretting vermoeiing van verschillende materialen en contacttypes en zelfs tot vermoeiingsproeven op gebogen proefstukken. De experimentele resultaten die in het kader van dit proefschrift werden ontwikkeld, kunnen gebruikt worden om de kennis van de mechanica van fretting vermoeiing te verdiepen, met name wat betreft de fase van scheurinitiatie en het schaaleffect.

Contents

Symbols and acronyms

Symbols

a	Contact semi-width	mm
A	Cross-section of the specimen	mm^2
b	Crack length	µm
b_0	Border between micro- and macro-crack	µm
c	Sticking zone	mm
C	Paris law constant	$MPa^{-4}m^{-1}$
d	Cross-head displacement	mm
e	Eccentricity of the mixed stick-slip zones	mm
E	Young's modulus	GPa
E*	Relative Young's modulus	GPa
f	Loading frequency	Hz
F_σ	Fatigue axial load	kN
$F(R_3)$	Axial force above the contact zones	kN
$F(R_4)$	Calibrated axial force of a strain gauge attached on the surface below the contact zones	kN
I_1	First stress invariant	MPa
J_2	Second invariant of a deviatoric stress tensor	$(MPa)^2$
K	Stress intensity factor	$MPa.m^{1/2}$
K_0	Stress intensity factor threshold for macro-crack growth	$MPa.m^{1/2}$
K_{th}	Stress intensity factor threshold for micro-crack growth	$MPa.m^{1/2}$
m	Fatigue strength exponent	-
n	Fatigue ductility exponent	-
N_f	Total lifetime	cycles
N_i	Crack initiation time	cycles
N_p	Crack propagation time	cycles

P	Normal force	kN
p(x)	Normal distribution	MPa
p_0	Maximum contact pressure	MPa
Q	Tangential force	kN
q(x)	Shear distribution	MPa
R-ratio	Fatigue ratio	-
R	Radius of cylindrical body	mm
R_{pad}	Radius of cylindrical pad	mm
T_0	Initial temperature	K
T_1	First harmonic or Thermoelastic temperature amplitude	K
T_2	Second harmonic temperature amplitude	K
T_3	Third harmonic temperature amplitude	K
T_{exp}	Overall experimental temperature	K
T_a	Overall temperature amplitude	K
ΔT	Mean temperature rise of the specimen	K
$V(R_4)$	Measured voltage from a strain gauge attached on the specimen surface below the contact zones	V
V_{spring}	Measured voltage from a strain gauge attached on one of the compliant springs	V
x	Distance along the contact width	mm

α	Coefficient of thermal expansion	K^{-1}
β_0	Regression coefficient	K
β_1	Regression coefficient	K/cycles
γ	Shear strain	-
δ	Relative slip amplitude	mm
ε	Normal strain	-
ε_e	Elastic strain	-
ε_p	Plastic strain	
ε_t	Plastic strain	-
$\varepsilon_{f'}$	Fatigue ductility coefficient	-

θ	Rotational misalignment of cylindrical pads	^{o}
μ	Friction coefficient	-
ρ	Mass density	kg/m^3
σ	Normal stress	MPa
$\sigma_{b,fl}$	Bending fatigue limit	MPa
$\sigma_{f'}$	Fatigue strength coefficient	MPa
σ_{fl}	Fatigue limit	MPa
σ_{ult}	Ultimate strength	MPa
σ_y	Yield strength	MPa
τ	shear stress	MPa
τ_{fl}	Shear fatigue limit	MPa
τ_s	Surface shear stress within the contact zone	MPa
υ	Poisson ratio	-
φ	Phase shift of temperature response to loading force	rad

Acronyms

A.C.	Alternative current
CCD	Charge coupled device
D.C.	Direct current
eFFDP	Enhanced fretting fatigue damage parameter
4BP	Four bucket point
FFT	Fast Fourier transform
FS	Fatemi-Socie
HgCDTe	mercury-cadmium-telluride
HSS	High-strength steel
InSb	indium-antimonide
IR	Infrared
LSM	Least square method
SEM	Scanning electron microscope
SLIM	Standard lock-in method

SWT	Smith-Watson-Topper
UV	Ultraviolet
VM	Variance method

Chapter 1 Introduction

"General characteristics of fretting fatigue are presented. The motivation of the research is described, followed by the objectives of this dissertation."

1 Introduction

1.1 Context

Dynamic forces in mechanical systems cause vibrations and as a result a very small reciprocating movement (microslip, typically *5* to *50* microns) between the interacting surfaces. Consequently fretting will arise due to local material removal and cracks could initiate at the border of the stick-slip area. These cracks could further propagate due to fatigue and the lifetime of the component will be degraded. Example installations and machine components that are cyclically loaded and can be prone to this type of damage are heat exchangers [Attia, 2006] and most mechanical joints such as bolted connections [Jayaprakash, Mutoh & Yoshii, 2011; Wagle & Kato, 2009], rivets [Li et al., 2008; Szolwinski et al., 2000], dovetail connections [Jayaprakash & Mutoh, 2014; Ruiz, Boddington & Chen, 1984; Tang et al., 2009], press fits [Gutkin & Alfredsson, 2008; Hirakawa, Toyama & Kubota, 1998], etc. A well-known in-service failure due to fretting fatigue happened in 2011 on a Boeing 737-3H4 (N632SW) during flight 812 of Southwest Airlines. The flight crew had to make an emergency landing as the flight experienced an immediate decompression while taking off through flight level 340. Post-accident inspection revealed that a section of fuselage skin about *1 524 mm* long by *203.2 mm* wide had fractured and flapped open on the upper left side above the wing. The National Transportation Safety Board determined that the probable cause of this accident was the improper installation of the fuselage crown skin panel at the S-4L lap joint during the manufacturing process, which resulted in multiple site damage fatigue cracking and eventual failure of the lower skin panel. The origin of the fracture was fretting fatigue damage on riveted joints of the aeroplane fuselage structure as illustrated in Figure 1.1 [NTSB, 2013].

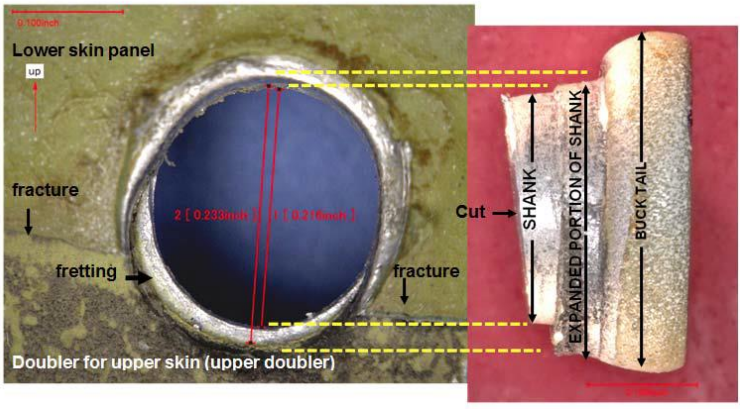

Figure 1.1 Fretting damage of a rivet in an aircraft accident [NTSB, 2013]

1.2 General characteristics of fretting fatigue

1.2.1 Contact types

Above mentioned applications which can be at risk of fretting fatigue damage can be characterized by different contact types based on their individual design. For instance, prestressed bolts and dovetail connections are under complete contact while riveting, press fitting and heat exchangers are subjected to fretting under incomplete and conformal contact. These typical contact configurations are illustrated in Figure 1.2 [Hills & Nowell, 1994]. In case of an incomplete contact, the contact area also depends on the normal load. The contact between the two bodies starts as single point or line contact when unloaded but will spread to an area contact when a normal load is applied. Conformal and non-conformal contacts can be distinguished by how easily the two surfaces conform to each other when they are pressed together. A non-conformal contact normally leads to a much higher contact pressure. In other words, the contact area under non-conformal contact is much smaller than the radii of curvature of both bodies.

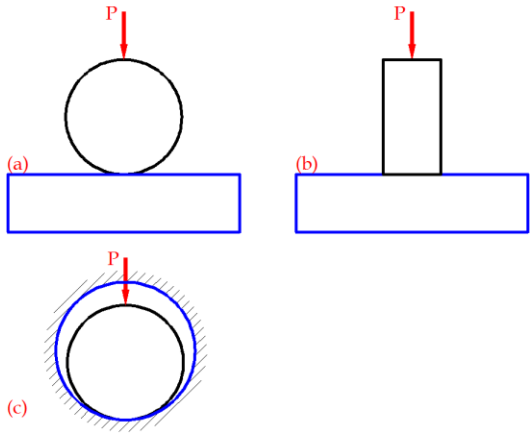

Figure 1.2 Basic contact types. (a) Incomplete and non-conformal, (b) complete, (c) incomplete and conformal [Hills & Nowell, 1994]

1.2.2 Crack initiation and propagation

Like plain fatigue, lifetime of materials or components subjected to fretting fatigue can be divided into two main proportions: crack initiation and crack propagation as shown in Figure 1.3. In plain fatigue, crack initiation is the consequence of cyclic slip activity or process a long a persistent slip band on a specific grain of a specimen due to dislocation (see Figure 1.4) [Schijve J, 2009]. Crack nucleation is more likely to occur at a free surface of the material than in the subsurface because there is less constraint to the cyclic slip. If slip occurs in a grain, a slip step will be created at the material surface during the loading stage of a load cycle, Figure 1.4a. The new surface may be corroded,

as it is exposed to an external environment (eg. air or liquid). Slip also implies that some strain hardening is induced on that specific grain since it is a result of micro-plastic deformation due to shear stress. As such, reverse slip cannot take place on the same slip line but on an adjacent one during the unloading stage of a load cycle, Figure 1.4b. This sequence is continued in the next cycles of the cyclic load until a crack nucleates. The exact moment of crack nucleation is extremely difficult to be detected in experiments. Therefore, researchers define another term, crack initiation, which is the moment when a certain crack size becomes detectable by a non-destructive technique (NDT), Figure 1.3.

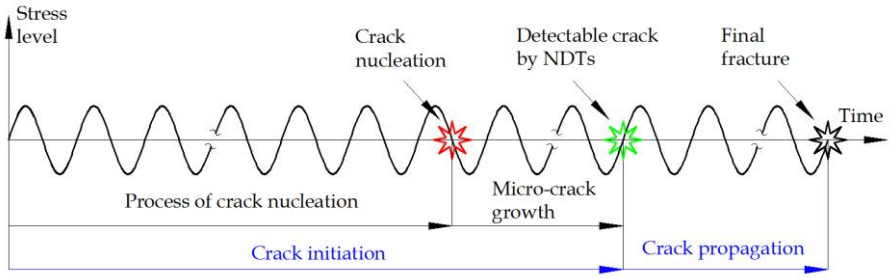

Figure 1.3 Normal process of fatigue failure

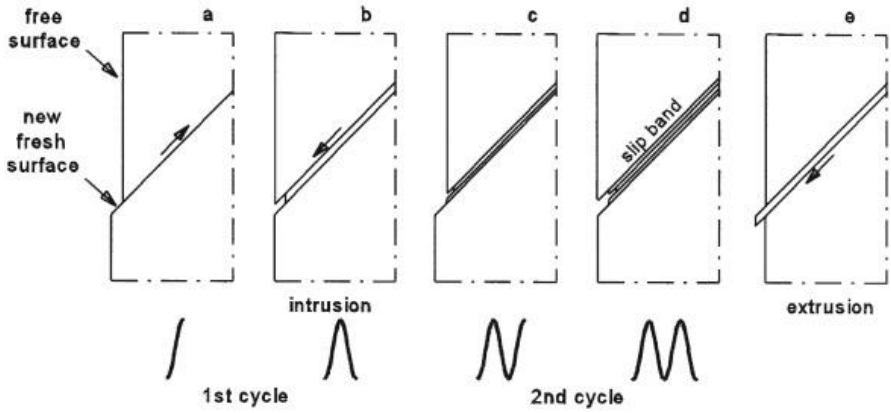

Figure 1.4 Crack nucleation process in plain fatigue [Schijve J, 2009]

Even though the cyclic slip activity takes place at a free surface of a specimen, the exact location within the specimen can hardly be predicted because the shear stress level on each grain is not homogenous, and it is difficult to identify which grain is subjected to micro-plastic deformation. Only a specially designed specimen that forces the stress raiser to be present in a specific zone would allow to predict the crack location and to monitor the cyclic slip process via optical techniques. Unlike plain fatigue, the location of crack initiation is commonly very well known in fretting fatigue. In fretting

fatigue tests on a standard dog-bone specimen clamped by two cylindrical pads, the localized stress concentration induced by the contact loadings (P and Q, see Figure 1.5) imposes the crack to be initiated within the contact area. Specifically, it originates at the trailing edge of the contact area which is the border of the stick-slip zone (see further Figure 1.5). However, whether the mechanism of crack initiation under fretting fatigue is identical to that of plain fatigue remains extremely challenging to prove. As the crack is hidden in a closed contact, the optical techniques used in plain fatigue are not able to visualize the damage initiation process.

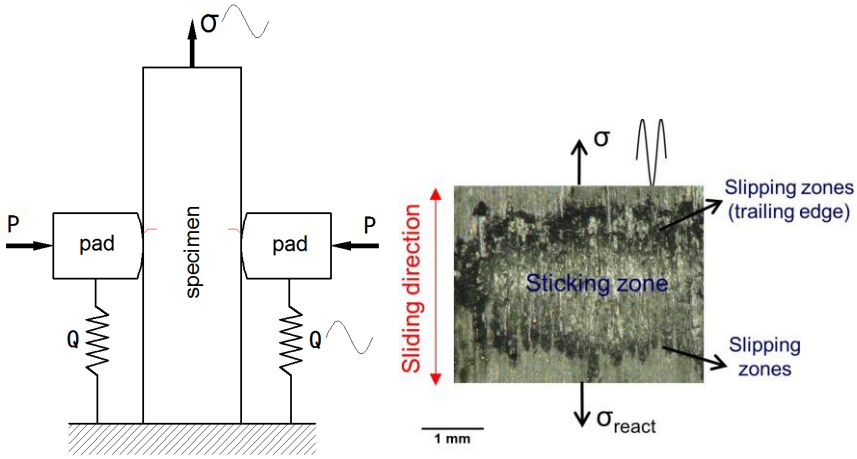

Figure 1.5 Typical fretting scar due to partial slip regime under cylinder-plane contact

1.2.3 Size effect in fretting fatigue

Like plain fatigue, several analytical models have been developed for a better understanding of the mechanics of fretting fatigue and typically been validated by coupon-scale laboratory tests. These models span a wide range from contact mechanics to damage and fracture mechanics. Hertzian contact types are preferably selected for an experimental study even though sample preparation and experimental set-up for such contact types are more complex than for the complete contact type. This is because well documented contact solutions (developed by Hertz) are available for such configuration. The most common contact configuration is cylinder on plane. In fretting fatigue, there are more challenges over plain fatigue such as complexity of stress states nearby the contact area, stress gradients and complex surface damage evolution due to fretting wear and corrosion. Additionally, there is a pronounced size effect in fretting fatigue. Below a critical contact area, lifetime is shifted sharply from a few hundred cycles to 10^7 cycles despite that the magnitudes of stress levels are identical [Hills, Nowell & O'Connor, 1988]. This change cannot solely be attributed to the typical scatter in fatigue since the level of difference is just too much. Because of this size effect, there

is a speculation whether or not stress-based approaches alone can be sufficient to study fretting fatigue problems [Mugadu, Hills & Nowell, 2002].

1.2.4 Fretting damages

Fretting fatigue lifetime has sometimes been investigated as a function of slip amplitude, not a typical stress or strain magnitude. A study conducted by [Vingsbo & Söderberg, 1988] (see Figure 1.6) revealed different sliding regimes: stick, mixed stick-slip (or partial slip), gross slip, and reciprocating sliding. Each sliding regime is characterized by a different damage mechanism. Fretting is normally covered by mixed stick-slip and gross slip. Reciprocating sliding can be distinguished from gross slip by evacuation of worn materials or debris from the contact zones. Under mixed stick-slip, cracking is dominant compared to wear due to a very localized stress concentration while under gross slip embryos of cracks may be removed by wear due to a higher slip amplitude. These observations were confirmed by the study of [Fouvry, Kapsa & Vincent, 1996]. As can be seen in the Figure 1.6, fatigue lifetime is decreasing with an increase of the slip amplitude under partial slip until a transition to gross slip where the lifetime is increasing with the slip amplitude. Wear was always observed to be increasing with the slip amplitude under both regimes but it is significantly increased under gross slip. Therefore, a partial slip regime is normally simulated to study fretting fatigue while gross slip is selected to investigate fretting wear.

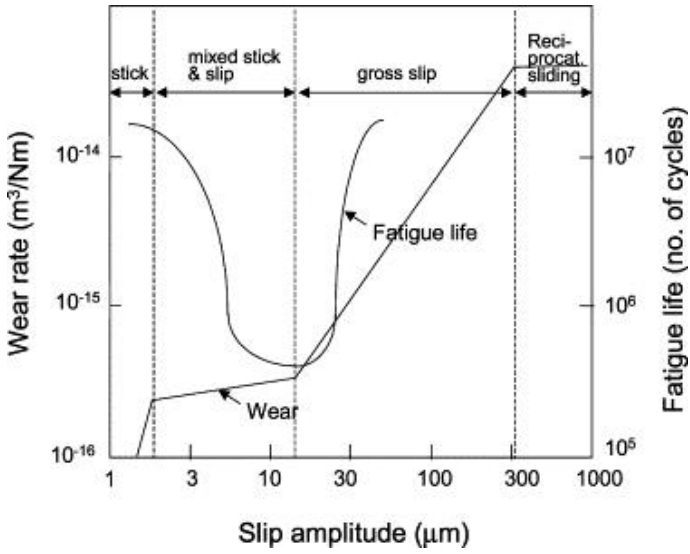

Figure 1.6 Fatigue lifetime versus slip amplitude [Vingsbo & Söderberg, 1988]

1.3 Motivation

Understanding crack propagation is less difficult than the crack initiation part [Hills et al., 2016; Hills & Nowell, 2014]. Once the stress intensity factor at a crack tip is developed, crack growth rate can be well estimated based on a Paris law obtained from plain fatigue tests. The main challenges for the crack initiation are a lack of knowledge on the crack formation process and a lack of advanced inspection techniques that allow to monitor crack initiation.

Without the experimental evidence of the crack initiation process, researchers needed to develop several hypotheses to study fretting fatigue crack initiation. Some compared fretting fatigue problems to fatigue of notched specimens because of the similarity of stress concentration [Ciavarella, 2003; Giannakopoulos et al., 2000]. Others treated fretting fatigue as multiaxial fatigue problems [Araújo & Nowell, 2002; Fouvry, Kapsa & Vincent, 2000; Szolwinski & Farris, 1996] because the stress state under fretting fatigue is multiaxial and features of failure due to fretting fatigue were claimed to be similar to those observed in multiaxial fatigue tests [Szolwinski & Farris, 1996]. Crack initiation was observed to be along a plane of maximum shear stress and first growth occurred under mixed mode I & II. Finally the crack path turned perpendicular to the fatigue loading and grew under pure mode I until final rupture. The multiaxial fatigue approach seems to be the most common so far, but the models used to predict the number of cycles to fretting fatigue crack initiation could only be validated based on the difference between total lifetime counted from the testing machine and crack propagation time determined by post-mortem analysis [Lykins, Mall & Jain, 2001] or analytical solutions [Araújo & Nowell, 2002; Szolwinski & Farris, 1998]. A slip band theory adopted from plain fatigue was also utilized [Fellows, Nowell & Hills, 1997].

In a more direct way, [Fellows, Nowell & Hills, 1997] aimed to separate the crack initiation and propagation stages by trying to find specific combinations of the fretting fatigue loads (σ, P, Q) which only affect crack initiation but not crack propagation, and vice-versa. Each combination is a variation of magnitude, frequency, phase difference and wave form. This approach led to developing a bi-actuator fretting fatigue test rig that allows independent control of tangential force, Q, and fatigue stress, σ, in terms of phase difference, frequency and wave form. However, the research was unsuccessful since no combinations of the fretting fatigue loads only affecting crack initiation were found.

To the author's best knowledge, there is only very limited literature on the separation of crack initiation and propagation times. Changes in electrical resistance and voltage due to crack initiation were used by [Endo & Goto, 1976] and [Meriaux et al., 2010], respectively. [De Pannemaecker et al., 2017] achieved the detection of fretting fatigue crack initiation with an X-ray synchrotron technique. These experimental techniques have their own merits

but one common drawback is that they only allow to provide information after the detection of crack initiation towards the final rupture of the specimen. As explained earlier the more complex stage is the mechanism before the crack initiation, i.e. crack nucleation process or damage accumulation, which demands another technique like the infrared thermography [Berthel et al., 2014; Szolwinski et al., 1999].

Being able to separate the crack initiation and propagation stages is critical from an application point of view since different remedies are used to improve each portion of total lifetime. Introduction of surface residual compressive stresses from for example shot peening or laser peening could improve the crack initiation but not the propagation lifetime while static yield strength and grain size could have more influence on the crack propagation lifetime [Schijve J, 2009]. Also, components like turbine discs need to be operated with a very high integrity, i.e. these need to be replaced immediately when a crack is detected [Fellows, Nowell & Hills, 1997]. From a theoretical point of view, it is also necessary to realize which crack length separates initiation and propagation since different theories are used to predict the corresponding lifetime. Continuum mechanics are used to study crack initiation and fracture mechanics are used to predict crack propagation. Values of fretting fatigue initiation and propagation lifetime were found to be very inconsistent in laboratory experiments. [Endo & Goto, 1976] experimentally concluded that fretting fatigue crack propagation lifetime takes most of the total lifetime in fully reversed bending tests. However, [Hills, Nowell & O'Connor, 1988], based on experimental results and analytical solutions, found that it is the crack initiation stage that controls most of the lifetime in fretting fatigue.

2 Objectives and organization of the manuscript

2.1 Objectives of the thesis

The main objective of this dissertation is to develop robust experimental methodologies based on infrared thermography to investigate fretting fatigue damage. The first goal is to determine the fretting fatigue limit and the second goal is the on-line detection of fretting fatigue crack initiation. The methodologies will be evaluated for two different metals (an aluminium alloy and a structural steel) and for two different Hertzian contact types (cylinder-plane and perpendicular cylindrical contacts). Realizing these goals should allow to discriminate between the crack initiation and propagation times in laboratory tests. A collection of data on crack initiation lifetime of both materials and contact types will be developed, with the purpose to provide a better validation of relevant analytical and numerical models. The developed experimental methodologies should also be sufficiently generic to be applicable to other metals subjected to other types of cyclic loads for which the location of crack initiation can be estimated prior to the tests.

2.2 Organisation of the manuscript

Chapter 2 gives a summary of the current state-of-the art with respect to the mechanics of fretting fatigue, a brief review of Hertzian contact distribution solutions under partial slip regime, and the potential of infrared thermography for damage detection under cyclic loading.

In Chapter 3, a review is made of existing fretting fatigue test rigs focusing on instrumentation and damage characterisation before introducing the UGent fretting fatigue test rig. Also, the infrared thermographic camera installed with the UGent test rig, along with a few signal processing methods to evaluate fretting fatigue damage is described in Chapter 4.

In Chapter 5, an experimental methodology based on infrared thermography for detection of fretting fatigue damage and rapid determination of a fretting fatigue limit is elaborated.

Chapter 6 is dedicated to the development of an experimental methodology based on lock-in thermography for the on-line detection of fretting fatigue crack initiation. The methodology is also used to discriminate the crack initiation and propagation stages of fretting fatigue tests with cylinder-plane contact configuration.

In Chapter 7, the developed experimental methodologies are applied to low cycle fatigue tests of a bent sample made of a high strength steel. This part of the work will confirm the more generic potential of the methodologies.

In the last Chapter, the main conclusions of this dissertation are formulated together with possible future research activities for a better understanding of the mechanics of fretting fatigue crack initiation.

References

Araújo, J.A., Nowell, D. (2002) The Effect of Rapidly Varying Contact Stress Fields on Fretting Fatigue. *International Journal of Fatigue*, 24, 763–75.

Attia, M.H. (2006) Fretting Fatigue and Wear Damage of Structural Components in Nuclear Power Stations — Fitness for Service and Life Management Perspective. *Tribology International*, 39, 1294–304.

Berthel, B., Moustafa, A.-R., Charkaluk, E., Fouvry, S. (2014) Crack Nucleation Threshold under Fretting Loading by a Thermal Method. *Tribology International*, 76, 35–44.

Ciavarella, M. (2003) A ' Crack-like ' Notch Analogue for a Safe-Life Fretting Fatigue Design Methodology. *Fatigue & Fracture of Engineering Materials & Structures*, 26, 1159–70.

De Pannemaecker, A., Buffiere, J.Y., Fouvry, S., Graton, O. (2017) In Situ Fretting Fatigue Crack Propagation Analysis Using Synchrotron X-Ray Radiography. *International Journal of Fatigue*, 97, 56–69.

Endo, K., Goto, H. (1976) Initiation and Propagation of Fretting Fatigue Cracks. *Wear*, 38, 311–24.

Fellows, L.J., Nowell, D., Hills, D.A. (1997) On the Initiation of Fretting Fatigue Cracks. *Wear*, 205, 120–9.

Fouvry, S., Kapsa, P., Vincent, L. (1996) Quantification of Fretting Damage. *Wear*, 200, 186–205.

Fouvry, S., Kapsa, P., Vincent, L. (2000) A Multiaxial Analysis of Fretting Contact Taking into Account the Size Effect. In *Fretting Fatigue: Current Technology and Practices, ASTM STP 1367, D. W. Hoeppner, V. Chandraskaran, and C. B. Elliot*. ASTM, West Conshohocken, PA.

Giannakopoulos, A.E., Lindley, T.C., Suresh, S., Chenut, C. (2000) Similarities of Stress Concentrations in Contact at Round Punches and Fatigue at Notches : Implications to Fretting Fatigue Crack Initiation. *Fatigue & Fracture of Engineering Materials & Structures*, 23, 561–71.

Gutkin, R., Alfredsson, B. (2008) Growth of Fretting Fatigue Cracks in a Shrink-Fitted Joint Subjected to Rotating Bending. *Engineering Failure Analysis*, 15, 582–96.

Hills, D.A., Nowell, D. (1994) *Mechanics of Fretting Fatigue*. Kluiwer Academic Publishers, Dordrecht.

Hills, D.A., Nowell, D. (2014) Mechanics of Fretting fatigue—Oxford's Contribution. *Tribology International*, 76, 1–5.

Hills, D.A., Nowell, D., O'Connor, J.J. (1988) On the Mechanics of Fretting Fatigue. *Wear*, 125, 129–46.

Hills, D.A., Ramesh, R., Fleury, R.M.N., Parel, K. (2016) A Unified Approach for Representing Fretting and Damage at the Edges of Incomplete and Receding Contacts. *Tribology International*, 108, 16–22.

Hirakawa, K., Toyama, K., Kubota, M. (1998) The Analysis and Prevention of Failure in Railway Axles. *International Journal of Fatigue*, 20, 135–44.

Jayaprakash, M., Mutoh, Y. (2014) Fretting Fatigue Strength Prediction of Dovetail Joint and Bolted Joint by Using the Generalized Tangential Stress Range–compressive Stress Range Diagram. *Tribology International*, 76, 116–21.

Jayaprakash, M., Mutoh, Y., Yoshii, K. (2011) Fretting Fatigue Behavior and Life Prediction of Automotive Steel Bolted Joint. *Materials & Design*, 32, 3911–9.

Li, Y.J., Tao, C.H., Zhang, W.F., Jiang, T. (2008) Fracture Analysis on Cage Rivets of a Cylindrical Roller Bearing. *Engineering Failure Analysis*, 15, 796–801.

Lykins, C.D., Mall, S., Jain, V.K. (2001) Combined Experimental – Numerical Investigation of Fretting Fatigue Crack Initiation. *International Journal of Fatigue*, 23, 703–11.

Meriaux, J., Fouvry, S., Kubiak, K.J., Deyber, S. (2010) Characterization of Crack Nucleation in TA6V under Fretting–fatigue Loading Using the Potential Drop Technique. *International Journal of Fatigue*, 32, 1658–68.

Mugadu, A., Hills, D.A., Nowell, D. (2002) Modifications to a Fretting-Fatigue Testing Apparatus Based upon an Analysis of Contact Stresses at Complete and Nearly Complete Contacts. *Wear*, 252, 475–83.

NTSB (2013) Aircraft Accident Report. Technical Report NTSB/AAR-89/03.

Ruiz, C., Boddington, P.H.B., Chen, K.C. (1984) An Investigation of Fatigue and Fretting in a Dovetail Joint. *Experimental Mechanics*, 24, 208–17.

Schijve J (2009) *Fatigue of Structures and Materials*. Springer Science+ Business Media, B. V.

Szolwinski, M.P., Farris, T.N. (1996) Mechanics of Fretting Fatigue Crack Formation. *Wear*, 98, 93–107.

Szolwinski, M.P., Farris, T.N. (1998) Observation, Analysis and Prediction of Fretting Fatigue in 2024-T351 Aluminum Alloy. *Wear*, 221, 24–36.

Szolwinski, M.P., Harish, G., Farris, T.N., Sakagami, T. (1999) In-Situ Measurement of Near-Surface Fretting Contact Temperatures in an Aluminum Alloy. *Journal of Tribology-Transactions of the ASME*, 121, 11–9.

Szolwinski, M.P., Harish, G., McVeigh, P.A., Farris, T.N. (2000) Experimental Study of Fretting Crack Nucleation in Aerospace Alloys with Emphasis

on Life Prediction. In Hoeppner, D.W., Chandraskaran, V. and and Elliot, C.B. (eds.), *Fretting Fatigue: Current Technology and Practices, ASTM STP 1367*. ASTM, West Conshohocken, PA, pp. 267–81.

Tang, H., Cao, D., Yao, H., Xie, M., Duan, R. (2009) Fretting Fatigue Failure of an Aero Engine Turbine Blade. *Engineering Failure Analysis*, 16, 2004–8.

Vingsbo, O., Söderberg, S. (1988) On Fretting Maps. *Wear*, 126, 131–47.

Wagle, S., Kato, H. (2009) Ultrasonic Detection of Fretting Fatigue Damage at Bolt Joints of Aluminum Alloy Plates. *International Journal of Fatigue*, 31, 1378–85.

Chapter 2 Literature review

"The state-of-the-art of the mechanics of fretting fatigue is reviewed and the potential of infrared thermography for fretting fatigue damage investigation is introduced"

1 Review of a Hertzian contact under partial slip

In this section, a Hertzian contact under partial slip is briefly introduced. Normally, contact problems deal with the determination of contact force distribution, contact shapes and dimensions, and subsurface stresses & strains. This section will not discuss the subsurface stress and strain field determination; only knowledge of contact force distribution, contact shape and dimension is required to define fretting fatigue test conditions. The chosen conditions need to achieve a partial slip regime to simulate cracking damage and to ensure zero or negligible macro-plasticity in order to simulate high cycle fatigue regime.

1.1 Line contact under partial slip [Hills & Nowell, 1994]

A contact configuration of cylindrical pads on a flat specimen is incomplete and non-conformal according to the definition in the previous chapter. The two bodies initially touch along a line when no load is applied. The contact line will spread into a rectangular contact due to deformation when a normal load, P, is applied. If the contact area is much smaller than the dimensions of the two bodies, the analysis of contact stresses at the planar body can be done assuming an infinite half-plane. The boundary condition for the vertical displacement leads to an elliptical contact pressure distribution as shown in equation (2-1). Equilibrium of forces in the vertical direction allows to calculate the maximum contact pressure, p_0 and the contact half-width, a, as in equations (2-2) and (2-3), respectively. There, $p(x)$ is the normal pressure distribution, x is a variable distance along the contact area. R is the cylindrical radius, and E^* $(1/E^*=[(1-\upsilon_1^2)/E_1+(1-\upsilon_2^2)/E_2]$ is the relative Young's modulus.

$$p(x) = -p_0\sqrt{1-(x/a)^2} \qquad \textbf{(2-1)}$$

$$a = \sqrt{\frac{4PR}{\pi E^*}} \qquad \textbf{(2-2)}$$

$$p_0 = \frac{2P}{\pi a} = \sqrt{\frac{PE^*}{\pi R}} \qquad \textbf{(2-3)}$$

Now consider that an additional tangential force, Q, with a magnitude lower than the frictional force, μP, is applied (μ is friction coefficient). For rigid bodies, this loading condition would lead to complete adhesion of the two bodies. For elastic bodies, it is almost impossible to obtain complete sticking, particularly at the contact edges due to force concentrations. Normally, a mixed stick-slip or partial slip regime will occur. The region where the generated shear stress distribution is equal to the frictional stress distribution, $q(x)=\mu p(x)$, is slipping whereas sticking occurs if $q(x)<\mu p(x)$.

Figure 2.1 illustrates a mixed stick-slip zone of a cylinder-plane contact. The sticking semi-width, *c*, and the shear stress distribution in the stick area can be computed from equations (2-4) and (2-5), respectively.

$$c/a = \sqrt{1-\left|Q/\mu P\right|} \qquad \textbf{(2-4)}$$

$$q'(x) = -\mu p_0 (c/a)\sqrt{1-(x/c)^2} \text{ for } -c < x < +c \qquad \textbf{(2-5)}$$

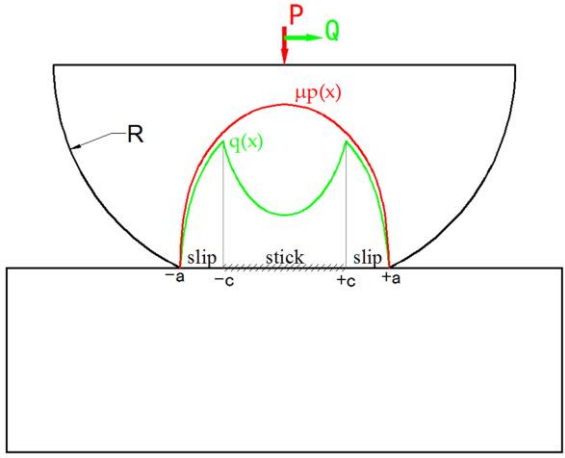

Figure 2.1 Mixed stick-slip zone for a line contact

When in addition to the shear stress, a fatigue stress, σ, is also applied (see Figure 2.2), it will cause an eccentricity, *e*, of the mixed stick-slip zones. This eccentricity can be determined from equation (2-6).

$$e = b = \frac{\sigma a}{4\mu p_0} \qquad \textbf{(2-6)}$$

The peak and shape of the shear stress distribution are also disturbed by this eccentricity as illustrated in Figure 2.2, and the shear stress distribution is altered as in equation (2-7). A larger slip zone and larger peak shear traction are observed at the side where the fatigue stress is applied, termed as the trailing edge of the contact area. It is at this trailing edge where a fretting fatigue crack is likely to nucleate and it may grow further until final fracture of the component. When defining experimental conditions, the magnitude of the fatigue stress is normally limited to a certain level to prevent reverse slip at the other contact edge. This threshold can be estimated by equation (2-8).

$$q''(x) = -\mu p_0 (c/a)\sqrt{1-((x-e)/c)^2} \text{ for } -c+e < x < +c+e \qquad \textbf{(2-7)}$$

$$\frac{\sigma}{\mu p_0} \le 4\left(1-\sqrt{1-Q/\mu P}\right) \qquad \textbf{(2-8)}$$

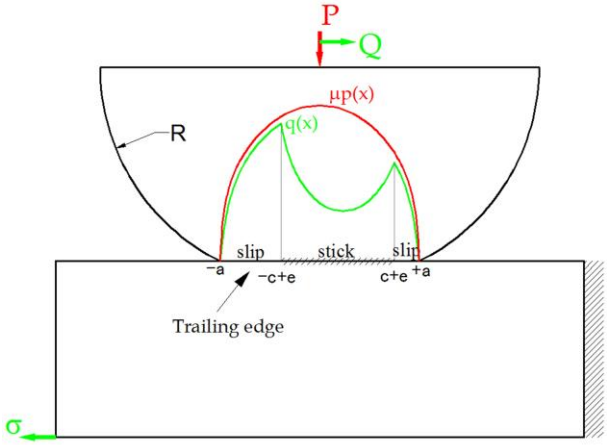

Figure 2.2 Shift of mixed stick-slip zone by fatigue load

2 State of the art of mechanics of fretting fatigue

The study of fretting fatigue is a combination of tribology and fatigue. From a tribological perspective, fretting fatigue problems in partial slip regime are extremely difficult. Contact solutions under partial slip have been improved for a variety of contact types. But, wear investigation is extremely challenging since it is hidden in the contact. Friction cannot be measured because the macroscopic relative displacement is almost inexistent, and only on a microscopic level slipping occurs. Only the friction coefficient at the border between the gross slip and partial slip region is used as a representation for partial slip. To some extent, an analytical approach allows to predict the friction coefficient under partial slip. Therefore, fretting fatigue problems are mostly studied from a fatigue perspective. Fatigue investigation itself requires two different methods to be applied. Crack initiation is based on continuum mechanics while crack propagation is based on fracture mechanics. However, the size effect in fretting fatigue conditions has until present led to lots of debates on the analogy of fatigue and fretting fatigue.

The size effect under fretting fatigue conditions was studied by Bramhall in the early 1970s [Hills, Nowell & O'Connor, 1988]. Below a critical contact area, lifetime shifts sharply from a few hundred cycles to 10^7 cycles despite that the magnitude of stress levels is similar. This effect has been observed for several alloys, such as aluminium alloy, titanium alloy and high strength steel [Mugadu, Hills & Nowell, 2002]. The size effect observed for aluminium alloy Al-4Cu is illustrated in Figure 2.3 [Nowell, Dini & Hills, 2006]. Bramhall

could achieve such investigation by manipulating the contact radius, R, of the cylindrical pad and the applied normal load, P, in a way that the maximum contact pressure is maintained while varying the semi-width of the contact area. Maximum contact pressure p_0 is proportional to $(P/R)^{1/2}$ (see equation (2-3)) and the contact semi-width a is proportional to $(PR)^{1/2}$ (see equation (2-2)). So far, many researchers have attempted to explain this size effect in either of two ways. Firstly based on crack propagation criteria, i.e. the crack is initiated but arrested below the critical contact area. Secondly based on crack initiation criteria, i.e. the crack could not be initiated below the critical contact area.

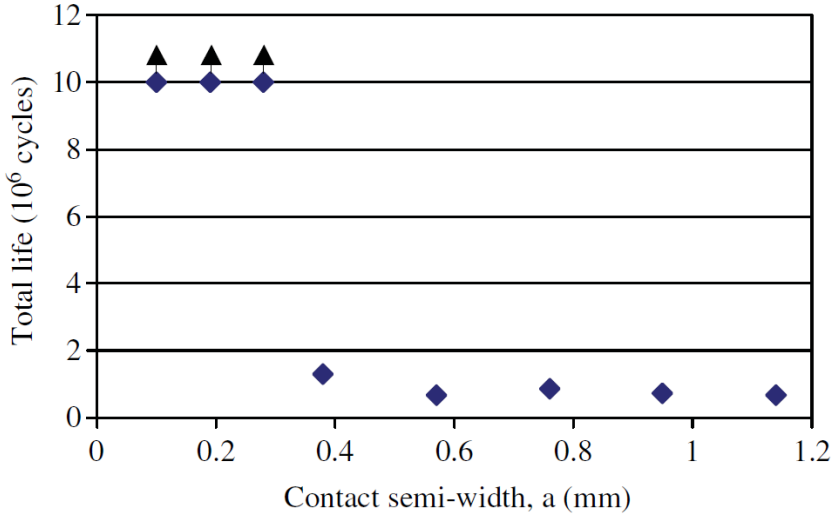

Figure 2.3 Lifetime vs contact semi-width of Al-4Cu alloy [Nowell, Dini & Hills, 2006]

2.1 Crack propagation based criteria

The term crack propagation here basically covers also the micro-crack growth, while in some literature it is solely defined as macro-crack growth. The border between short and large cracks, b_0, may be determined by equation (2-9), where σ_{fl} is the fatigue limit, and ΔK_0 is the stress intensity factor threshold for a macro-crack to grow. This threshold is defined to correspond to a macro-crack growth rate (db/dN) of zero; or based on standard [ASTM-E647-08, 2009] this threshold is obtained when $db/dN=10^{-10}$m/cycle. However, this threshold is not applicable to micro-crack growth, since a micro-crack could still propagate even though its crack tip stress intensity factor is below ΔK_0. This phenomenon has been observed by [Miller, 1993], and it was interpreted that the micro-crack related threshold is different from the macro-crack related threshold. Very prominent micro-crack stress intensity factor threshold definitions for plain fatigue have been

developed by Kitagawa-Takahashi, equation (2-10) [Kitagawa & Takahashi, 1976] and El-Haddad, equation (2-11) [El Haddad, Smith & Topper, 1979].

$$\Delta K_{0\cdot} = 1.12\sigma_{fl}\sqrt{\pi b_0} \quad \textbf{(2-9)}$$

The crack propagation criteria for fretting fatigue are based on short-crack arrest methodologies. It is expected that below a critical contact area, the stress gradient at the contact surface is so sharp that micro-crack growth is arrested when it grows just a little further from the initiation zone (the contact surface). The further a micro-crack tip is located from the contact zone, the less influence of contact load. [Araújo & Nowell, 1999] calculated the stress intensity factor at a micro-crack tip assuming that the micro-crack growth is perpendicular to the fatigue loading and controlled solely by mode I. Based on the Kitagawa-Takahashi or El Haddad micro-crack stress intensity factor threshold, crack arrest conditions could be predicted. This methodology was used to interpret the size effect of fretting fatigue. However, [Araújo & Nowell, 1999] could not find evidence of crack arrest during their experiments that could confirm their hypothesis.

$$\Delta K_{th,Takahashi} = \Delta K_{0\cdot}\sqrt{\frac{b}{b_0}} \quad if\ b < b_0 \quad \textbf{(2-10)}$$

$$\Delta K_{th,El-Haddad} = \Delta K_{0\cdot}\sqrt{\frac{b}{b+b_0}} \quad if\ b < b_0 \quad \textbf{(2-11)}$$

[Fouvry et al., 2008] extended the crack arrest methodology to determine a stress intensity factor under mixed mode (mode I&II) growth of an oblique micro-crack (Figure 2.4). Figure 2.5 illustrates the threshold diagrams for micro- and macro-cracks based on both Kitagawa-Takahashi (K-T) and El Haddad approaches. Crack arrest occurs when the crack tip stress intensity factor falls below the micro-crack growth threshold, the squared dotted line "□" in Figure 2.5. Without the crack arrest, the crack will grow until the complete failure of the specimen, the triangle dotted line "▲" in Figure 2.5. Based on these diagrams as used by [Araújo & Nowell, 1999] and experimental evidence of crack arrest at a certain depth, the size effect could be interpreted. This methodology was also considered as a design for infinite lifetime since it allows to determine the corresponding fretting fatigue limit conditions [Nowell, Dini & Hills, 2006]. In addition, crack growth could be well predicted based on the Paris law parameters determined from plain fatigue tests once the stress intensity factor is fully developed. This portion of fretting fatigue lifetime is more or less resolved with the help of well-established fracture mechanics based calculations [Hills & Nowell, 2014]. However, it is important to note that this is based on the assumption that fretting fatigue will always lead to micro-crack development.

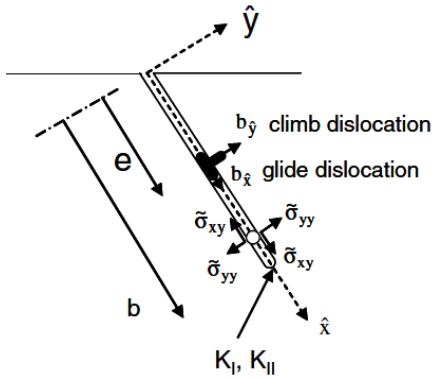

Figure 2.4 Schematic of oblique crack growth under mixed mode I&II conditions [Fouvry et al., 2008]

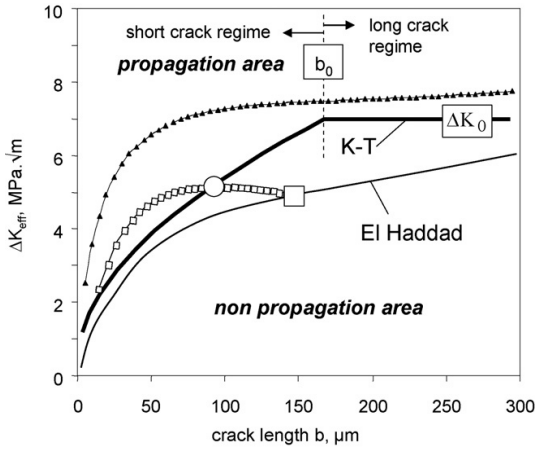

Figure 2.5 Kitagawa-Takahashi (K-T) and El Haddad diagrams for micro-crack thresholds [Fouvry et al., 2008]

2.2 Crack initiation based criteria

2.2.1 Uniaxial fatigue criteria

Fatigue problems were first studied by Wöhler in the 1880s. He developed a uniaxial stress-life approach (S-N curve: Figure 2.6) for designing finite fatigue lifetime. Basquin modified the Wöhler curve to a strain-life curve for the high cycle fatigue regime and found a linear relationship between elastic strain, $\Delta\varepsilon_e$, and lifetime in a double logarithmic diagram, equation (2-12).

$$\left(\frac{\Delta\varepsilon}{2}\right)_e = \frac{\left(\sigma_f'\right)}{E}\left(2N_i\right)^m \qquad \textbf{(2-12)}$$

In the elastic range, also the maximum normal stress can be correlated to lifetime as follows: $\sigma_{max} = E(\Delta\varepsilon/2)_e = \sigma_f'(2N_i)^m$.

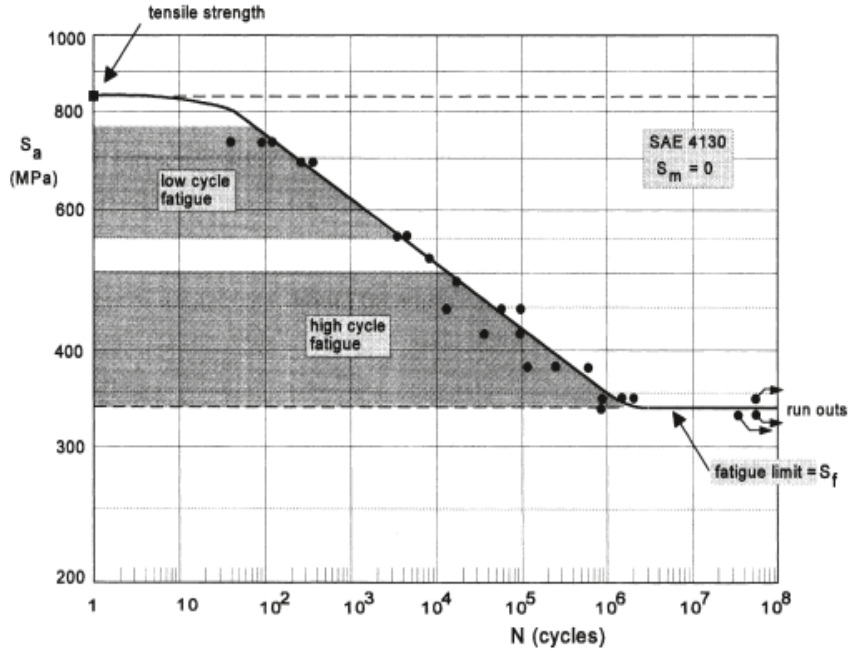

Figure 2.6 S-N curve of unnotched specimens of a low-alloy steel (SAE 4130) [Schijve J, 2009]

Manson and Coffin later observed a linear relationship between the logarithm of plastic strain and the logarithm of lifetime for a wide range of materials (see equation (2-13)). Using the plastic strain instead of stress allows a better representation of the fatigue lifetime curve in the low cycle region (see Figure 2.6 and Figure 2.7). Manson and Hirschberg used both elastic and plastic strains to correlate with fatigue crack initiation lifetime as in equation (2-14) [Schijve J, 2009]. In this sense, the plastic strain is also included in lifetime prediction even for high cycle fatigue which is motivated by the fact that localized plasticity also occurs in high cycle fatigue. Here, σ_f' is a fatigue strength coefficient, m is a fatigue strength exponent, ε_f' is a fatigue ductility coefficient and n is a fatigue ductility exponent. These constants are to be determined by curve fitting to experimental data from both low and high cycle fatigue experiments (see Figure 2.7). The lifetime considered here should be the crack initiation proportion only. However, since the determination of crack initiation lifetime as a function of the controlled strain is difficult, sometimes total lifetime is used instead.

$$\left(\frac{\Delta\varepsilon}{2}\right)_{pl} = \varepsilon_f'(2N_i)^n \tag{2-13}$$

$$\left(\frac{\Delta\varepsilon}{2}\right)_t = \left(\frac{\Delta\varepsilon}{2}\right)_e + \left(\frac{\Delta\varepsilon}{2}\right)_{pl} = \frac{(\sigma_f')}{E}(2N_i)^m + \varepsilon_f'(2N_i)^n \tag{2-14}$$

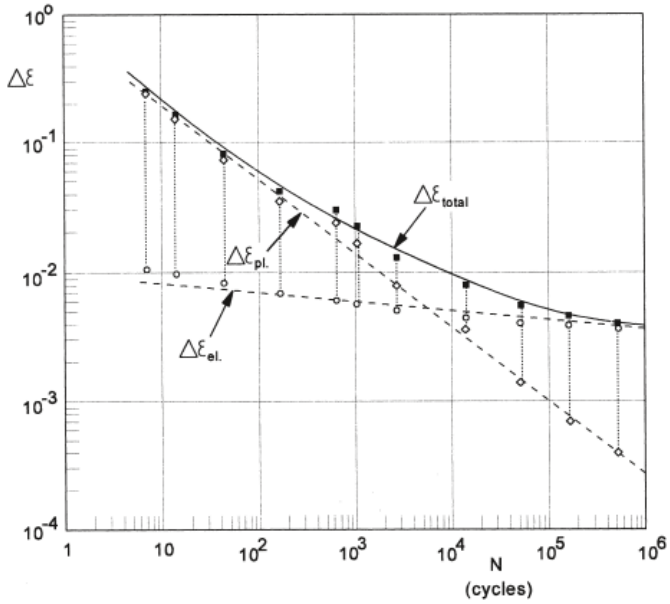

Figure 2.7 Strain-life diagram with the total strain range equal to the sum of the plastic and the elastic strain range. Material: AISI 4340 (annealed) [Schijve J, 2009]

2.2.2 Multiaxial fatigue criteria

The above mentioned relations are a satisfactory tool for crack initiation prediction for several materials but completely fail to interpret more complex fatigue problems such as combined loadings or fatigue of notched specimens. However, these uniaxial fatigue relations are the basis for prediction of crack initiation lifetime under more complex stress states. Multiaxial fatigue criteria are categorized into three main approaches: equivalent stress and strain, energy loss and critical plane approaches [You & Lee, 1996]. Instead of the applied total strain amplitude, a multiaxial damage parameter is used to calculate the crack initiation lifetime. To limit the length of this thesis, only the criteria applied to fretting fatigue are discussed.

Smith-Watson-Topper (SWT) proposed a multiaxial fatigue criterion based on the multiplication of the maximum principal strain, $\Delta\varepsilon_1$, and the maximum stress normal to that plane, σ_1^{max}, equation (2-15). On the other

hand, McDiarmid and Fatemi & Socie (FS) proposed a multiaxial parameter based on maximum shear stress, $\Delta\tau_{max}$, and maximum shear strain, $\Delta\gamma_{max}/2$, as shown in equations (2-16) and (2-17), respectively. Here, τ_{fl} is the shear fatigue limit, σ_y and σ_{ult} are the yield and ultimate strength respectively, and a is a constant fitted to uniaxial torsion tests. These three criteria are critical plane based since the defined maximum principal strain, shear stress or shear strain are on a plane which experiences this maximum value within a load cycle. In this sense, these criteria can also predict the plane of crack initiation. These critical plane criteria have been developed based on physical crack initiation observed in experiments. It is believed that for crack initiation, which is controlled by shear for most ductile materials, the SWT criterion shows less accuracy. The Crossland multiaxial fatigue criterion on the other hand, is based on an equivalent stress at a certain point, area or volume as shown in equation (2-18) where $J_{2,a}$ is the amplitude of the second invariant of the deviatoric stress tensor, $I_{1,max}$ is the maximum of the first invariant stress tensor, and $\sigma_{b,fl}$ is the bending fatigue limit.

$$SWT = \left(\sigma_1{}^{\max} \frac{\Delta\varepsilon_1}{2} \right) \tag{2-15}$$

$$McDiarmid = \left(\frac{\Delta\tau_{\max}}{2} + \frac{\tau_{fl}}{2\sigma_{ult}} \sigma_{\max} \right) \tag{2-16}$$

$$FS = \frac{\Delta\gamma_{\max}}{2} \left(1 + \alpha \frac{\sigma_{\max}}{\sigma_y} \right) \tag{2-17}$$

$$Crossland = \sqrt{J_{2,a}} + \frac{I_{1,\max}}{3} \left(\frac{3\tau_{fl}}{\sigma_{b,fl}} - \sqrt{3} \right) \tag{2-18}$$

Materials subjected to an identical multiaxial damage parameter are hypothesized to have the same crack initiation time. Therefore, the crack initiation time under multiaxial fatigue could be determined based on experimental results of uniaxial fatigue with the same damage parameter. An excellent review can be found in [Navarro, Munoz & Dominguez, 2008]. In that work the Basquin equation is used instead of equation (2-14) for the reason that stress levels in fretting fatigue conditions are elastic.

$$SWT = \sigma_{\max} \left(\frac{\Delta\varepsilon_1}{2} \right) = \frac{\left(\sigma_{f'} \right)^2}{E} \left(2N_i \right)^{2m} + \sigma_{f'} \varepsilon_{f'} \left(2N_i \right)^{m+n} \tag{2-19}$$

[Szolwinski & Farris, 1998, 1996] applied the SWT criterion in fretting fatigue to predict crack initiation lifetime. However, this model could not take the

size effect into account. [Fouvry, Kapsa & Vincent, 2000] incorporated for the first time the size effect into multiaxial fatigue models by averaging the multiaxial fatigue parameters over an area instead of taking the value for a single critical point (see Figure 2.8).

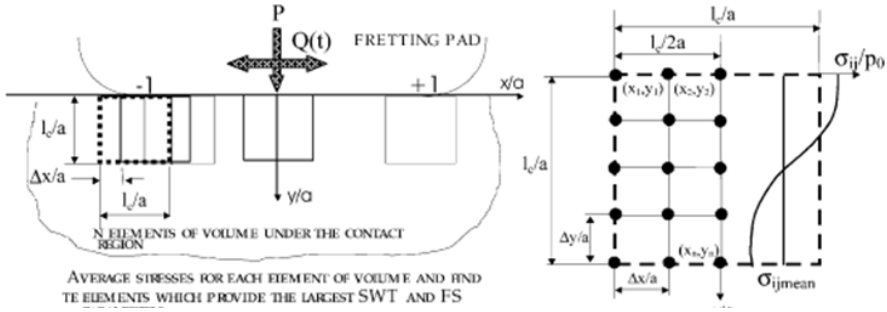

Figure 2.8 Averaging area approach to incorporate the size effect [Araújo & Nowell, 2002]

[Araújo & Nowell, 2002] adopted this methodology and implemented it into the criteria of SWT and FS. They concluded that this approach could explain the size effect but an issue was a suited selection of the dimensions of the averaging area. [S Fouvry & Kubiak, 2009] defined the dimensions of this area by a calibration based on a plain fretting test but the error of the predicted results compared to fretting fatigue experiments was around *10 %*. An identical value of the calibrated area was used for all load conditions considering it as a material property. [Fouvry, Gallien & Berthel, 2014] determined a correlation between the stress gradient and the area to be averaged, i.e. the dimension to be averaged depends on the stress gradient within the contact zone. In this way, the error on loading conditions leading to crack initiation between the model and the experiment was reduced to be less than *5 %*. This implies that this averaging area may not be a material property but dependent on the stress states.

On the other hand, when multiaxial fatigue criteria are used to predict the fretting fatigue limit in the high cycle fatigue regime, i.e. higher than 10^6 cycles, the multiaxial fatigue parameters as defined by Crossland and McDiarmid can be simply compared to the shear fatigue limit, τ_{fl} [S. Fouvry & Kubiak, 2009].

2.2.3 Ruiz criterion

The size effect of fretting fatigue may suggest that a stress-based approach alone is not sufficiently effective to predict fretting fatigue lifetime. Some researchers analyse fretting fatigue lifetime as a function of slip amplitude solely [Vingsbo & Söderberg, 1988]. [Ruiz, Boddington & Chen, 1984] combined stress-based parameters (σ_s and τ_s) with a slip amplitude (δ) to determine the location of crack initiation as well as to predict the lifetime.

The Ruiz crack initiation parameter is defined as the multiplication of these three parameters: $\sigma_s\tau_s\delta$. Here σ_s and τ_s are normal and shear stresses at the contact surface respectively, and δ is the relative slip amplitude. The quantity $\tau_s\delta$ represents the frictional energy loss to create a crack, while the stress σ_s represents the normal stress to open the crack after its nucleation. [Nowell & Hills, 1990] adopted the Ruiz crack initiation parameter to interpret the size effect. The criterion also allowed to predict the location of crack initiation at the trailing edge of the contact area which was confirmed experimentally. However, [Nowell & Hills, 1990] admitted that multiplying the frictional energy term by a normal stress is rather arbitrary and lacks physical background. Still, [Vidner & Leidich, 2007] adopted the criterion by calculation of stresses and strains using multiaxial fatigue criteria, Smith-Watson-Topper (SWT) and Fatemi-Socie (FS), in combination with a new parameter for frictional energy loss (see equations (2-20) & (2-21)). Again, these enhanced fretting fatigue damage parameters (eFFDPs) are rather arbitrary.

$$eFFDP = P^*_{fric} SWT \tag{2-20}$$

$$eFFDP = P^*_{fric}.FS \tag{2-21}$$

2.2.4 Micro-mechanical approaches

The above mentioned criteria are based on a macro-mechanical approach, i.e the parameters are defined by bulk stresses or strains. Another approach is the micro-mechanical one where stresses or strains are determined on a smaller scale, e.g. the size of a grain for the Dang Van criterion. [Fouvry, Kapsa & Vincent, 2000] adopted the Dang Van criterion to predict an infinite life condition. The criterion states that the fatigue limit of a material is obtained when there is a plastic shakedown on a specific grain. This approach can be extended to predict crack initiation lifetime, simply by correlating to uniaxial tensile test results as discussed in the section on multiaxial fatigue criteria. Another micro-mechanical approach is based on the crack formation itself, which means it does not only consider when a crack is formed but also how it is formed. Such approaches need experimental evidence of the crack formation process. In plain fatigue, this crack formation can be visualized by optical microscopy or video recordings since it mostly occurs at the free surface of a specimen. However, in fretting fatigue the zone of crack initiation is hidden in a closed contact and it is therefore deemed impossible to monitor this process during the test. [Fellows, Nowell & Hills, 1997] have attempted to collect this information off-line by firstly separating the crack initiation and propagation stages with their bi-actuator fretting fatigue test rig, but it was deemed impossible to detect crack initiation. Although lacking experimental proof of the crack formation process, [Fellows, Nowell & Hills, 1997] proposed a hypothesis

assuming an identical crack formation process as in plain fatigue (see Chapter 1.1.2.2 for more details). Crack initiation is a result of cyclic slip activity. An intrusion created by the cyclic clip may be accelerated by the fretting induced stress raiser. Even though also an extrusion is sometimes created, this extrusion will be removed by slip of the micro-slipping so that a crack is initiated as shown in Figure 2.9. The developed slip band theory for crack initiation in plain fatigue [Mura, 1994] was then utilized. The hypothesis was expected to be verified by comparison of the predicted lifetime with experimental data of crack initiation lifetime. As mentioned earlier it was not possible to detect the crack initiation with the bi-actuator test rig, so the hypothesis remains unverified even though the model was well developed.

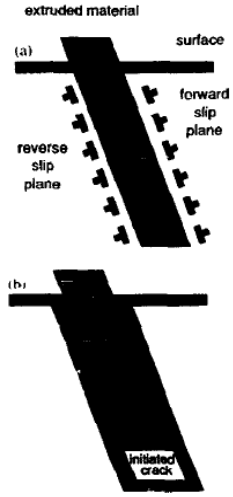

Figure 2.9 Assumed crack formation process under fretting fatigue [Fellows, Nowell & Hills, 1997]

3 Non-destructive methods for fretting damage inspection

The potential drop technique was applied to fretting fatigue tests by [Kondo et al., 2005] and [Meriaux et al., 2010b]. Different calibration techniques to establish the relation between voltage and crack length had been used. The former relied on a plain fatigue test of a pre-cracked specimen while the latter performed a fretting fatigue test for the calibration. The latter procedure for the calibration is rather complex. Both of them achieved a detection of short cracks, around *50* µm. With a small detection threshold, [Meriaux et al., 2010a] extended the experimental investigation to quantify fretting fatigue crack growth modes. [De Pannemaecker et al., 2017] used the X-ray synchrotron technique to monitor the crack propagation rate during a fretting fatigue test. The feasibility of this technique could only be

demonstrated for crack depths larger than *100* µm and a specimen thickness of *2* mm. Such thin specimen simulates fretting fatigue under plane stress conditions, whilst in practical applications components are likely to fail in plane strain conditions [Johnson, 1985]. [Endo & Goto, 1976] developed an experimental technique based on optical microscopy and electrical resistance to investigate fretting fatigue crack initiation and propagation under fully reversed bending. Due to this finding, [Sato & Fujii, 1986] used a travelling microscope with an accuracy of *1* µm to investigate crack growth rate in fretting fatigue experiments. In their experiments, fretting fatigue cracks may have been forced to reach the front surface where the optical devices were installed. The reported non-destructive techniques allow to detect the moment of crack initiation and/or to study the crack growth rate. However, the accumulated damage prior to crack initiation cannot be investigated. This process remains the most difficult one to understand in fretting fatigue.

[Forsyth et al., 2007] evaluated different non-destructive methods for inspection of fretting damage on aeroplane fuselage structures, particularly at rivets. A coupon type test was performed on two aluminium sheets fastened by rivets. Infrared thermography was shown to be the best candidate to quantify fretting damage during off-line inspection among other NDT techniques such as ultrasonic inspection, X-ray radiography and eddy current. Ultrasonic inspection demonstrated some promising results too, but could not distinguish between fretting damage and machining defects whereas eddy current and radiography did not show any indications of damage. Infrared thermography was then selected to monitor damage during the test and showed potential to detect crack initiation. [Berthel et al., 2014] utilized the thermography technique to analyse and separate the surface damage due to friction on the one hand and due to plasticity on the other hand. [Szolwinski et al., 1999] attempted to measure a full-field temperature distribution near the contact under fretting fatigue. This temperature distribution allowed them to visualize the transition from gross slip to stabilized partial slip regime during the early stages of fretting fatigue tests.

4 Infrared thermography for damage investigation under cyclic loading

In principle, thermography is a technique which provides an image of the distribution of temperature at the surface of an examined object. Thermal images are actually visual displays of the amount of infrared energy emitted, transmitted and reflected by an object. Two important temperature responses due to cyclic loading have been observed: a thermoelastic effect and a plasticity-induced heat dissipation. With either response, rapid fatigue limit determination and detection of fatigue crack initiation have been achieved.

4.1 Fatigue limit

A sequence of block loads with increased stress level (see Figure 2.10) was applied to estimate fatigue properties of materials. These tests are normally very short in duration (a few hours) and non-destructive in nature. Measuring the intrinsic heat dissipation based on differential thermography allowed [Luong, 1998; Rosa & Risitano, 2000] to determine the loading block which corresponds to the fatigue limit of coupon specimens and real mechanical components. Coupling the measured heat dissipation with different damage models, [Fargione et al., 2002] could rapidly construct a complete S-N curve of materials, whereas [Risitano & Risitano, 2010] were capable to predict a residual fatigue life of materials.

Performing similar block loading sequences, [Krapez, Pacou & Gardette, 2000] utilized a signal processing method, least squares curve fitting, to separate the temperature responses into three effects as shown in equation (2-22): the thermoelastic effect (first harmonic: $T_1 sin(2\pi ft+\phi_1)$), the inelastic effect (second harmonic: $T_2\ sin(4\pi ft+\phi_2)$), and the self-heating effect (linear drift: $\Delta T t.f$). They used parameters T_1 and T_2 as indicators to define the loading block corresponding to the fatigue limit of the materials.

$$T_{\exp}(t) = \Delta T.t.f + T_1 Sin(2\pi ft + \varphi_1) + T_2 Sin(4\pi ft + \varphi_2) \qquad \textbf{(2-22)}$$

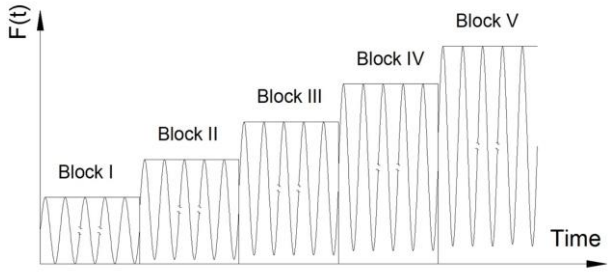

Figure 2.10 Typical sequential block loads used for rapid determination of fatigue limit

4.2 Crack initiation detection

4.2.1 Plain fatigue

[Ranc, Wagner & Paris, 2008] developed an experimental set-up to investigate the proportion of crack initiation time to total lifetime in the giga-cycle regime. Since the giga-cycle regime extends beyond 10^7 cycles, the fatigue machine was equipped with an ultrasonic actuator to be able to finish testing in a reasonable time. Specific for this type of test is that the location with the highest stress, i.e. the center of the specimen, is stationary even though the other parts are subjected to cyclic deformation. Therefore it is not necessary to record several thermal images for one load cycle and storage

issues are avoided. The loading frequency was *20* kHz while the thermal images were recorded with a framerate of *10* or *100* Hz. The experimental data is shown in Figure 2.11 with some level of signal-to-noise ratio. A data fitting procedure was performed to reduce the signal-to-noise ratio and thus the crack size detection limit as much as possible. When the filtered temperature data rose above the stabilized temperature (the horizontal line), it was defined as the moment of crack initiation. With a filtered signal-to-noise ratio of *70* mK, a crack size of *40* μm was detected.

[Plekhov et al., 2005] monitored surface crack growth during bending fatigue tests by analysing the evolution of the standard deviation of spatial temperature within several regions of interest around a visualized hot spot, Figure 2.12a. The regions of interest are coaxial circles with different radii. One region of interest is located outside the hot spot as a reference. When a crack is not initiated, the temperature within all the regions of interest is homogeneous, so its standard deviation is stabilized (see Figure 2.12b). Crack initiation is detected when the standard deviation of the spatial temperature around the hot spot increases from the stabilized regime, as the crack disturbs the homogeneous temperature distribution of that region of interest. When a crack extends out of a region of interest, the corresponding temperature distribution returns to be less heterogeneous, i.e a drop of its standard deviation can be noticed. Then the standard deviation of the spatial temperature of nearby or surrounding regions of interest increases. Some types of infrared camera allow direct determination of the standard deviation of spatial temperature, so this approach can be implemented as on-line technique if the computational speed is fast enough.

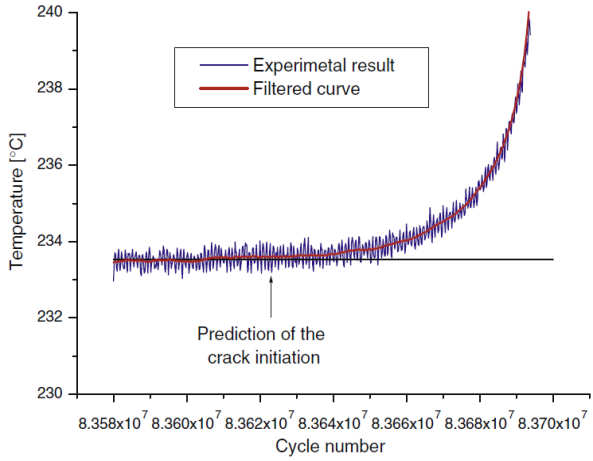

Figure 2.11 Temperature variation during a giga-cycle fatigue test [Ranc, Wagner & Paris, 2008]

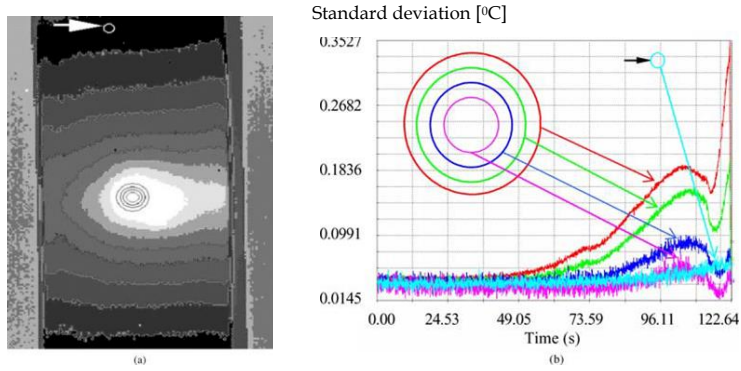

Figure 2.12 a) Hot spot on the specimen surface b) Evolution of the standard deviation of spatial temperature distribution within regions of interest around the hot spot [Plekhov et al., 2005]

[Ummenhofer & Medgenberg, 2009] detected fatigue crack initiation of a welded joint by analyzing linear (thermoelastic) and non-linear effects and phase differences of thermal images. Intermittent series of thermal images were captured because of storage problems and signal processing was performed to all data series. Motion compensation was desired for this pixel data processing since elastic deformation causes changes to the field of view of each pixel during fatigue loading. A procedure to separate these effects for each pixel is shown in Figure 2.13.

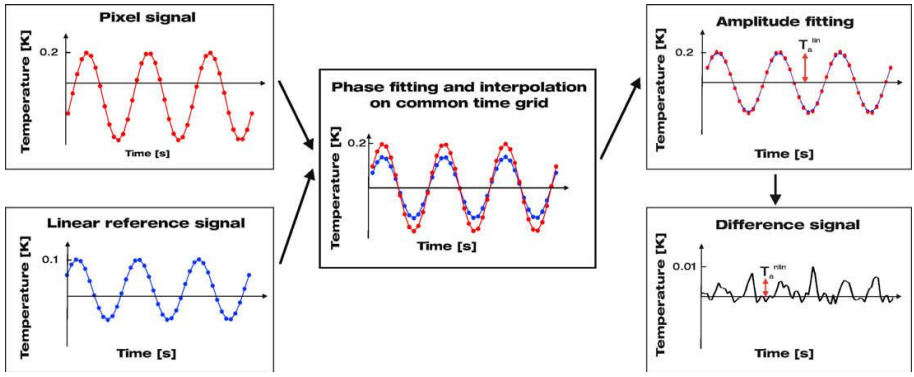

Figure 2.13 Schematic representation of data processing process [Ummenhofer & Medgenberg, 2009]

First, a linear reference signal is phase fitted and interpolated with the measured temperature data points. Then an amplitude normalization is conducted to extract the linear temperature amplitude. In the end, the difference between the measured temperature and the fitted linear temperature amplitude gives the non-linear effect. Actually, the linear and non-linear effects correspond to the thermo-elastic and the in-elastic effects respectively, as mentioned by [Krapez, Pacou & Gardette, 2000]. Figure 2.14 illustrate thermal images corresponding to these different effects and its

corresponding visual image. Occurrence of cracks at the surface led to a change of these two effects so that crack initiation could be detected.

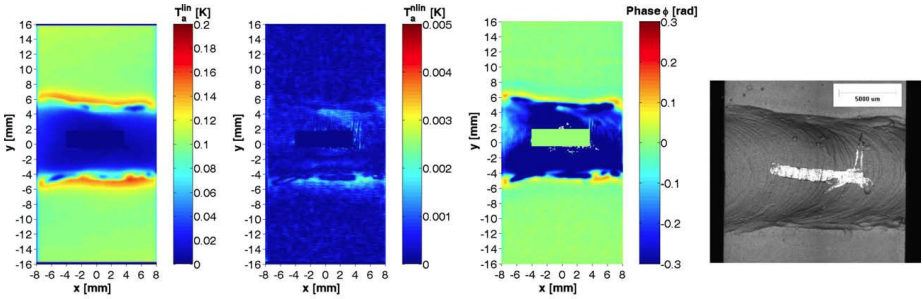

(a) linear temperature amplitude (b) nonlinear temperature amplitude (c) relative phase (d) surface image

Figure 2.14 Thermal images separation with a pixel data processing method [Ummenhofer & Medgenberg, 2009]

4.2.2 Plain fretting

The principle of sequential block loads was also adopted in plain fretting tests. Similarly to [Krapez, Pacou & Gardette, 2000], [Berthel et al., 2014] applied the least mean squares algorithm to distinguish different temperature responses in plain fretting tests: the first harmonic, the second harmonic, and the linear drift. Parameters corresponding to these measured temperature responses are considered to include the thermoelastic and inelastic (friction and plasticity) effects. On the other hand, a developed thermo-fretting model covered the thermo-elastic effect and the frictional part of the inelastic effect. Comparisons of the measured temperature responses to those of the analytical model allowed to detect the plasticity effect of a specific load block. Therefore, the loading condition of that block was considered as fretting crack initiation condition in the high cycle regime, defined as 10^6 cycles.

5 Summary and conclusions

Most researchers consider the mechanics of crack propagation in fretting fatigue to be more or less resolved. Once the stress intensity factor can be determined, the problems of fretting fatigue are not very much different from plain fatigue, thanks to the theory of fracture mechanics. Of course the complexity of the stress components added by the contact loading and the feasibility of fracture mechanics concepts to be applied to a micro-crack needs to be carefully addressed.

Both macro-mechanical and micro-mechanical approaches have allowed to yield reasonable predictions of fretting fatigue crack initiation, taking the size effect into account. These models are based on an individual hypothesis and validated by the time a crack is considered to be initiated. Off-line optical

microscopy is normally adopted for crack inspection. The hypothesis related to the crack formation process remains the most challenging one to proof experimentally, since there is no chance to visualize this process on-line in a closed contact. Only a very limited amount of non-destructive techniques have been demonstrated to be feasible for fretting fatigue. Such advanced inspection techniques are however necessary since they could provide an on-line detection of the crack initiation. Procedures based on intermittent stopping and restarting experiments to allow for off-line optical inspection cannot guarantee that identical contact conditions are maintained.

The feasibility of infrared thermography to detect damage and crack initiation due to cyclic load such as plain fatigue and plain fretting has been demonstrated in literature. This technique was furthermore evaluated to be the best candidate for inspection of fretting fatigue damage in a riveted lap joint and for off-line fretting fatigue crack initiation. In this thesis, this technique will be adopted to investigate fretting fatigue damage and crack initiation.

References

Araújo, J.A., Nowell, D. (1999) Analysis of Pad Size Effects in Fretting Fatigue Using Short Crack Arrest Methodologies. *International Journal of Fatigue*, 21, 947–56.

Araújo, J.A., Nowell, D. (2002) The Effect of Rapidly Varying Contact Stress Fields on Fretting Fatigue. *International Journal of Fatigue*, 24, 763–75.

ASTM-E647-08 (2009) Standard Test Method for Measurement of Fatigue Crack Growth Rates 1.

Berthel, B., Moustafa, A.-R., Charkaluk, E., Fouvry, S. (2014) Crack Nucleation Threshold under Fretting Loading by a Thermal Method. *Tribology International*, 76, 35–44.

De Pannemaecker, A., Buffiere, J.Y., Fouvry, S., Graton, O. (2017) In Situ Fretting Fatigue Crack Propagation Analysis Using Synchrotron X-Ray Radiography. *International Journal of Fatigue*, 97, 56–69.

El Haddad, M.., Smith, K.N., Topper, T.H. (1979) Fatigue Crack Propagation of Short Cracks. *Journal of Engineering Materials and Technology*, 101, 42–6.

Endo, K., Goto, H. (1976) Initiation and Propagation of Fretting Fatigue Cracks. *Wear*, 38, 311–24.

Fargione, G., Geraci, A., Rosa, G. La, Risitano, A., Doria, V.A. (2002) Rapid Determination of the Fatigue Curve by the Thermographic Method. *International Journal of Fatigue*, 24, 11–9.

Fellows, L.J., Nowell, D., Hills, D.A. (1997) On the Initiation of Fretting Fatigue Cracks. *Wear*, 205, 120–9.

Forsyth, D., Genest, M., Shaver, J., Mills, T. (2007) Evaluation of Nondestructive Testing Methods for the Detection of Fretting Damage. *International Journal of Fatigue*, 29, 810–21.

Fouvry, S., Gallien, H., Berthel, B. (2014) From Uni- to Multi-Axial Fretting-Fatigue Crack Nucleation : Development of a Stress-Gradient-Dependent Critical Distance Approach. *International Journal of Fatigue*, 62, 194–209.

Fouvry, S., Kapsa, P., Vincent, L. (2000) A Multiaxial Analysis of Fretting Contact Taking into Account the Size Effect. In *Fretting Fatigue: Current Technology and Practices, ASTM STP 1367, D. W. Hoeppner, V. Chandraskaran, and C. B. Elliot*. ASTM, West Conshohocken, PA.

Fouvry, S., Kubiak, K. (2009) Introduction of a Fretting-Fatigue Mapping Concept: Development of a Dual Crack Nucleation – Crack Propagation Approach to Formalize Fretting-Fatigue Damage. *International Journal of Fatigue*, 31, 250–62.

Fouvry, S., Kubiak, K. (2009) Development of a Fretting–fatigue Mapping Concept: The Effect of Material Properties and Surface Treatments. *Wear*, 267, 2186–99.

Fouvry, S., Nowell, D., Kubiak, K., Hills, D. a. (2008) Prediction of Fretting Crack Propagation Based on a Short Crack Methodology. *Engineering Fracture Mechanics*, 75, 1605–22.

Hills, D.A., Nowell, D. (1994) *Mechanics of Fretting Fatigue*. Kluiwer Academic Publishers, Dordrecht.

Hills, D.A., Nowell, D. (2014) Mechanics of Fretting fatigue—Oxford's Contribution. *Tribology International*, 76, 1–5.

Hills, D.A., Nowell, D., O'Connor, J.J. (1988) On the Mechanics of Fretting Fatigue. *Wear*, 125, 129–46.

Johnson, K.L. (1985) *Contact Mechanics*. Cambridge University Press.

Kitagawa, H., Takahashi, S. (1976) Application of Fracture Mechanics to Very Small Cracks or the Cracks in the Early Stage. *American society of metals*, 627–30.

Kondo, Y., Sakae, C., Kubota, M., Yanagihara, K. (2005) Non-Propagating Crack Behaviour at Giga-Cycle Fretting Fatigue Limit. *Fatigue Fracture of Engineering Materials and Structures*, 28, 501–6.

Krapez, J.C., Pacou, D., Gardette, G. (2000) Lock-in Thermography and Fatigue Limit of Metals. In *Quantitative Infrared Thermography 5*. pp. 277–82.

Luong, M.P. (1998) Fatigue Limit Evaluation of Metals Using an Infrared Thermographic Technique. *Mechanics of Materials*, 28, 155–63.

Meriaux, J., Boinet, M., Fouvry, S., Lenain, J.C. (2010a) Identification of Fretting Fatigue Crack Propagation Mechanisms Using Acoustic Emission. *Tribology International*, 43, 2166–74.

Meriaux, J., Fouvry, S., Kubiak, K.J., Deyber, S. (2010b) Characterization of Crack Nucleation in TA6V under Fretting–fatigue Loading Using the Potential Drop Technique. *International Journal of Fatigue*, 32, 1658–68.

Miller, K.J. (1993) The Two Thresholds of Fatigue Behaviour. *Fatigue & Fracture of Engineering Materials & Structures*, 16, 931–9.

Mugadu, A., Hills, D.A., Nowell, D. (2002) Modifications to a Fretting-Fatigue Testing Apparatus Based upon an Analysis of Contact Stresses at Complete and Nearly Complete Contacts. *Wear*, 252, 475–83.

Mura, T. (1994) A Theory of Fatigue Crack Initiation, 176, 61–70.

Navarro, C., Munoz, S., Dominguez, J. (2008) On the Use of Multiaxial Fatigue Criteria for Fretting Fatigue Life Assessment. *International Journal of Fatigue*, 30, 32–44.

Nowell, D., Dini, D., Hills, D.A. (2006) Recent Developments in the Understanding of Fretting Fatigue. *Engineering Fracture Mechanics*, 73, 207–22.

Nowell, D., Hills, D. a. (1990) Crack Initiation Criteria in Fretting Fatigue. *Wear*, 136, 329–43.

Plekhov, O., Palin-Luc, T., Saintier, N., Uvarov, S., Naimark, O. (2005) Fatigue Crack Initiation and Growth in a 35CrMo4 Steel Investigated by Infrared Thermography. *Fatigue Fract. Engng Mater. Struct*, 28, 169–78.

Ranc, N., Wagner, D., Paris, P.C. (2008) Study of Thermal Effects Associated with Crack Propagation during Very High Cycle Fatigue Tests. *Acta Materialia*, 56, 4012–21.

Risitano, A., Risitano, G. (2010) Cumulative Damage Evaluation of Steel Using Infrared Thermography. *Theoretical and Applied Fracture Mechanics*, 54, 82–90.

Rosa, G. La, Risitano, A. (2000) Thermographic Methodology for Rapid Determination of the Fatigue Limit of Materials and Mechanical Components. *International Journal of Fatigue*, 22, 65–73.

Ruiz, C., Boddington, P.H.B., Chen, K.C. (1984) An Investigation of Fatigue and Fretting in a Dovetail Joint. *Experimental Mechanics*, 24, 208–17.

Sato, K., Fujii, H. (1986) Crack Propagation Behaviour in Fretting Fatigue. *Wear*, 107, 245–62.

Schijve J (2009) *Fatigue of Structures and Materials*. Springer Science+ Business Media, B. V.

Szolwinski, M.P., Farris, T.N. (1996) Mechanics of Fretting Fatigue Crack Formation. *Wear*, 98, 93–107.

Szolwinski, M.P., Farris, T.N. (1998) Observation, Analysis and Prediction of Fretting Fatigue in 2024-T351 Aluminum Alloy. *Wear*, 221, 24–36.

Szolwinski, M.P., Harish, G., Farris, T.N., Sakagami, T. (1999) In-Situ Measurement of Near-Surface Fretting Contact Temperatures in an Aluminum Alloy. *Journal of Tribology-Transactions of the ASME*, 121, 11–9.

Ummenhofer, T., Medgenberg, J. (2009) On the Use of Infrared Thermography for the Analysis of Fatigue Damage Processes in Welded Joints. *International Journal of Fatigue*, 31, 130–7.

Vidner, J., Leidich, E. (2007) Enhanced Ruiz Criterion for the Evaluation of Crack Initiation in Contact Subjected to Fretting Fatigue. *International Journalof Fatigue*, 29, 2040–9.

Vingsbo, O., Söderberg, S. (1988) On Fretting Maps. *Wear*, 126, 131–47.

You, B., Lee, S. (1996) A Critical Review on Multiaxial Fatigue Assessments of Metals. *International Journal of Fatigue*, 18, 235–44.

Chapter 3 Fretting fatigue tests

"Challenges and efforts for exploiting experimental results from laboratory tests to real fretting problems are presented. The functionality of the test rig used in the current study is elaborated."

1 Introduction

A first purpose of fretting fatigue experiments is to calibrate or evaluate theoretical models that allow to calculate stress, strain, and displacement fields for a certain contact shape and dimension. A second and more challenging purpose of fretting fatigue experiments is to investigate damage evolution in terms of friction, wear, fatigue crack initiation and propagation. Friction seems to be easily given by some theories (eg. Coulomb friction), but in practice, friction and also wear can be affected by many factors such as roughness, contact type, load, speed, material type, etc. Adequate crack initiation models are selected based on experimental evidence of crack initiation features. These can vary based on loading conditions and material used. For ductile materials, cracks are likely nucleated in a shear mode while cracks may be nucleated in a tensile mode for brittle materials. In low and high cycle fatigue regimes, cracks typically nucleate from a free surface while in ultra-high cycle fatigue, cracks will in most cases nucleate subsurface from material imperfections like inclusions. Modelling crack propagation requires experimental proof of, at least, crack path and crack propagation modes.

When fretting fatigue tests would allow to separate crack initiation and crack propagation lifetime, evidently an improved understanding of the mechanics of fretting fatigue could be accomplished. In addition, influences of loading conditions, load histories, different material types and combinations, and surface treatment can also be studied. [Hills & Nowell, 1994] have reported that fretting fatigue tests can be divided into three general categories.

1. *Simulation of a real engineering fretting problem.* The intention of this type of tests is to reproduce as careful as possible the fretting contact conditions occurring in service, either on a full scale or on a medium scale. Experimental results are expected to be transferrable to the real engineering problem without modifications. One of the most significant works related to this type of test, was conducted by [Ruiz, Boddington & Chen, 1984] who developed a medium scale test set-up, Figure 3.1, to simulate the contact of a turbine blade against its disk. A failed blade sample is shown in Figure 3.2. However, attention should be paid to two critical points raised by [Hills & Nowell, 1994] for this type of test. The first one is the size effect when dimensions of a tested sample are smaller than the prototype's dimensions. Indeed, a smaller contact area may lead to a different slip amplitude, which is an additional critical parameter for fretting fatigue lifetime besides local stresses and strains. This challenge is already a major concern from a macroscopic perspective before looking into a more complex topography at the level of asperities. A second attention point is the presence of machining imperfections even though global dimensions of the sample are identical to the prototype. A minor machining defect could cause a

different contact distribution for the same contact pair, particularly if it is a complete contact.

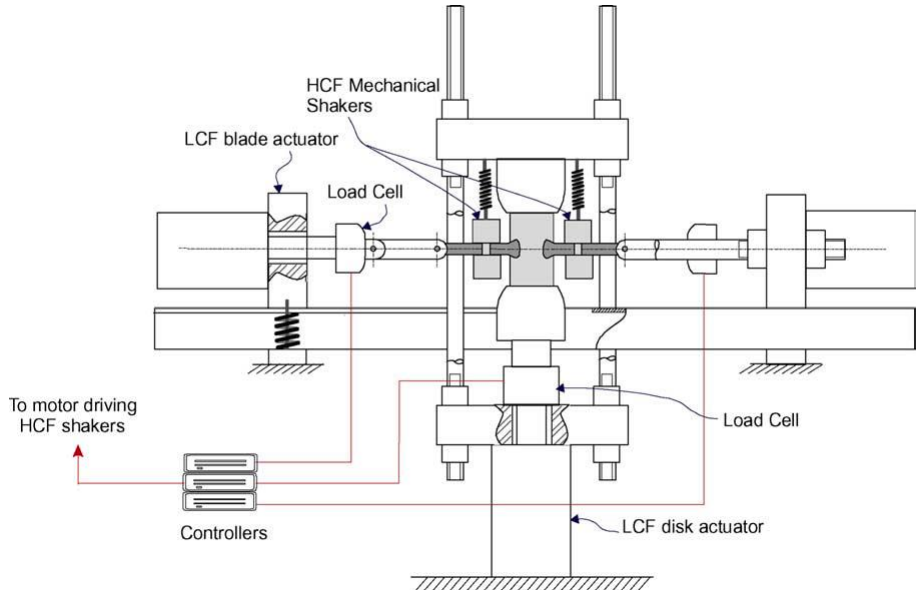

Figure 3.1 Apparatus for fretting fatigue test of turbine blade vs disk [Nowell, Dini & Hills, 2006]

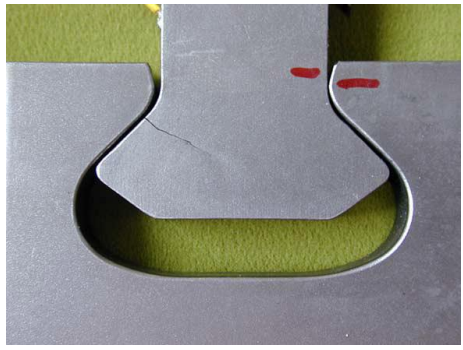

Figure 3.2 Failed blade specimen [Nowell, Dini & Hills, 2006]

2. *Material ranking tests*. The intention of these tests is to compare the fretting fatigue strength of different materials or the efficiency of different surface treatment techniques. A simplified contact geometry is selected to ensure rapid experimental preparation and testing without paying too much attention to the contact details. However, the selected contact geometry should allow a repetition from one test to another. A good example of this test type is a concept proposed by [Hills & Nowell, 1994] to adopt a rotary four point bending test used by Wöhler to evaluate fatigue behaviour of train axles as sketched in Figure 3.3. The specimen is clamped by

bridge pads having flat feet (bridge method) via a proving ring. The proving ring can float freely over the specimen and rotate together with the specimen during the test. The cross-section of the specimen is subjected to a typical distribution of tensile and compressive stresses due to the bending load. Combined with specimen rotation, fluctuating tensile and compressive stresses over the cross-section of the specimen allow to control the desired relative slip at the bridge feet. In this test, the contact configuration is simple and the speed of the test can be high since the motion is continuous, which can avoid inertia effects. Attention is to be paid to the balancing of the bridge pads during the rotation of the specimen.

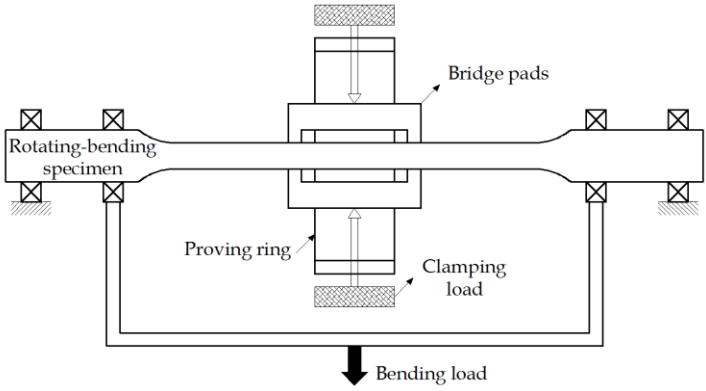

Figure 3.3 Bridge type rotary bending test

3. *Idealised fretting fatigue tests*. The intention of these tests is to generate ample experimental data that allow to support the development of fundamental understanding of the mechanics of fretting fatigue process. The contact type should be well defined and allow analytical determination of stress, strain, displacement, relative slip etc. The knowledge gained from these tests should be generic or true for other contact types or even real engineering problems.

Apart from the second type of test, the other two test types share a common purpose of providing results which can be used to understand the fretting fatigue behaviour of real industrial cases. The first method is of course more expensive but could provide a direct insight into the real contact taking into account the two attention points mentioned earlier while the third method is not straightforward. An intermediate modelling step is required to get some insights into the real problems. However, it provides a basic tool for a complete understanding of fretting fatigue. In the following section, the evolution of fretting fatigue test configurations related to the last category is presented.

2 Evolution of idealised fretting fatigue test configurations

2.1 Single actuator test rig

In principle, fretting tests should be performed under partial slip or gross slip conditions, which requires a well-controlled displacement in the order of several microns. These slip regimes may occur at displacements below *50* μm. In practice, it was quite difficult to generate and control this magnitude of displacement by external actuators or cams, as any linkage of actuators should have a similar compliance to that of the contact [Hills & Nowell, 1994]. In addition, it was not easy to measure a displacement of that level. An alternative is to exploit self-compliance of the specimen to generate a desired tangential displacement when the bulk fatigue load is applied by an actuator. In this kind of tests, one of the approaches was to use two physically separated contacts in the form of a floating bridge [Hills & Nowell, 1994]. The compliance of the system could be controlled either by the specimen or by the bridge. Typically, the feet of the bridge pads were flat so that a complete contact was realized.

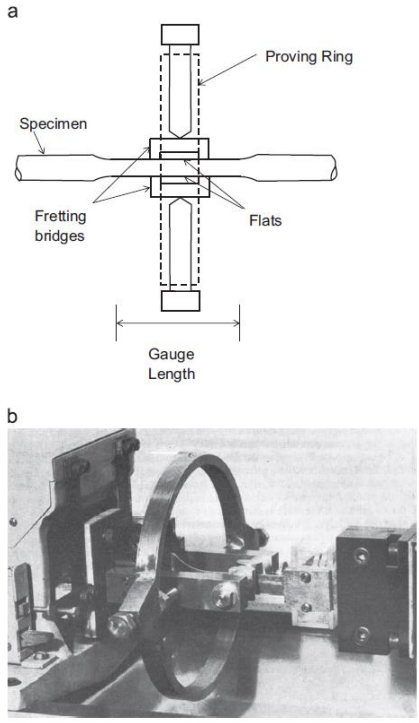

Figure 3.4 A floating fretting bridge type apparatus used by Fenner in 1950s [Hills & Nowell, 2014]

The bridge method to induce a relative slip is shown schematically in Figure 3.4a and as a picture in Figure 3.4b. The two bridges were clamped to a standard tensile specimen by a proving ring. The normal load to the specimen was controlled by tightening a screw-bolt system via the proving ring. The cyclic movement was obtained from an applied bulk reciprocating load on the specimen. In addition to the compliance of the specimen and the bridges, compliance of the proving ring also allowed to obtain a desired tangential displacement within the contact. Ideally, the sliding regime at the four contact points between the feet of the bridges and the specimen should have been be identical if the surface finish and cleanliness of the specimen was the same. But in practice, it was possible that each contact pair of the fretting bridges experienced a totally different sliding regime among the following three possibilities: complete stick, complete slip or mixed stick-slip. These floating fretting bridge type tests have been very popular from the 1950s until the 1990s [Nowell, Dini & Hills, 2006].

In order to avoid different mechanisms at the four bridge feet, an alternative was to rigidly fix a pair of the fretting bridges at one end and allow a motion at another end of the pair as shown in Figure 3.5. On the other hand, the stress state at the bridge feet was extremely difficult to be characterised as it was a complete contact. Stress singularity at the edges, machining imperfections, and bending of the bridge feet were major concerns. In case of a complete contact, a minor machining defect or a little tilt of the pad, intuitively, would not only lead to a localized zero contact pressure but also disturb the overall contact distribution. An option to avert these problems was that the contact configuration was changed from complete to incomplete contact. As can be seen in the figure, the flat faces on the fretting bridge pads were replaced by cylindrical faces. This change in contact configuration has been introduced by [Nishioka, K., Hirakawa, 1969].

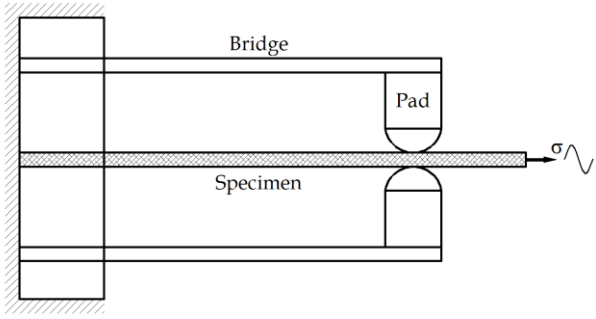

Figure 3.5 Fretting apparatus using cantilever springs to apply normal contact force

This pad configuration allows a closed form of contact stress solutions under partial slip regime as well as the analysis of the effect of the bulk fatigue load. A brief review was reported in Chapter 2.1. However, two problems need to be addressed: the edge effect and the alignment. Theoretically, the edge effect

cannot occur if the lengths of the cylinders in contact are infinite. In practice, an infinite length does not exist and stress concentration at the contact edges may occur. This edge effect can be reduced by using identical widths of pad and specimen. Alignment needs to be carefully made since rotation of the pad around any axis except the axis of the cylindrical pad will disturb the well-defined tractions, Figure 3.6. Even though rotation around the pad axis does not change the pressure distribution, part of the applied normal force is lost. If the pad face is axisymmetric (spherical), no misalignment is expected but this configuration results in a more complex stress state. Complete formulation of this contact shape under fretting fatigue is reported in [Hills & Nowell, 1994] and corresponding experimental works can be found in [Kuno, M., Waterhouse, R. B., Nowell, D., and Hills, 1989] and [Navarro, Munoz & Dominguez, 2008].

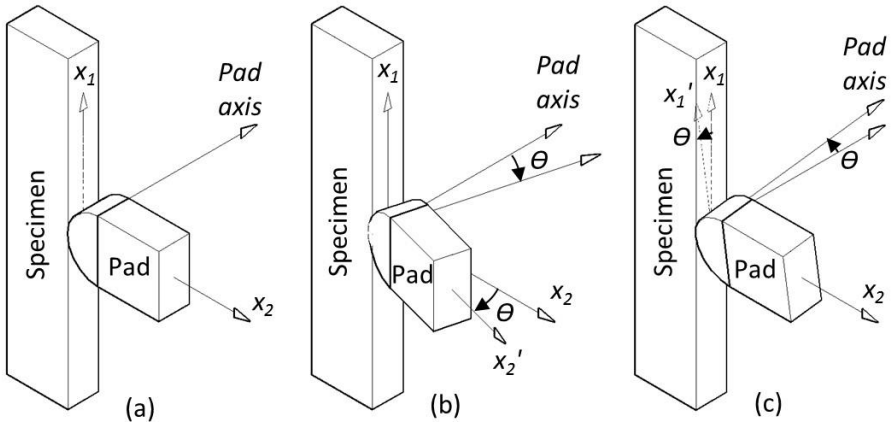

Figure 3.6 a) Perfectly aligned specimen and pad. Misalignment by pad rotation ϴ b) around x_1 axis or c) around x_2 axis

2.2 Single actuator fretting fatigue test rig with adjustable compliance

Another evolution in idealised fretting fatigue test rig designs was that the spring stiffness of the cantilever beam could be adjusted. This configuration has been adopted by Bramhall and many other researchers around the world. The Bramhall apparatus is shown both as schematic and as picture in Figure 3.7a and Figure 3.7b, respectively. This system was also used by [Nowell & Hills, 1990] and [Szolwinski & Farris, 1998] (see Figure 3.8). This kind of test rig had the advantages of being inexpensive and avoiding unwanted phase shift between fatigue and tangential forces. The introduction of tangential force due to deformation of the specimen via application of the bulk fatigue load, automatically assured the in-phase evolution of the two forces. However, it required a large fatigue force to realize sufficient deformation of the specimen no matter how stiff the spring was and it could not be used to

study cases where fatigue load was constant (a particular case with zero fatigue load is called plain fretting).

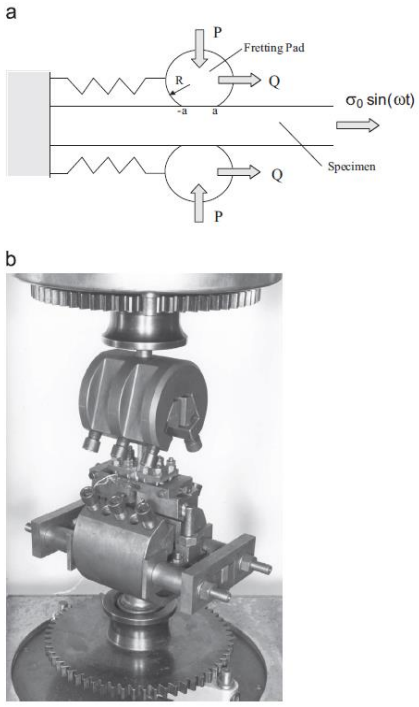

Figure 3.7 Original Bramhall test rig [Hills & Nowell, 2014]

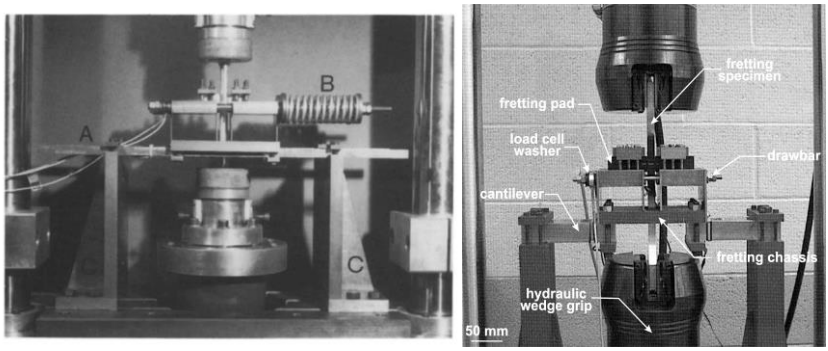

Figure 3.8 Fretting fatigue test rig used by [Nowell & Hills, 1990] (left) and [Szolwinski & Farris, 1998] (right)

2.3 Two collinear actuators fretting fatigue test rig

The single actuator fretting fatigue test rig originated from the concept of the bridge type tests when it was difficult to find a method to control the tangential displacement by an external actuator. With a better control system available, it gave birth to a two collinear actuators fretting fatigue test rig which was first put into practice by [Fellows, Nowell & Hills, 1997]. The

main reason behind the development was the attempt to clearly separate crack initiation and crack propagation lifetimes. Instead of using compliant springs to induce the desired tangential force, it was controlled by an independent hydraulic actuator. The test rig had more advantages compared to the single actuator since it allowed independent control of the fatigue and the tangential forces. Different waveforms, frequencies, phase shifts and amplitudes could be simulated to reproduce as close as possible industrial cases of real fretting problems. However, a very well controlled system needed to be carefully implemented to be able to control these two actuators. Until this moment, to assure a perfect in-phase behaviour of fatigue and tangential forces (which is automatically obtained in the single actuator test rig) remains challenging.

At the time when a well-controlled experimental set-up could be devised and the stress state and slip at the contact could be well characterised, another challenge popped up, i.e. the size effect in fretting fatigue. Below a critical contact area, fretting fatigue lifetime was shifted from a few hundred thousand cycles to infinite even though the magnitude of stress levels were kept constant. This phenomenon has been observed in several materials like aluminium alloy, titanium alloy and high strength steel. It led to severe doubt whether the results of a coupon scale test could be used to interpret real fretting problems in which the contact type was completely different. [Mugadu, Hills & Nowell, 2002] proposed that each real contact problem requires its own coupon scale test with an identical contact type and area. The test set-up and one of the simulated contact types are shown in Figure 3.9. Remember that most of the real fretting contacts such as bolted joints or dovetail connections experience complete contact. Therefore, they modified the two actuator fretting fatigue test rig developed by Fellows (originally for cylinder to plane contact) to allow various contact types representative of real problems. The change of contact type seemed to be easy and straightforward, but when having constraints of maintaining well-defined tractions within the contact it required a reliable and robust design. For complete contact, minor misalignment in any direction would cause a significant change to the contact distribution. Applying a shear force may lead to a rocking moment which alters the well-defined tractions. A detailed design to tackle these issues can be found in [Mugadu, Hills & Nowell, 2002].

Inspired by the above designs, [Meriaux et al., 2010b] also developed their own two collinear actuators fretting fatigue test rig. In addition to the previously discussed fretting fatigue test rigs which typically only record the loads, they equipped their test rig with a potential drop and acoustic emission systems to monitor fretting fatigue crack initiation and propagation. They even considered this set-up as a break through. With the potential drop technique, a micro-crack length around $50\ \mu m$ could be detected and crack growth rate could also be measured. On the other hand, the acoustic emission technique allowed to quantify different modes of micro-crack

propagation for a specific waveform of the fatigue load and the tangential forces [Meriaux et al., 2010a].

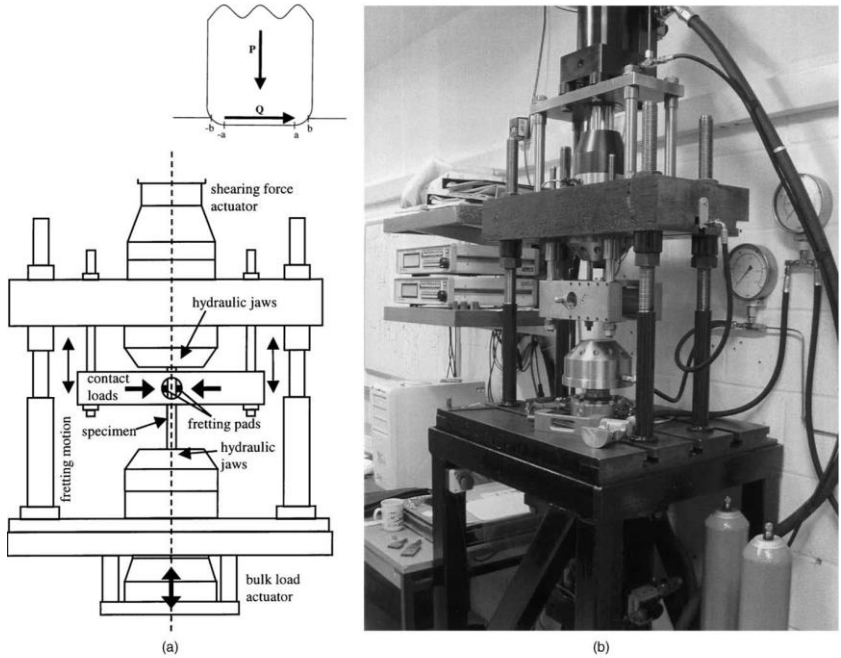

Figure 3.9 Two collinear actuators fretting fatigue test rig [Mugadu, Hills & Nowell, 2002]

2.4 Three actuator fretting fatigue test rig

Another more advanced type of fretting fatigue test rig has recently been devised. The test rig employs three independent hydraulic actuators to control the three interacting forces (fatigue load, shear force, and normal load) as a function of arbitrary time under fretting fatigue [Hills & Nowell, 2014]. According to the authors this allows to study problems where, for example, an out-of-balance rotating mass which modifies both shear and normal fretting loads.

3 UGent fretting fatigue test rig

A fretting fixture had been designed and manufactured to be installed on an ESH 100 kN servo hydraulic load frame so that fretting fatigue tests could be performed [De Pauw, De Baets & De Waele, 2013]. Its schematic drawing is shown in Figure 3.10 (more detailed drawings can be found in Appendix A). The 100 kN hydraulic cylinder of the load frame is used to apply axial dynamic loads on a dog-bone specimen. A constant normal load, P, is applied to the specimen by a separate horizontal hydraulic cylinder via the

fretting pads mounted on their holders, the flexural beams. The C-beam mounted on ertalon blocks can float freely on the base plate to ensure that the normal load is applied equally in the opposite direction. The tangential force, Q, between the dog-bone specimen and the pads is generated by the compliant springs due to the elastic deformation of the specimen. The stiffness of the compliant springs can be adjusted by changing their thickness. This test rig is classified as a single actuator with adjustable compliant springs since the horizontal actuator is not synchronized with the actuator of the fatigue load and the horizontal actuator is not used to control the tangential force as discussed in the previous section. The interaction of these forces on the specimen is shown in Figure 3.11.

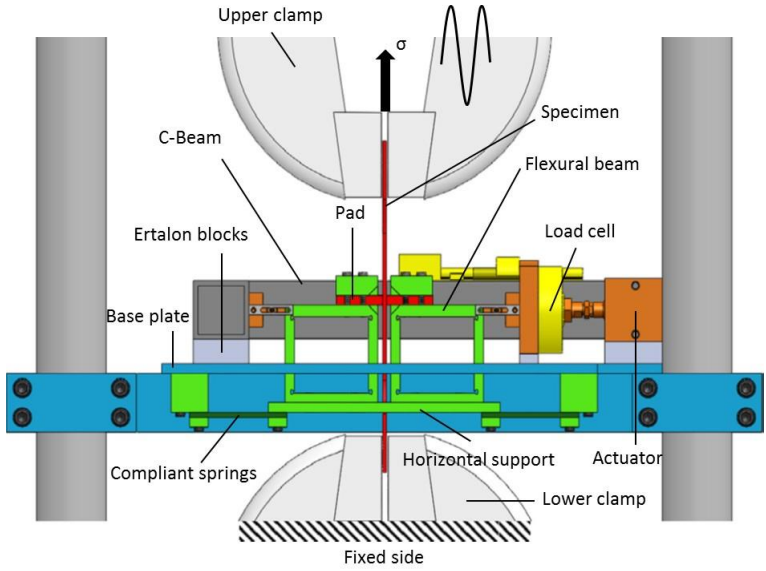

Figure 3.10 Schematic drawing of the fretting fatigue test rig [Hojjati-talemi et al., 2014]

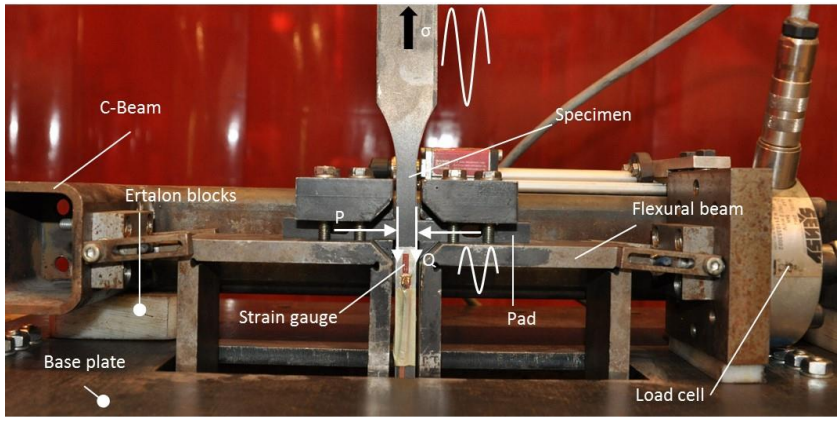

Figure 3.11 Picture of the experimental set-up

The load cell mounted on the C-beam is used to measure directly the contact normal load whereas the tangential force is measured by a calibrated strain gauge attached to the compliant spring at the right-hand side of the rig. The procedure to calibrate this strain gauge will be discussed in section 3.2.

3.1 Challenges of the current test rig

With the available test set-up, two issues remained notwithstanding the huge effort spent in the design process. One is the accurate application of the normal force to the specimen via the pads and the other is the contact alignment for cylindrical pads on a plane specimen. Solutions for these two issues showed to be contradictory.

3.1.1 Application of normal load

The flexural beams, holders of fretting pads, are designed to be fixed to the horizontal support by bolts and nuts as illustrated in Figure 3.12. The horizontal hydraulic actuator controls two opposite normal forces acting on the flexural beams and transferred to the specimen via the pads. Due to the rigidity of this system, part of the controlled force can be absorbed in the bolted connections and not be transferred to the specimen. The problem can be solved by loosening the bolts before applying the load but this may disturb the already well-aligned contact that will be discussed in the next section. This is, at first sight, a minor issue but can have a major effect on the sliding regime at the fretting contact. The ambition to simulate a partial slip regime may not be reached and in the worst case the sliding regime becomes gross slip because the exact normal load is lower than the designed value. As such, instead of performing a test to simulate fretting fatigue, fretting wear occurs.

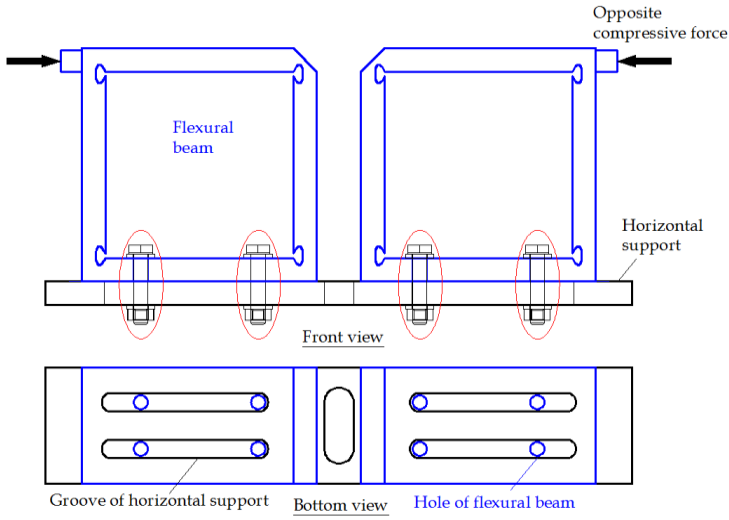

Figure 3.12 Issue with normal load application

3.1.2 Contact alignment

Contact alignment of cylindrical pads on a plane specimen is critical to achieve a contact that is as close as possible to a line contact so that the well-defined tractions of this contact configuration are not violated. In practice, it is quite challenging to realize this, even with very careful mounting. To that end a pressure sensitive film is used to visualize if the alignment is good. The pressure sensitive film is put in between the specimen and the pads, and then a force is applied to see if the pressure is uniformly distributed. If not, re-mounting of at least the pads is required. Figure 3.13 illustrates failed specimens due to fretting damage where cracks originate from different contact alignments. The left figure is considered to be good; the right one clearly lacks a full line contact. If misalignment takes place, the experimental results cannot be used to validate any analytical or numerical model.

This technique can facilitate the alignment but the normal force needs to be unloaded to check the pressure distribution on the film. Re-application of the normal force does not guarantee the well aligned contact because of the design of the current holder (flexural beam) of the pads. Whilst (re-)applying the normal load, the flexural beam can rotate around the vertical axis (x_1) and introduce misalignment, Figure 3.6. Of course, the flexural beams can be tightened to the horizontal support with bolt-nut connections (see Figure 3.12) to avoid rotation, but this leads to some incorrect normal force application as discussed in section 3.1.1.

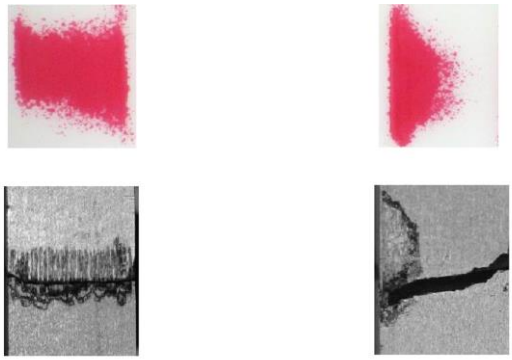

Figure 3.13 Loss of well-defined tractions due to contact misalignment
[Hojjati-talemi et al., 2014]

3.1.3 Optimization of the test rig

As mentioned in the previous section, solutions to the two current issues of the test rig are contradictory. An alternative to solve both issues is to modify the connection between the flexural beams and the horizontal support. The original connection is a plain bolt-nut type which is then modified by adding a housing, sketched in Figure 3.14. The hexagonal segment is mounted in the groove of the horizontal support while the cylindrical segment is mounted in

the hole of the flexural beam. These grooves and holes are sketched in Figure 3.12. Therefore, during the application of the normal load, P, all bolts and nuts can be loosened to avoid any normal force absorption. Whilst the bolt-nut connection is being loosened, the flexural beam can only move freely in the horizontal direction without any rotations that would disturb the well-aligned specimen and pad.

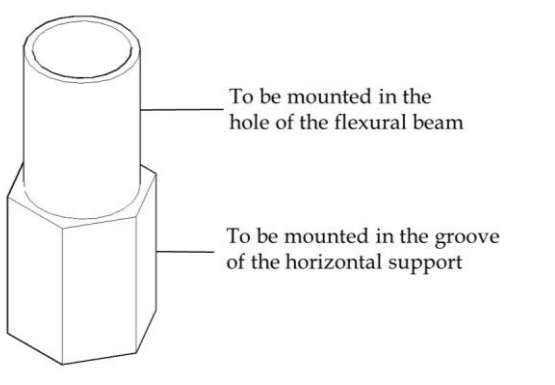

Figure 3.14 Housing for bolt-nut connection between the flexural beam and the horizontal support

3.2 Calibration of the spring

The schematic drawing of the test performed to calibrate the spring is illustrated in Figure 3.15. The specimen and pads are manufactured from identical materials; two material types are used in this study. One is an aluminium alloy (Al2024-T3) and the other one is a cold drawn structural steel (S235JRC).

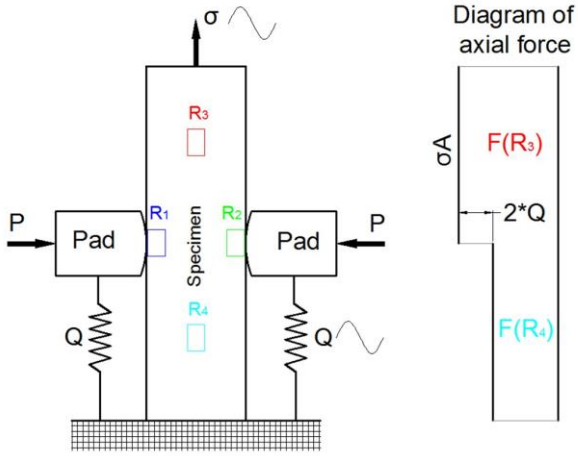

Figure 3.15 Schematic of test setup and diagram of axial force for single actuator fretting fatigue test

Their main mechanical properties are summarized in Table 3.1 Strength properties of Al2024-T3 and S235JRC and the specimen dimensions are shown in Figure 3.16. The specimen contact surface is a plane, while the pad contact surface is cylindrical. The radius, R_{pad}, of the aluminium and the steel cylindrical pads are *50* mm and *150* mm, respectively.

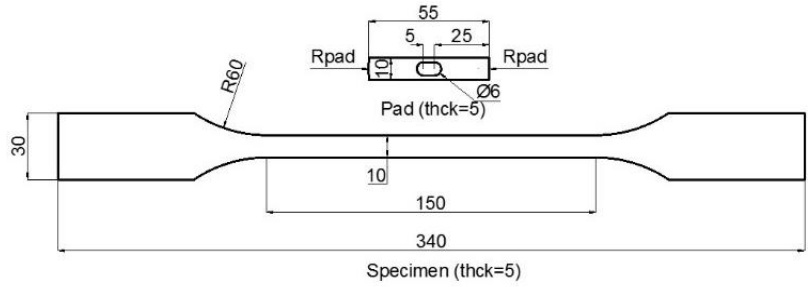

Figure 3.16 Dimensions of the specimen and the pad

Table 3.1 Strength properties of Al2024-T3 and S235JRC

Materials	Young's Modulus E [GPa]	σ_y [MPa]	σ_{ult} [MPa]
Al2024-T3	73	383	506
S235JRC	210	650	700

From Figure 3.15, the tangential force, Q, generated by the compliant springs can be computed by the difference between the forces above and below the contact areas divided by *2* as shown in equation (3-1). $F(R_3)$ is directly measured by the load cell of the ESH 100 kN, F_σ, and $F(R_4)$ is measured by a calibrated strain gauge on the specimen surface below the contact zones (see Figure 3.11). This strain gauge is calibrated by means of simple tensile tests without fretting load. The calibrated relation is given in equation (3-2).

$$Q = \frac{F(R_3) - F(R_4)}{2} = \frac{F_\sigma - F(R_4)}{2} \quad \textbf{(3-1)}$$

$$\frac{F(R_4)}{V(R_4)} = 2.332\ kN/V \quad \textbf{(3-2)}$$

The tangential force, Q, can also be measured based on the deflection of the compliant springs via another calibrated strain gauge attached to one of the springs. This methodology is preferred since it is not necessary to waste a strain gauge on all tested specimens. Evidently, it requires a more complex calibration of the strain gauge attached to the spring, i.e. how much tangential force is equivalent to *1 V* measured from that strain gauge when

spring deflection takes place. Hereto the following methodology is applied in quasi-static conditions. Five load levels are applied to take experimental errors into account. Two strain gauges are needed; one on the specimen surface below the contact areas and the other one on the compliant spring at the right hand side. Before applying the quasi-static loads, an estimated partial slip condition (F_{σ_max} = *9 kN*, σ_{max} = *180 MPa*, *R = 0.1*, *P = 1 kN*) for Al2024-T3 is cyclically applied for 10^3 *cycles* since it has been shown that after 10^3 *cycles*, the partial slip regime was stabilized [Hills & Nowell, 1994]. This stabilized partial slip regime will ensure that no macroscopic slipping between the pads and the specimen occurs during application of the quasi-static loads. Therefore, no loss of forces due to friction is present. Representative correlations between the applied axial force and the voltages measured from the two strain gauges are shown to be linear in Figure 3.17. Their slopes for the five fatigue load levels are summarized and averaged in Table 3.2 and Table 3.3.

Table 3.2 Ratios of measured voltage to applied load range for the strain gauge on the compliant spring[1]

Axial load ranges ΔF_σ [kN]	V_{spring}/F_σ [V/kN]	$(V_{spring}/F_\sigma)_{mean}$ [V/kN]
0-2	-0.0512	
0-4	-0.0525	
0-6	-0.0536	-0.053
0-8	-0.0547	
0-9	-0.0552	

Table 3.3 Ratios of measured voltage to applied load range for the strain gauge on the specimen

Axial load ranges ΔF_σ [kN]	$V(R_4)/F_\sigma$ [V/kN]	$(V(R_4)/F_\sigma)_{mean}$ [V/kN]
0-2	0.333	
0-4	0.339	
0-6	0.343	0.342
0-8	0.347	
0-9	0.349	

1 The minus sign (-) indicates that the tangential force, *Q*, is downward

Once all relations are obtained, the second step is to determine how much axial force, F_σ, needs to be applied to get a spring deflection which corresponds to $V_{spring} = 1\ V$. Taking the inverse of the mean value reported Table 3.2 gives $F_\sigma = 18.712\ kN$.

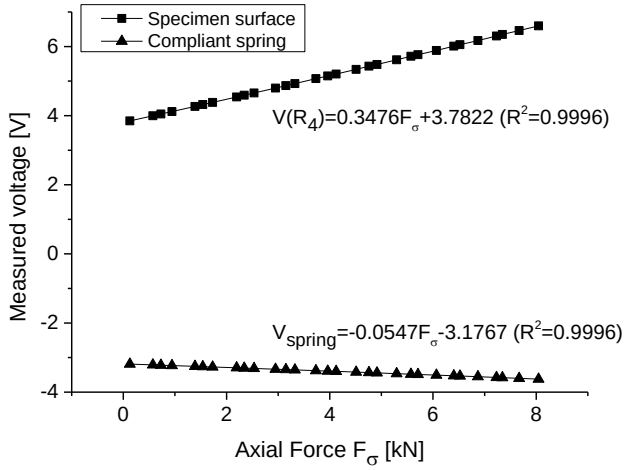

Figure 3.17 Linear relation between applied axial force and the voltages from strain gauges attached to the specimen and to the leaf spring

The next step is to determine how much tangential force is generated when an axial force F_σ equal to $18.712\ kN$ is applied. Based on the equation (3-1), $Q=(18.712-F(R_4))/2$, and thus $F(R_4)$ needs to be determined. From equation (3-2), the voltage measured with the strain gauge on the specimen surface below the contact areas, $V(R_4)$, allows to find $F(R_4)$, i.e. $F(R_4) = 2.332 V(R_4)$. On the other hand, Table 3.3 gives $V(R_4) = 6.403\ V$ as shown in equation (3-3) when an axial force $F_\sigma = 18.712\ kN$ is applied. Then the force in the specimen below the contact areas is obtained as $F(R_4) = 14.933\ kN$, equation (3-4). Finally, $Q = 1.889\ kN$ (equation (3-5)) corresponds to $F_\sigma = 18.712\ kN$ or $V_{spring} = 1\ V$. That also means ***1.889 kN/V*** is the calibrated value of this strain gauge.

$$V(R_4) = 0.342 \times F_\sigma = 0.342 \times 18.712 = 6.403\ V \quad \textbf{(3-3)}$$

$$F(R_4) = 6.403 \times 2.332 = 14.933 kN \quad \textbf{(3-4)}$$

$$Q = \frac{F_\sigma - F(R_4)}{2} = \frac{18.712 - 14.933}{2} = \frac{3.779}{2} = 1.889 kN \quad \textbf{(3-5)}$$

The same methodology has been applied to a test on specimens made of structural steel S235JRC. It was found that ***1 V*** measured with the strain gauge on the compliant spring is equivalent to ***Q = 1.893 kN***. The difference between the two materials is limited to $0.18\ \%$, which confirms that the calibrated value of the strain gauge on the compliant spring is independent

of the tested materials. Obviously, it will depend on the gauge length of the specimen and the position of the fretting pads with respect to the specimen length. During the tests these parameters need to be kept identical to those of the calibrated samples.

3.3 Instrumentation for damage monitoring

With the current UGent fretting fatigue set-up optimized, an infrared camera is also installed to monitor the evolution of fretting fatigue damage and especially to detect the moment of crack initiation on-line. It is a camera based system with an array of cooled infrared detectors of indium-antimonide (InSb). The measurement is within a medium wavelength *2-5 μm* of infrared radiation from the samples. More detailed information to be discussed in the next chapter.

4 Summary and conclusions

Different categories of fretting fatigue tests, each serving a different purpose, have been introduced. The first category, called "*Simulation of a real engineering fretting problem*", can give direct insight into fretting fatigue behaviour of real engineering problems. The second category, called "*Material ranking tests*", allows to rapidly compare fretting fatigue strength of different materials and surface treatment. The third category, called "I*dealised fretting fatigue tests*", ameliorates the understanding of mechanics of fretting fatigue. With an intermediate modelling, fretting fatigue behaviour of real engineering problems can be estimated. This last category has been discussed in more detail in this chapter. All test set-ups are typically equipped with sensors to measure only the interacting forces except [Meriaux et al., 2010a, 2010b] who implemented instrumentation to monitor damage evolution. Contact configuration of cylindrical pads on plane specimen is the most popular in research because of available closed form analytical solutions for contact force distribution, contact shape and dimension, stress and strain field, sticking and slipping size, etc in fretting fatigue. However, whether results of this kind of test can be extended to other contact types or real contact problems remains doubtful due to the size effect phenomenon.

More advanced test rigs in terms of number of actuators to control the interacting forces under fretting fatigue have been devised. They have also become more user friendly for contact alignment and allow various contact types. The latter advantage is important in case the size effect is really the obstacle of correlation of laboratory tests to real fretting problems. In any case, these modern test rigs will be a potential to simulate as close as possible real loading conditions: differences of frequency, wave form, amplitude and phase shift in the real contact problems.

Referring to Chapter 2.2, the size effect for cylinder-plane contact has been claimed to be tackled solely by a stress-based approach. Therefore, in this

thesis, fretting fatigue experiments with this contact type will be performed. Two different materials, an aluminium alloy and a structural steel will be used. An infrared camera will also be installed to detect their crack initiation lifetime, so the model can be further validated. Another contact type, two perpendicular cylinders, will also be tested. These experimental activities are expected to the future tool to confirm whether the stress-based approach is reliable enough to understand fretting fatigue behaviour of materials or components, with the size effect as a major challenge.

References

De Pauw, J., De Baets, P., De Waele, W. (2013) Design of a Fretting Fatigue Test Rig. *Journal of Sustainable Construction and Design*, 4, 6 Pages.

Fellows, L.J., Nowell, D., Hills, D.A. (1997) On the Initiation of Fretting Fatigue Cracks. *Wear*, 205, 120–9.

Hills, D.A., Nowell, D. (1994) *Mechanics of Fretting Fatigue*. Kluiwer Academic Publishers, Dordrecht.

Hills, D.A., Nowell, D. (2014) Mechanics of Fretting fatigue—Oxford's Contribution. *Tribology International*, 76, 1–5.

Hojjati-talemi, R., Wahab, M.A., De Pauw, J., De Baets, P. (2014) Prediction of Fretting Fatigue Crack Initiation and Propagation Lifetime for Cylindrical Contact Configuration. *Tribology International*, 76, 73–91.

Kuno, M., Waterhouse, R. B., Nowell, D., and Hills, D.A. (1989) Initiation and Growth of Fretting Fatigue Cracks in the Partial Slip Regime. *Fatigue & Fracture of Engineering Materials & Structures*, 12, 387–98.

Meriaux, J., Boinet, M., Fouvry, S., Lenain, J.C. (2010a) Identification of Fretting Fatigue Crack Propagation Mechanisms Using Acoustic Emission. *Tribology International*, 43, 2166–74.

Meriaux, J., Fouvry, S., Kubiak, K.J., Deyber, S. (2010b) Characterization of Crack Nucleation in TA6V under Fretting–fatigue Loading Using the Potential Drop Technique. *International Journal of Fatigue*, 32, 1658–68.

Mugadu, A., Hills, D.A., Nowell, D. (2002) Modifications to a Fretting-Fatigue Testing Apparatus Based upon an Analysis of Contact Stresses at Complete and Nearly Complete Contacts. *Wear*, 252, 475–83.

Navarro, C., Munoz, S., Dominguez, J. (2008) On the Use of Multiaxial Fatigue Criteria for Fretting Fatigue Life Assessment. *International Journal of Fatigue*, 30, 32–44.

Nishioka, K., Hirakawa, K. (1969) Fundamental Investigations of Fretting Fatigue. *Bulletin of JSME*, 12, 692–7.

Nowell, D., Dini, D., Hills, D.A. (2006) Recent Developments in the Understanding of Fretting Fatigue. *Engineering Fracture Mechanics*, 73, 207–22.

Nowell, D., Hills, D. a. (1990) Crack Initiation Criteria in Fretting Fatigue. *Wear*, 136, 329–43.

Ruiz, C., Boddington, P.H.B., Chen, K.C. (1984) An Investigation of Fatigue and Fretting in a Dovetail Joint. *Experimental Mechanics*, 24, 208–17.

Szolwinski, M.P., Farris, T.N. (1998) Observation, Analysis and Prediction of Fretting Fatigue in 2024-T351 Aluminum Alloy. *Wear*, 221, 24–36.

Chapter 4 Infrared thermography instrumentation

"In this chapter, the concepts of lock-in thermography signal processing are discussed. Conventionally, damage detection in fretting fatigue tests has been performed using off-line methodologies. The feasibility of coupling temperature acquisition using an infrared thermographic camera and on-line signal processing, for on-line monitoring of damage under cyclic loading will be demonstrated."

1 Introduction

Thermography is conventionally defined as a technique to measure temperature. The most straightforward technique is to attach thermal sensors, for example thermocouples or resistive thermometers, to a surface where temperature is desired to be measured. These techniques can give a very high spatial resolution (up to a few microns) based on the sensor tip dimensions and a temperature resolution around *100* mK. This contact thermography is however based on spatially discrete measurements and necessitates a serial measuring methodology since a large array of contact sensors is impracticable.

Besides the contact thermography, several contactless thermographic techniques exist. One popular approach is the photothermal or thermo-reflectance principle. It is based on the fact that the optical reflection of a reflecting surface is usually temperature-dependent. As a result the intensity of the reflected light can be related to temperature. Three other contactless thermographic techniques can be used; one is based on visible light microscopy and two are based on near infrared microscopy. The techniques are based on thermal mapping using nematic or thermochromic liquid crystals, fluorescent microthermal imaging, etc [Breitenstein, O., Warta, W., Langenkamp, 2010]. Basically, samples covered with liquid crystals show different colours in relation to the temperature when they are illuminated by white light, so temperature mapping can be done. Fluorescent microthermal imaging is based on strong temperature dependence of certain organic dyes. Samples applied with this thin layered dye reveal temperature differences if they are illuminated by UV light and observed by a fluorescent microscope or a sensitive CCD camera. The last type of contactless thermographic technique using a camera is based on infrared irradiation. This is considered to be the most elegant technique since it gives a high spatial and temperature resolution, and the infrared radiation is transparent to some solid materials like sapphire and silicon. This technique does not require any liquids or organic dyes to be applied to the object surface.

Infrared light is an electromagnetic wave with a wavelength between *0.7 μm* and *1 000 μm*, and is further categorized as short range (near visible light), medium range and long range as illustrated on Figure 4.1. Within the medium range and long range wavelengths, there are two windows where the atmosphere (water vapour and CO_2) is transparent to infrared light, Figure 4.1. An infrared camera is built to detect infrared radiation within these wavelengths so that contactless measurements in atmosphere are feasible. A material's sensitivity to the infrared radiation depends on the applied wavelength. For example, indium-antimonide (InSb) is only sensitive in mid-range (*3-5 μm*) while mercury-cadmium-telluride (HgCDTe) is only sensitive in long range (*8-14 μm*). There are two methods to construct an infrared image based on these detectors. One is called a serial-based system

and the other one is a camera-based system. A serial-based measuring technique relies on a single infrared detector that scans a surface to map the temperature distribution. On the other hand, a camera-based system uses a focal plane array like a digital optical camera to measure the surface temperature distribution. Both methods can provide a high sensitivity in the range of *10~20 mKs* but the latter allows a higher frame rate (up to *kHz* range).

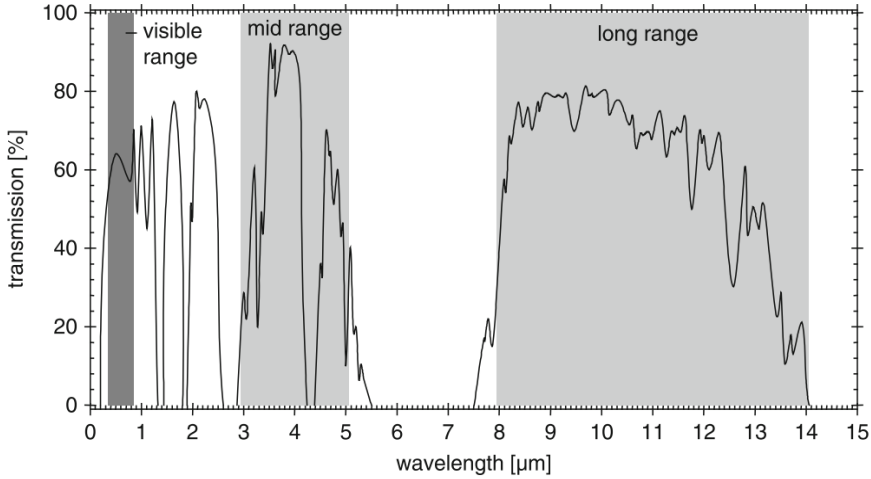

Figure 4.1 Transmission of the atmosphere in the wavelength range between 0.2-14 µm (distance 1250 m at 20 ^{0}C and 100% relative humidity) [Miller, 2001]

Conventionally, a steady-state surface temperature is measured, which is called classical or passive thermography. However, temperature can be actively influenced by external sources. Such measurements are called active thermography which includes lock-in and pulse thermography. The lock-in thermography normally uses excitation according to a periodic wave form (eg. cyclic mechanical loads), whilst pulse thermography is based on an instantaneous excitation (eg. by means of a flash lamp oriented towards the specimen). Therefore the lock-in technique normally takes more time than the pulse thermography for any measurement. For active thermography, amplitude and phase of cyclic parameters are used for analysis and evaluation. This technique [Berthel et al., 2014; Krapez, Pacou & Gardette, 2000; Ummenhofer & Medgenberg, 2009] has become more and more popular as it can give more reliable information than passive thermography [Fargione et al., 2002; Luong, 1998; Micone & De Waele, 2016; Risitano & Risitano, 2010; Rosa & Risitano, 2000]. Though the target object is stationary, an external heat source is used to excite the object, called temperature modulation and a camera is used to analyse temperature responses of the reflected signal. This practice is common in non-destructive evaluation of materials. Sometimes, an external vibration at ultra-high frequency is used,

called infrasonic, to force material defects to respond to that motion, yielding an improved temperature signal. Mostly, the temperature responses measured by one of these techniques have been analyzed off-line. Therefore, an attempt to implement the principles of such methods in an on-line methodology will be made in this study.

2 Lock-in signal processing

Basically lock-in signal processing is a technique dealing with an oscillating signal. An excellent review was made by [Krapez, 1998], including four algorithms: standard lock-in method (SLIM), least-squares method (LSM), four bucket point (4BP), and variance method. The first three methods require a reference frequency (called lock-in frequency) so that the exact signal, corresponding to this reference frequency, can be extracted from an input signal containing a variety of noises. The last method is a purely statistical method which does not require any reference frequency. The 4BP technique is just a special case of the SLIM method when the number of samples per cycle is equal to four. Of all these algorithms, the LSM approach has been demonstrated to be the best technique in terms of damage detection; however it cannot be performed on-line. Therefore, only the standard lock-in methodology will be introduced in detail in the following section.

2.1 Standard lock-in method

The lock-in methodology is a filtering technique that is typically applied for cases where signals have to be extracted from statistical noise. The basic requirement to allow the use of this technique is that the target signal can be periodically pulse or amplitude modulated with a certain frequency, called "lock-in frequency", $f_{lock\text{-}in}$. This modulation is sometimes part of the experiment itself, i.e. the lock-in frequency is equal to the loading frequency.

The aim of the lock-in principle is to evaluate only the oscillating or *AC* (alternating current) component of the main signal. Mathematically, this can be done by simple integration of the multiplication of an input signal *F(t)* with a lock-in correlation function *K(t)* over an integration time, t_{int}, according to equation (4-1). If *K(t)* is an anti-symmetric square wave function, it will result in a perfect suppression of the *DC* (direct current) component of the input signal *F(t)*. *DC* and *AC* components of the signal are defined analogously to an electrical current [Breitenstein, O., Warta, W., Langenkamp, 2010].

$$S = \frac{1}{t_{\text{int}}} \int_0^{t_{\text{int}}} F(t)K(t)dt \quad \text{with} \begin{cases} K(t) = +1 \text{ for first half period} \\ K(t) = -1 \text{ for last half period} \end{cases} \qquad \textbf{(4-1)}$$

Digital lock-in processing requires digitizing the input signal *F(t)* into several discrete numbers F_k. The same needs to be done for the correlation function

$K(t)$ to get a set of numbers K_k, called weighting factors. Discrete numbers of the signal are obtained from the real time measurement, whilst the weighting factors are extracted from the correlation function based on the time of the measured signal. Then the entire lock-in correlation procedure can be performed numerically for a set of M numbers as illustrated by equation (4-2). The integration time corresponding to this number M can last for multiple periods of the lock-in correlation function. There are two strategies of performing digital lock-in correlation: on-line (evaluation of the data during the measurement) and off-line (all data are stored and correlated after the measurement). The summation in equation (4-2), defined as standard lock-in correlation, can be done easily during the measurement.

$$S = \frac{1}{M}\sum_{k=1}^{M} F_k K_k \qquad \textbf{(4-2)}$$

In case the above summation spans a number of multiple lock-in periods, N, the weighting elements remain the same for every individual lock-in period, L, if the sampled elements are recorded in a synchronous way with the lock-in frequency. More details about synchronization of the lock-in frequency and the sampling rate will be discussed in the following section. Then it is possible to simplify the digital lock-in correlation, Equation (4-2), to equation (4-3). Equation (4-3) looks more complex than the previous one, but it is easier from a correlation perspective because it is only necessary to determine the weighting elements in the first period of the total integration time. Note that the multiplication of NxL is equal to the parameter M corresponding to the total integration time.

$$S = \frac{1}{N \times L}\sum_{i=1}^{N}\sum_{j=1}^{L} F_{i,j} K_j \qquad \textbf{(4-3)}$$

Up to this point, the correlation function, $K(t)$, was anti-symmetric. This correlation process is called wideband lock-in correlation because it can be used to extract the amplitude of a harmonic signal, $F(t)$, for a variety of frequencies. On the other hand, if the correlation function is harmonic, the methodology is called narrowband correlation since it allows to extract the signal amplitude at the very specific frequency of the correlation function. These two correlation methods have their own merits and should be chosen depending on the applications and purposes. In terms of level of signal-to-noise ratio, it is more advantageous to select the same lock-in correlation function as the signal function [Breitenstein, O., Warta, W., Langenkamp, 2010].

Next, the narrowband correlation process is discussed. Assume a *sine* wave signal having an amplitude A, a phase Φ and an arbitrary frequency f, as shown in equation (4-4). This time, two harmonic correlation functions are selected, one is a *sine* or in-phase function (0^o), equation (4-5), and the other is a *cosine* or quadrature function (90^o out of phase), equation (4-6). Of course,

single correlation can be done as well but the phase independent amplitude is obtained only when the signal, *F(t)*, and the correlation function, *K(t)*, are exactly in phase. This is only achievable if synchronization between the sampling rate and lock-in frequency is possible (see section 2.2).

$$F(t) = A\sin(2\pi ft + \Phi) \quad \textbf{(4-4)}$$

$$K(t)^0 = 2\sin(2\pi f_{lock\text{-}in}t) \quad \textbf{(4-5)}$$

$$K(t)^{90} = 2\cos(2\pi f_{lock\text{-}in}t) \quad \textbf{(4-6)}$$

The *sine* and *cosine* correlations allow to extract the signal amplitude, *A*, without requiring the signal, *F(t)*, and the correlation function, *K(t)*, to be in phase and to investigate the influence of that phase shift, Φ, on the correlation output, *S*. Inserting these two correlation functions and the signal function into equation (4-1), the corresponding correlation outputs, S^0 and S^{90} can be determined from the integration, equations (4-7) and (4-8), respectively.

$$S^0 = \frac{1}{t_{\text{int}}}\int_0^{t_{\text{int}}} F(t)K(t)^{0^o}\,dt = \frac{1}{t_{\text{int}}}\int_0^{t_{\text{int}}} A\sin(2\pi ft + \Phi)*2\sin(2\pi f_{lock-in}t)dt \quad \textbf{(4-7)}$$

$$S^{90} = \frac{1}{t_{\text{int}}}\int_0^{t_{\text{int}}} F(t)K(t)^{90^o}\,dt = \frac{1}{t_{\text{int}}}\int_0^{t_{\text{int}}} A\sin(2\pi ft + \Phi)*2\cos(2\pi f_{lock-in}t)dt \quad \textbf{(4-8)}$$

For a long enough integration time spanning multiple lock-in periods, t_{int} >> one lock-in period, it is shown in Appendix B that these integrations result in simple *cosine* and *sine* outputs as a function of the signal amplitude *A* and the phase shift *Φ* as shown in equations (4-9) and (4-10). It should be noted that any disturbing harmonic functions having frequencies different from the lock-in frequency, $f_{lock\text{-}in}$, and any *DC* components of the signal can be perfectly suppressed by this correlation process.

$$S^0 = A\cos(\Phi) \quad \textbf{(4-9)}$$

$$S^{90} = A\sin(\Phi) \quad \textbf{(4-10)}$$

Combining equations (4-9) and (4-10), the independent phase amplitude *A* can be calculated from equation (4-11), while the phase difference of the signal to the correlation function can be calculated from equation (4-12). Indeed, the in phase and 90° out of phase correlation outputs, S^0 and S^{90}, can be determined from a digital lock-in correlation process, similarly to equation

(4-2) or (4-3), replacing the anti-symmetric weighting factors K_j by the *sine* and *cosine* weighting factors S^0_j and S^{90}_j.

$$A = \sqrt{\left(S^0\right)^2 + \left(S^{90}\right)^2} \tag{4-11}$$

$$\Phi = \arctan\left(\frac{S^{90}}{S^0}\right) \tag{4-12}$$

This standard lock-in strategy is actually a discrete Fourier transform of the signal at a specific frequency, the lock-in frequency. This type of correlation gives oscillating parameters at that single frequency, typically the basic harmonic. Higher harmonics can be studied, but this requires multiple correlation processes. Instead of the *sine* and *cosine* correlations, other lock-in algorithms such as a Fast Fourier Transform (FFT) and least-squares method should be performed if higher harmonics are of interest. The only rule to be respected for performing the FFT is that the set of numbers M needs to be 2^i where i is an integer.

2.2 Timing strategy

In this section, a different timing strategy, i.e. timing correlation between the sampling rate of the signal and the lock-in frequency, is given. So far, synchronous and oversampling rate, Figure 4.2a, have been used to explain the basic principle of lock-in correlation. Such timing strategies are not the only way to perform the lock-in correlation. Before explaining other timing strategies, a sampling theory proposed by Nyquist and Shannon is reviewed. In order to reproduce a *sine* or *cosine* signal, at least 2 samples per cycle are required. Hence, for a *sine* or *cosine* signal at the lock-in frequency, its sampling rate should be at least two times the lock-in frequency, $f_s > 2f_{lock\text{-}in}$ or $f_{lock\text{-}in} < f_s/2$ [Orfanidis, 2010]. This criterion is normally defined as the Nyquist frequency $f_{Nyq} = f_s/2$ which borders undersampling and oversampling. Remember well that the more samples are taken per period, the more equivalent the digital correlation process, equation (4-1), will be to the integration, equation (4-2).

In Figure 4.2, the abscissa and ordinate are the time and values of *sine* weighting factors respectively (the cosine weighting factors are not shown here). The continuous line corresponds to a signal function whilst the square marks indicate the sampled event and the weighting factors; the vertical dashed line indicates the end of a lock-in duration. From this figure, synchronization is defined when the signal is sampled equidistantly along the time axis so that from one lock-in period to another one, the weighting factors remain alike, Figure 4.2a. Asynchronous sampling corresponds to a situation where the individual samples are not equidistant along the time axis or where the signal is sampled randomly in the time domain so that the

weighting factors are different from one lock-in period to another one, Figure 4.2b. Cases a and b are considered to be oversampling based on the above sampling theorem since there are 12 samples per period. In Figure 4.2c, the sampling rate of the signal is asynchronous and particularly very low, only 1 sample per signal period, which can be called undersampling. This results in an aliasing phenomenon, i.e. the reproduced waveform (indicated by the dashed sine wave) does not represent the original signal. However, this case still allows to determine the signal amplitude correctly. If the frequency of the signal is known in advance, this undersampling technique is very useful not needing many samples which sometimes causes storage issues in case of off-line processing. Figure 4.2d is a dangerous case of undersampling with two samples per period. Reproduction of these sampled events results in a straight line instead of an oscillating signal. Finally, it is also possible to select the undersampling technique with synchronization, as can be seen in Figure 4.2e.

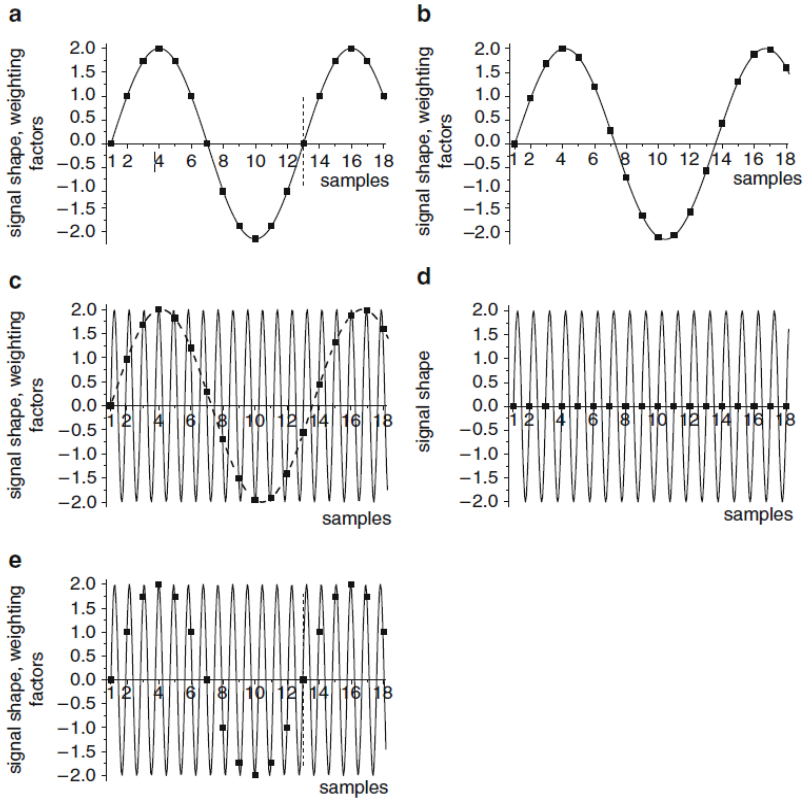

Figure 4.2 Timing diagrams of (a) conventional synchronous correlation, (b) conventional asynchronous correlation, (c) asynchronous undersampling, (d) undersampling at a forbidden frequency, (e) synchronous undersampling [Breitenstein, O., Warta, W., Langenkamp, 2010]

Synchronization is very helpful and will accelerate the lock-in correlation process but it is not always possible to do so, especially when the lock-in frequency is controlled by a testing machine that is independent from the camera. Therefore, most of the time asynchronization is faced requiring a search for the corresponding weighting factors when a signal event is sampled for the correlation.

3 Lock-in thermography

Lock-in thermography is distinguished from standard thermography by the way it displays the temperature at each pixel. In lock-in thermography, the temperature amplitude is used for imaging rather than the absolute temperature. It is typically based on the lock-in signal processing discussed in the previous section. Each thermal image depends on the phase difference between the signal and the correlation function. As an example, Figure 4.3 illustrates the in-phase and quadrature thermal images of a solar cell. The heat source on that solar cell is powered for only half a period. An infrared camera with signal processing based on the lock-in methodology is used to observe temperature reaction of this heat source. In this example, a heat source on the solar cell can be more clearly visualized (especially for the in-phase image) by lock-in thermography compared to the standard thermal image where noise is unavoidable. In other literatures, the lock-in thermography is also adopted for detecting defects in a non-destructive approach [Junyan, Yang & Jingmin, 2010] and for improving image resolution in thermoelastic stress analysis [Kim et al., 2014].

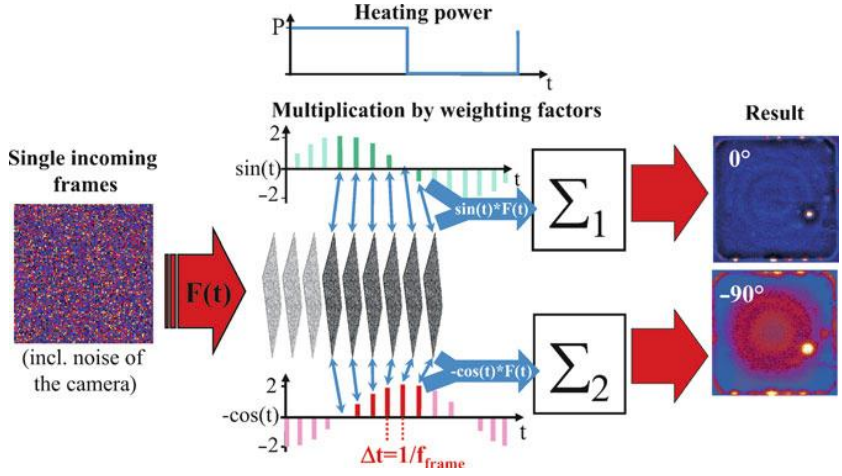

Figure 4.3 Lock-in imaging process [Breitenstein, O., Warta, W., Langenkamp, 2010]

4 ImageIR8300 camera

4.1 Commercial software IRBIS3

The ImageIR8300 of InfraTEC is a camera-based system with full frame resolution of *640* by *512 pixels* and temperoal resolution of *25 mK* at *30°C*. The infrared detector is InSb cooled by Stirling cooler, and its spectral range is in a range of *2-5 μm*. The temperature measurement is ranged within *-5~150 °C*. The maximum frame rate is *300 Hz* if the full frame thermal image is recorded and can be further increased if sub frame image is taken. Equipped with a telephotolens of a *50 mm* focal distance., the minimum working distance of the camera is *500 mm*. An circular ring needs to be mounted with the lens if shorter distance is required to lower the pixel size, and if the field of view of the zone of interest is sufficiently large enough. The current camera is controlled by a commercial software IRBIS3 installed on a computer laptop via an ethernet cable. The software allows to perform a remote focus, adjust the acquisition parameters, record the thermal images, analyze temperature data, and to extract the data for further analysis. But, the triggering of the camera by the software is not possible with the current camera model.

Like other researchers, thermal images obtained from the software are stored and post-processed off-line. The size of full-frame thermal images (see Figure 4.4) is large, a few megapixels, which leads to storage issues if long measurement periods are required. Even though a sub-frame function of software allows to reduce the images size, it is still very difficult to avoid this challenge.

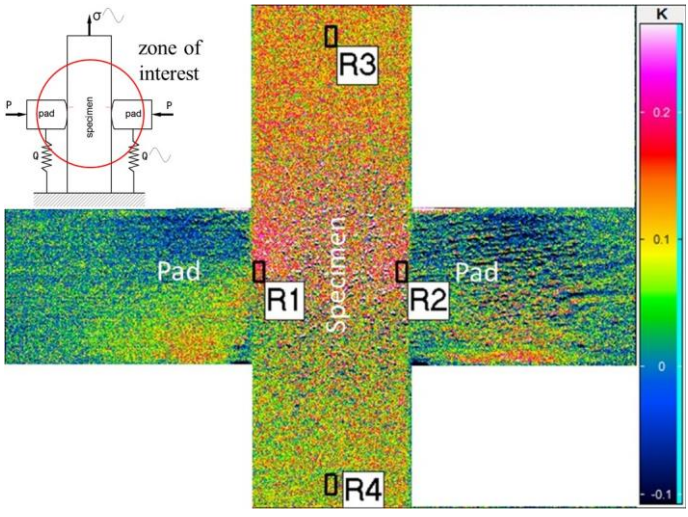

Figure 4.4 A full frame thermal image, *640* by *512* pixels, of a fretting fatigue test captured by the ImageIR8300 camera and visualized with IRBIS3 software

This common practice does not allow continuous measurement during long experiments like fatigue tests. This drawback has so far restricted researchers to a certain practice even though they realized the larger potential of thermography to monitor material damage in cylic loading conditions. For instance:

- Many researchers have been forced to perform fatigue tests of short duration (less than a few hours), with stepwise block loading, to generate some fatigue damage but not a complete failure of the specimen so that thermal images of the entire test could be captured. By analysing the evolution in temperature data they attempted to predict fatigue strength or crack initiation lifetime from these thermal images [Colombo, Vergani & Burman, 2012; Fargione et al., 2002; Krapez, Pacou & Gardette, 2000; Luong, 1998; Micone & De Waele, 2016; Montesano, Fawaz & Bougherara, 2013; Risitano & Risitano, 2010; Rosa & Risitano, 2000] and [Berthel et al., 2014]. Such techniques seem to be very common for (plain) fatigue analysis with infrared thermography. Real time measurement of the crack initiation with thermography has been very rare.
- Some researchers recorded intermittent sequences of images during fatigue tests conducted until final rupture of the specimen. The time gap from one sequence to another one typically spans a large number of cycles [Ummenhofer & Medgenberg, 2009]. Even though this technique has been demonstrated to allow the detection of crack initiation, the continuous temperature response of the entire test could not be captured, which sometimes led to missing important information of the test.
- Some researchers equiped a fatigue testing machine with an ultrasound actuator to significantly increase the load frequency (MHz regime) and to make sure that the center of the specimen, where the fatigue stress is maximum, is stationary during cyclic loading to avoid the requirement of recording images at multiple samples per cycle [Ranc, Wagner & Paris, 2008].

4.2 On-line data acquisition with Matlab

Reviewing the relevant literature, revealed that several thermal theories and models have been developed to assess material damage under cyclic loading. However, in-situ and on-line monitoring of such damage does not yet exist. At Laboratory Soete the infrared camera of InfraTEC, model ImageIR8300 can also be controlled by a Matlab interface, Figure 4.5, in addition to the dedicated commercial software, IRBIS3. In particular, access to temperature data is made possible without the need of recording thermal images with this script. This functionality could indeed solve the storage issues related to a thermography technique. In addition, this script allows to load existing thermal images so that the event corresponding to those images can be

reproduced or simulated. A simulated thermal image visualized using this script is illustrated in Figure 4.5.

The accuracy of this on-line data acquisition can be verified with the conventional off-line technique. Four regions of interest, R_1-R_4, have been selected for this verification as shown in Figure 4.4 and Figure 4.5. Two regions are located near the contact zones whilst the others two are above and below the contact zones. Off-line temperature data of the four regions is extracted with InfraTEC CAM software IRBIS3 from sequences of thermal images recorded with the same software. These images can be reproduced by the Matlab script and the data of the selected regions of interest has also been acquired on-line. As an illustration, the comparison between the on-line and off-line data acquisition for the region R_1 is shown in Figure 4.6. An excellent data matching can be observed.

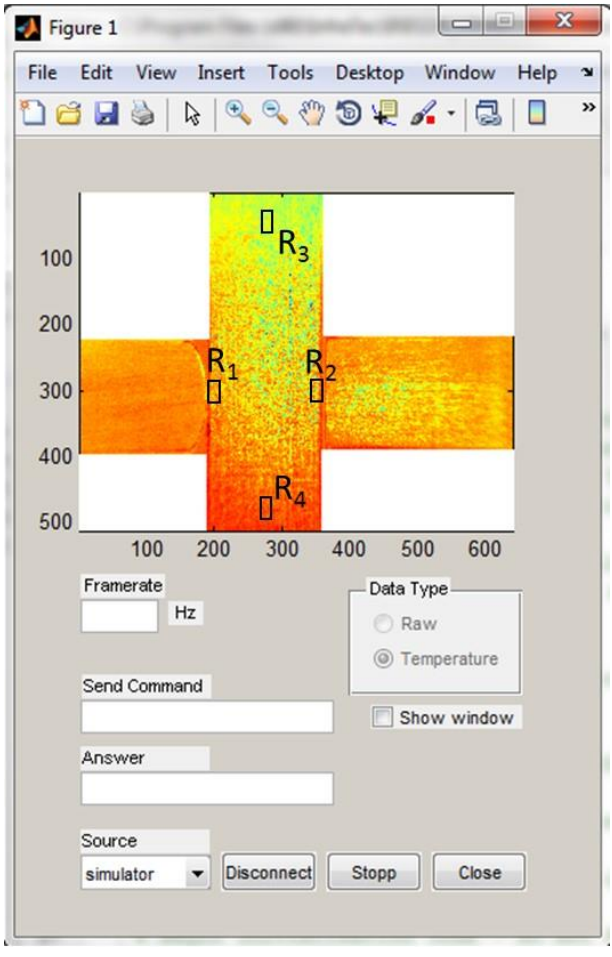

Figure 4.5 A thermal image reproduced and visualized by Matlab

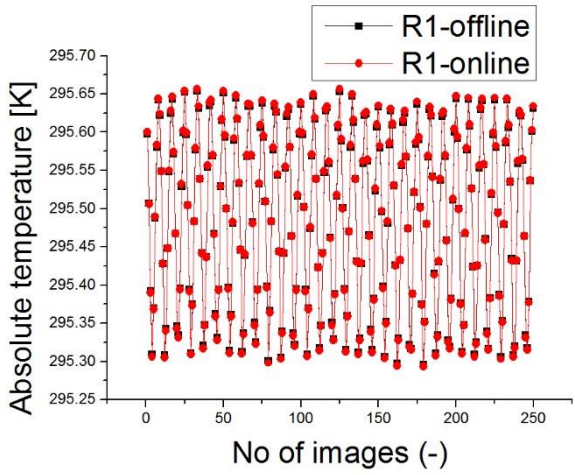

Figure 4.6 On-line vs off-line data acquisition at *ROI* R_1

5 Summary and conclusions

Infrared thermography is considered the most elegant among other thermography techniques due to its high spatial resolution, high frame rate, high sensitivity, and simple experiment preparation (it is e.g. not always necessary to use an external flash light or liquids). The principle of lock-in algorithm is elaborated since it is looks possible for the on-line processing compared to the other algorithms. With this signal processing, active or lock-in thermography can be performed to measure a temperature of objects in dynamic motion or to directly analyse the oscillating temperature modulation. This technique improves the conventional thermography based on a steady state temperature by giving more reliable information based on the amplitude and the phase of the oscillating signal. It could be the reason why the technique has been widely used for damage detection under different cyclic loadings and in non-destructive evaluation. However, those methodologies have been applied mostly off-line and have been limited due to storage issues. The infrared camera used at Laboratory Soete, InfraTEC model ImageIR8300, allows access to on-line data acquisition with a Matlab script. This means that continuous temperature measurements can be performed during the whole experiment even though it requires several days of testing. The lock-in principle, typically adopted for lock-in thermography, can be used to process the temperature data of certain regions of interest without the need of constructing any thermal images.

References

Berthel, B., Moustafa, A.-R., Charkaluk, E., Fouvry, S. (2014) Crack Nucleation Threshold under Fretting Loading by a Thermal Method. *Tribology International*, 76, 35–44.

Breitenstein, O., Warta, W., Langenkamp, M. (2010) *Lock-in Thermography, Basics and Use for Evaluating Electronic Devices and Materials*, Second. Springer Verlag, Heidelberg.

Colombo, C., Vergani, L., Burman, M. (2012) Static and Fatigue Characterisation of New Basalt Fibre Reinforced Composites. *Composite Structures*, 94, 1165–74.

Fargione, G., Geraci, A., Rosa, G. La, Risitano, A., Doria, V.A. (2002) Rapid Determination of the Fatigue Curve by the Thermographic Method. *International Journal of Fatigue*, 24, 11–9.

Junyan, L., Yang, W., Jingmin, D. (2010) Infrared Physics & Technology Research on Thermal Wave Processing of Lock-in Thermography Based on Analyzing Image Sequences for NDT. *Infrared Physics and Technology*, 53, 348–57.

Kim, G., Kim, G., Park, J., Kim, D., Cho, B. (2014) Infrared Physics & Technology Application of Infrared Lock-in Thermography for the Quantitative Evaluation of Bruises on Pears. *INFRARED PHYSICS & TECHNOLOGY*, 63, 133–9.

Krapez, J.. (1998) Compared Performances of Four Algorithms Used for Modulation Thermography. In *Quantitative Infrared Thermography 4*. pp. 148–53.

Krapez, J.C., Pacou, D., Gardette, G. (2000) Lock-in Thermography and Fatigue Limit of Metals. In *Quantitative Infrared Thermography 5*. pp. 277–82.

Luong, M.P. (1998) Fatigue Limit Evaluation of Metals Using an Infrared Thermographic Technique. *Mechanics of Materials*, 28, 155–63.

Micone, N., De Waele, W. (2016) On the Application of Infrared Thermography and Potential Drop for the Accelerated Determination of an S-N Curve. *Experimental Mechanics*, 57, 143–53.

Miller, J.L. (2001) *Principle of Infrared Technology: A Practical Guide to the State of the Art*. John Willey Sons, New York.

Montesano, J., Fawaz, Z., Bougherara, H. (2013) Use of Infrared Thermography to Investigate the Fatigue Behavior of a Carbon Fiber Reinforced Polymer Composite. *Composite Structures*, 97, 76–83.

Orfanidis, S.J. (2010) *Introduction to Signal Processing*. Rutgers University.

Ranc, N., Wagner, D., Paris, P.C. (2008) Study of Thermal Effects Associated with Crack Propagation during Very High Cycle Fatigue Tests. *Acta Materialia*, 56, 4012–21.

Risitano, A., Risitano, G. (2010) Cumulative Damage Evaluation of Steel Using Infrared Thermography. *Theoretical and Applied Fracture Mechanics*, 54, 82–90.

Rosa, G. La, Risitano, A. (2000) Thermographic Methodology for Rapid Determination of the Fatigue Limit of Materials and Mechanical Components. *International Journal of Fatigue*, 22, 65–73.

Ummenhofer, T., Medgenberg, J. (2009) On the Use of Infrared Thermography for the Analysis of Fatigue Damage Processes in Welded Joints. *International Journal of Fatigue*, 31, 130–7.

Chapter 5 Fretting fatigue limit

"In this chapter, the current state of the art on fretting fatigue limit is briefly reviewed, followed by an elaboration of a developed thermographic method for rapid determination of the fretting fatigue limit."

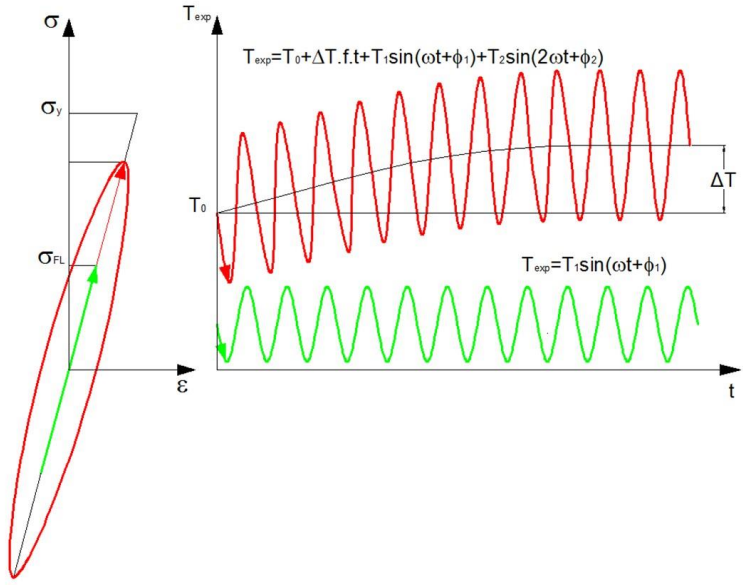

1 Introduction

The fatigue regime is usually categorized in three domains: low cycle fatigue (lifetime: $N_f < 10^4$ *cycles*), high cycle fatigue (10^4 *cycles* $< N_f < 10^7$ *cycles*), and ultra high cycle fatigue ($N_f > 10^7$ *cycles*) [Schijve J, 2009; Wagner et al., 2009]. Low cycle fatigue is characterized by macroscopic plastic deformation, whilst only localized plastic deformation occurs in high cycle fatigue [Schijve J, 2009]. The localized plastic deformation in high cycle fatigue can be due to cyclic slip activity at the free surface of a certain grain, or due to a sharp cross-sectional change, a tip of a notch, a fretting contact, etc. In this sense, fretting fatigue is typically considered to be high cycle fatigue which should show a fatigue limit at 10^7 *cycles* [Kondo et al., 2005] even though failures due to fretting fatigue have sometimes been observed in ultra high cycle fatigue regimes [Hirakawa, Toyama & Kubota, 1998]. So far two approaches to determine the fretting fatigue limit have been reported: analytical approach and experimental approach.

2 Analytical approaches

The fatigue limit is defined as the threshold that determines the stress level below which either a crack is not nucleated or either is nucleated but arrested. Crack nucleation and crack arrest can be analysed based on continuum mechanics and fracture mechanics (applied to micro-cracks), respectively. As discussed in Chapter 2.2, the crack nucleation part is not yet well understood due to the size effect and the lack of experimental evidence of the crack formation process. Therefore, the fretting fatigue limit has been studied based on short-crack arrest. Crack arrest can be divided into two types: microstructural crack arrest where micro-crack growth is stopped due to obstacles like grain boundaries, and mechanical crack arrest where the stress intensity factor at a micro-crack tip drops below the stress intensity factor threshold for micro-crack growth [Schijve J, 2009]. The mechanical crack arrest approach has been exploited in fretting fatigue due to the nature of the stress gradient induced by the fretting contact.

The very well known law for fatigue crack propagation and its growth rate is the Paris law. This law states that a crack will not grow if the stress intensity factor at the crack tip is below a threshold value. This threshold, only valid for macro-cracks, can be experimentally determined according to an ASTM standard [ASTM-E647-08, 2009]. However, [Miller, 1993] showed that below this stress intensity factor threshold, a short crack or micro crack could still grow and could also be arrested because there is a lower threshold value for short crack propagation. He discussed two thresholds for crack propagation, a macro-crack threshold ΔK_0 (same as for the Paris law), and a micro-crack threshold $\Delta K_{th} < \Delta K_0$. The fretting fatigue limit is considered to be that loading condition for which the stress intensity factor is below the threshold

value for a non-propagating micro-crack. The transition between short and long crack dimensions can be estimated by equation (2-9) and the short-crack threshold can be determined based on the work of Kitagawa-Takahashi (equation (2-10)) and El-Haddad (equation (2-11)). These methodologies were applied to fretting fatigue firstly by [Araújo & Nowell, 1999] and followed by [Fouvry et al., 2008]. The main difficulty was to calculate the stress intensity factor at the crack tip induced by fretting fatigue loading. Once the stress intensity factor can be calculated, this approach can be used to design components that risk fretting fatigue damage for an infinite lifetime. The idea is to ignore the crack nucleation damage and to determine that loading condition which would avoid crack growth following nucleation as schematically shown in Figure 5.1.

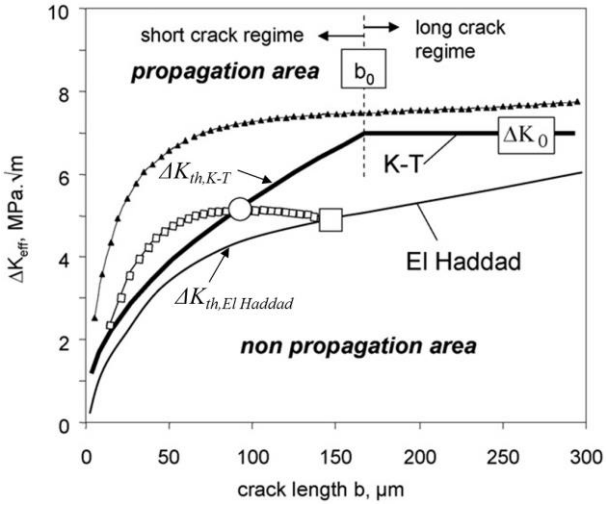

Figure 5.1 Kitagawa-Takahashi (K-T) and El Haddad curves for micro-crack thresholds [Fouvry et al., 2008]

3 Experimental approaches

3.1 Plain fatigue tests using pre-cracked specimens

The stress intensity factor threshold for a micro-crack, ΔK_{th}, proposed by [Kitagawa & Takahashi, 1976] and [El Haddad, Smith & Topper, 1979] (equations (2-10)&(2-11)) are not identical and there is no consensus on which of both is the optimal criterion. Therefore, there were some attempts to determine the threshold value experimentally by plain fatigue testing of pre-cracked specimens, eg. [Kubota et al., 2017]. The pre-crack length needs to be representative for a micro-crack. In their work, a single micro-crack length of $70\ \mu m$ (see Figure 5.2) was used to determine the corresponding stress intensity factor threshold from an S-N curve determined from plain fatigue tests.

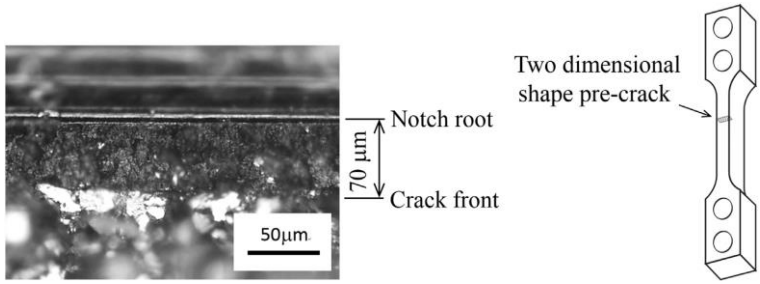

Figure 5.2 Pre-cracked specimen with an initial crack length of *70 µm* [Kubota et al., 2017]

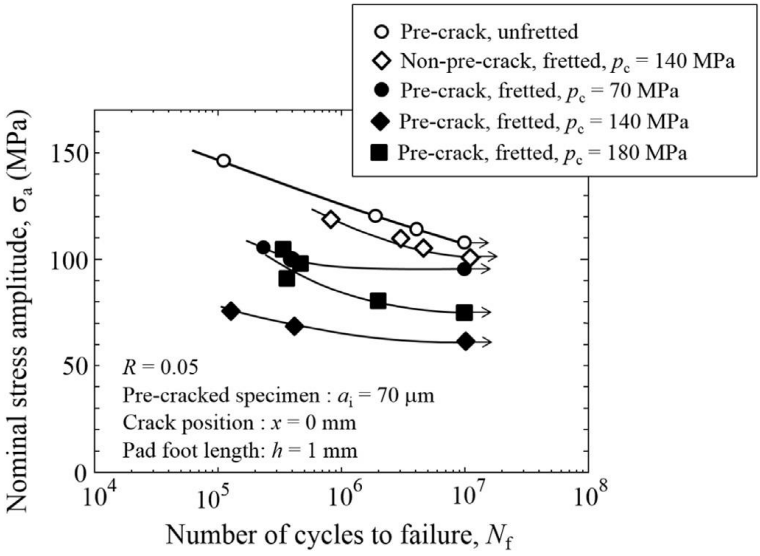

Figure 5.3 S-N test of pre-cracked specimen to determine ΔK_{th} [Kubota et al., 2017]

To introduce such a short crack, a fatigue pre-cracking procedure was performed on a notched specimen to obtain the desired crack length. Then the specimen surface covering the initial notch was removed by polishing to obtain a plain specimen having a sharp and short crack without the starter notch. The samples with the short crack were again fatigue loaded to determine the S-N curve shown in Figure 5.3 with a fatigue limit defined to correspond to 10^7 cycles (typical boundary of high cycle fatigue). The unbroken sample at this limit was cross-sectioned to reveal its crack length (*70 µm*). Combining this information with the corresponding load level, allowed to calculate the stress intensity factor threshold. A parametric study of the effect of contact pressure, bridge pad position with respect to the pre-crack and bridge pad stiffness on the determined stress intensity factor threshold was also conducted using a 3-D finite element model, Figure 5.3.

This approach could improve the uncertainty of the stress intensity factor threshold of micro-cracks developed by the previously discussed diagrams. However it requires the construction of an S-N curve which is known to be time consuming and expensive (several number of samples are required). The technique may even require an individual S-N curve for different short crack lengths.

3.2 Fretting fatigue tests with infrared thermography

In order to tackle the challenges posed by the higher discussed experimental technique, infrared thermography is utilized in this dissertation. It has been recognized in previous work [Colombo, Vergani & Burman, 2012; Fargione et al., 2002; Luong, 1998; Micone & De Waele, 2016; Montesano, Fawaz & Bougherara, 2013; Risitano & Risitano, 2010; Rosa & Risitano, 2000] that this technique could solve the time consuming and expensive nature of conventional S-N curve tests for plain fatigue. In contrast to the higher reported approaches, both analytical and experimental, thermography does not necessarily require a pre-crack in the specimen. It also allows to detect damage of a virgin specimen.

When components are subjected to cyclic loading, two main temperature responses are observed: reversible (first harmonic) and irreversible (higher harmonics and self-heating of the specimen). The reversible effect is the phenomenon that a temperate change introduced by loading (within the elastic range) will disappear after removal of the loading. This effect can only cause a temporary temperature change of the component and is normally within a range of a few *mK's*. A temperature change that remains even after removal of loading is called the irreversible effect and is mainly due to plasticity and friction. This effect is much more pronounced than the reversible one as it can go up to a few hundred *Kelvins*. The overall temperature response can be expressed by equation (5-1) [Berthel et al., 2014; Krapez, Pacou & Gardette, 2000]. It includes as first term the temperature rise of the specimen due to the irreversible effect, $T_0+\Delta T.f.t$, as second term the response due to the thermoelastic effect, i.e. the first harmonic $T_1 sin(\omega t+\varphi_1)$, and as third term the non-linear response due to the irreversible effect, i.e. the second harmonic $T_2 sin(\omega t+\varphi_2)$. Higher harmonics than the second order are normally neglected. While the irreversible effect is quite difficult to be quantified, the reversible effect can be quantified by a well-known thermoelastic relation developed by Lord Kelvin, equation (5-2) [Szolwinski et al., 1999].

$$T_{\exp}(t) = T_0 + \Delta T.f.t + T_1 \sin(\omega t + \varphi_1) + T_2 \sin(2\omega t + \varphi_2) \qquad \textbf{(5-1)}$$

$$T_1 = \left| -\frac{\alpha T_0}{\rho C_p}\ \sigma_{kk} \right| = \left| -k\sigma_{kk} \right| \qquad \textbf{(5-2)}$$

In the latter equation, α is the coefficient of thermal expansion, ρ is the mass density, C_p is the specific heat capacity at constant pressure, T_1 is the thermoelastic temperature amplitude, and σ_{kk} is the sum of the principal stresses, T_0 is initial temperature, and k is the thermoelastic constant. The minus sign (-) indicates that a positive stress (tension) will result in a drop of temperature whereas a negative stress (compression) will result in a rise of temperature, which is not very intuitive. This phenomenon can be explained as follows. A temperature rise normally results in a volumetric expansion of materials. If the volumetric expansion is prevented, a negative stress will develop. Therefore a temperature rise corresponds to a negative stress, Figure 5.4. Identically, a drop in temperature corresponds to a volumetric shrinkage or a positive stress.

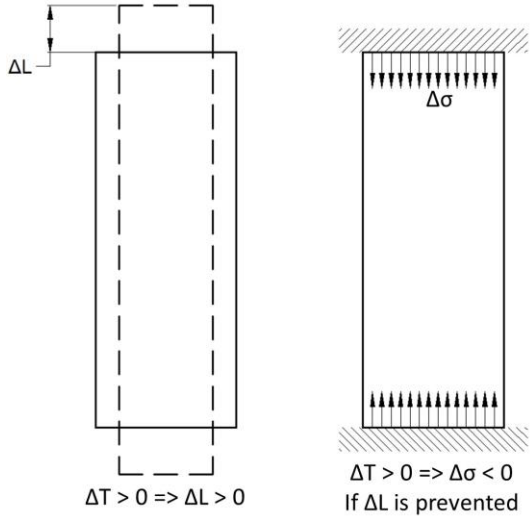

Figure 5.4 Schematic explanation of thermoelastic effect

Fatigue analysis with thermography

It is well-known that there is a correlation between the damage accumulated during the fatigue process and the heat dissipation. Based on the measurement of the temperature rise of the specimen due to the dissipated energy, the fatigue limit or even a complete S-N curve of metals can be determined. This thermal methodology has also been successfully applied to composite materials.

Instead of only measuring the temperature rise of the specimen, lock-in thermography allows to separate linear and non-linear temperature responses of materials, where the dissipated energy is linked to the non-linear response. An excellent review of four lock-in thermography algorithms can be found in [Krapez, 1998]. The temperature responses of the first and higher harmonics, or the linear and non-linear responses, are used to rapidly determine the heat dissipation and fatigue limit of metals [Krapez, Pacou &

Gardette, 2000]. For example, the so-called E- and D-mode algorithms developed by CEDIP are capable to measure directly the linear and non-linear temperature response of materials [Brémond, 2004; Bremond & Potet, 2001]. In another example, crack initiation in a weld was detected by separating temperature responses based on signal post-processing over each pixel of the thermal images [Ummenhofer & Medgenberg, 2009]. The linear temperature response was obtained by thermoelastic analysis of the loading signal, while the non-linear temperature response was calculated as the difference of the total experimental temperature and the linear response.

Fretting fatigue analysis with thermography

Damage accumulation during fretting fatigue is similar to plain fatigue except that surface damage due to friction is combined with the plastic deformation of materials. Infrared thermography has been shown to be an excellent non-destructive method for evaluation of fretting damage at closed surfaces of riveted lap joints [Forsyth et al., 2007]. It has furthermore been demonstrated that analysis of the first and second order harmonics using least-squares lock-in processing allows to separate the plastic deformation from the friction-induced surface damage in plain fretting conditions (without fatigue load) [Berthel et al., 2014]. The separation is achieved by comparing the temperature responses at a contact zone of the sample in an experiment, which take into account both friction and plasticity, and those of a thermal model which includes only the frictional effect. This allows to predict which load conditions, under plain fretting conditions, lead to a crack in the high cycle regime (defined as 10^6 cycles).

4 Development of an infrared thermographic methodology

The current study exploits the feasibility of the second harmonic to predict the fretting fatigue limit of two different metals. The fatigue stress level, and consequently also the tangential force imposed by the fretting pad, is increased stepwise in blocks. With thermal images recorded, temperature responses are analysed in the frequency domain via the Fast Fourier Transform (FFT) implemented in the commercial software Matlab. Different physical contributions are linked to the harmonics at specific frequencies. In particular, fretting fatigue damage is related to the harmonic at twice the loading frequency. Monitoring the second harmonic allows to identify the stress level below which no or negligible damage is found. This stress level is assumed to be the fretting fatigue limit.

4.1 Experimental set-up

A fretting fixture has been designed for installation on an ESH 100 kN servo hydraulic load frame, in order to perform fretting fatigue tests [De Pauw, De

Baets & De Waele, 2013] (Chapter 3.3). The normal clamping load, P, is applied to the specimen by a separate horizontal hydraulic actuator which loads the fretting pads mounted on flexural beams. The C-beam mounted on ertalon blocks can float freely on the base plate and ensures that the normal load is applied equally at both fretting pads. The tangential force, Q, between the dog-bone specimen and the pads is generated by the compliant springs as a result of the elastic deformation of the dog-bone specimen. The interaction of these forces on the specimen is shown on the photographs in Figure 5.5 and the schematic diagram in Figure 5.6.

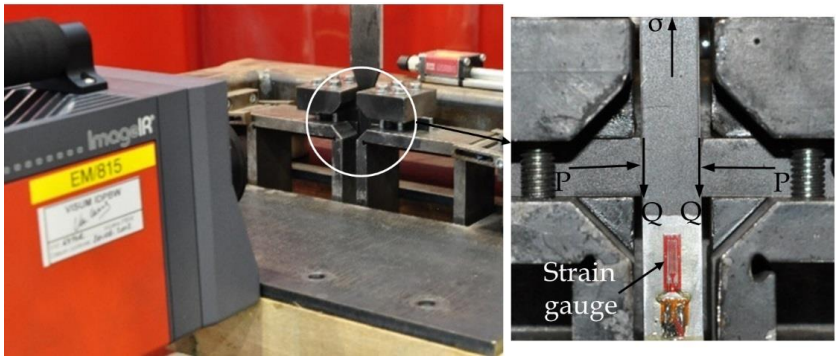

Figure 5.5 Experimental set-up

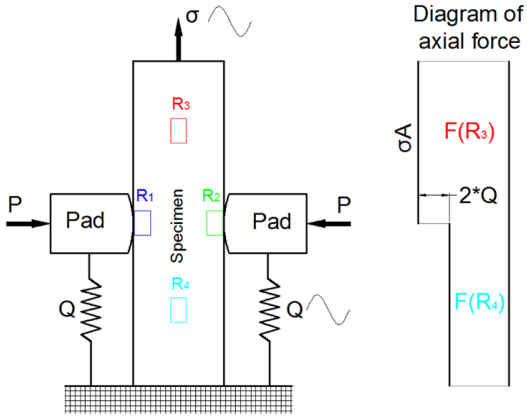

Figure 5.6 Interacting forces and diagram of axial force in a fretting fatigue test

The load cell mounted on the C-beam is used to directly measure the normal load. The tangential force generated by the compliant springs can be measured in two ways. First, as the difference between the force measured by the load cell of the ESH 100 kN and the force below the contact areas measured by a calibrated strain gauge mounted on the specimen surface (see Figure 5.5). Secondly, it can be calculated from the deflection of the springs based on a calibrated strain gauge attached on one of the springs. The latter

methodology has been used since it does not require the use of a strain gauge on each tested specimen; evidently it requires a calibration of the spring.

Fretting fatigue tests under ambient conditions with cylindrical pads against a plane specimen are performed and monitored by an infrared camera. The specimen and the pads are painted in black to improve their thermal emissivity. The infrared camera is an InfraTec ImageIR8300 model with a telephoto lens of *50 mm* focal distance. It is based on a focal plane array with InSb detectors cooled by a Stirling system. Its spatial resolution is *640* by *512* pixels and its temporal sensitivity at 25^0C is about *25 mK*. The camera is used with a default standard calibration with a temperature range of *5* to *60* ^0C and an integration time of *1 050* μs. The camera is installed at a distance of around *200 mm* from and perpendicular to the specimen surface. This corresponds to a pixel size of the thermal images equal to *65* μm, the lowest pixel size achievable.

4.2 Materials and specimens

A standard dog-bone specimen and cylindrical face pads are used in this study. Their materials are chosen to be identical, either aluminium alloy Al2024-T3 or either steel S235JRC. The Al2024-T3 is a tempered aluminium alloy for aerospace applications while the S235JRC is a cold drawn steel for structural applications. The materials' strength properties are summarized in Table 5.1 and detailed specimen dimensions are sketched in Figure 5.7.

Table 5.1 Strength properties of Al2024-T3 and S235JRC (3.1)

Materials	Young's Modulus E [GPa]	σ_y [MPa]	σ_{ult} [MPa]
Al2024-T3	73	383	506
S235JRC	210	650	700

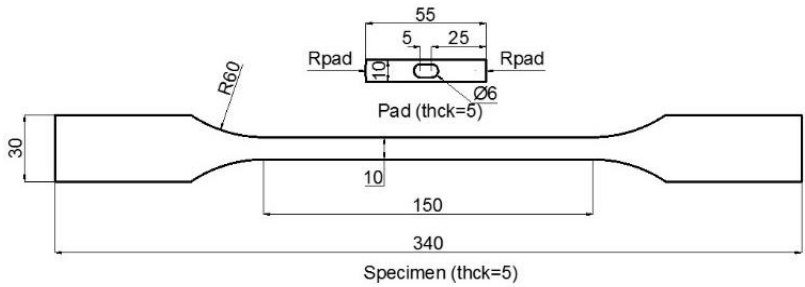

Figure 5.7 Dimensions of the specimen and the pad

The thicknesses of the specimen and the pads are designed to be equal to avoid possible edge effects. The dog-bone specimen's contact surface is plane, while the pad's contact surface is cylindrical. The cylindrical radius, R_{pad}, of

the aluminium and the steel pads are *50 mm* and *150 mm*, respectively. A groove in the pad facilitates its alignment with the specimen (see Chapter 3.3.1.2). The surface roughness of the aluminium alloy after milling resulted in an $R_a < 0.3\ \mu m$ while the structural steel samples had to be ground after milling to ensure an $R_a < 0.3\ \mu m$.

4.3 Sliding regimes in fretting

Fretting can be divided into two types of sliding regimes: partial slip and gross slip, depending on the sliding amplitude or the magnitude of the tangential force. Partial slip is considered to be a mix of sticking and slipping within the contact area at a low sliding amplitude while the entire contact areas will slip over each other if the sliding amplitude is increased. The latter case is defined as gross slip. Normally, a partial-slip regime is selected for fretting fatigue tests since cracking is the dominant damage while wear is more dominant for a gross-slip regime [Fouvry, Kapsa & Vincent, 1996]. To determine the transition between the two regimes, an approach used in [Hojjati Talemi et al., 2014] is adopted. The estimated partial-slip condition ($\sigma_{max} = 180\ MPa$, $R = 0.1$, $P = 1\ kN$) for Al2024-T3 is cyclically applied for 10^3 *cycles* since it was shown that after this duration, a steady state partial-slip regime could be achieved [Hills & Nowell, 1994]. After that, the fatigue force is immediately unloaded to a situation with tangential force equal to zero or without deflection of the compliant spring. Then, a monotonous quasi-static load equivalent to an axial stress of *325 MPa* is applied until the pads slip over the specimen, i.e the deflection of the compliant springs drop even though the axial load is increased. The maximum value which the tangential force reaches is defined as the border between the two regimes. The approach is also applied for the structural steel, and Figure 5.8 illustrates the two sliding regimes in fretting for both materials.

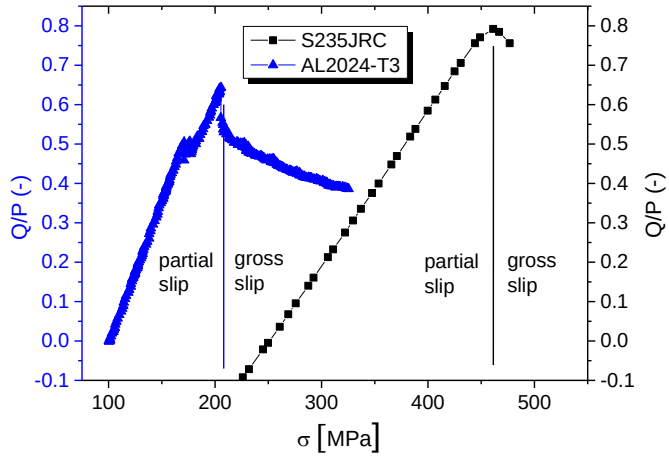

Figure 5.8 Sliding regimes in fretting for Al2024-T3 and S235JRC

4.4 Friction coefficient

At the beginning of fretting fatigue tests, the friction coefficient is rather low because of a good surface finish of the contacting virgin surfaces. The sliding regime normally begins with a macroscopic relative displacement. Due to surface removal and debris trapped in the contact, the friction coefficient rises and the sliding regime changes to partial slip or gross slip depending on what level of loading condition is applied, Figure 5.8. Normally, it is impossible to measure a friction coefficient under partial slip. Therefore, analytical solutions have been developed to estimate a partial slip friction coefficient from a mean value of friction coefficients at several points of the gross slip regime [Araújo & Nowell, 1999; Hills & Nowell, 1994]. [Hojjati Talemi et al., 2014] replace the mean friction coefficient in the equation by a friction coefficient at one exact gross slip point defined by material standard, which is based on a level of the relative displacement. On the other hand, [Fouvry, Kapsa & Vincent, 1996] point out that the friction coefficient at the transition between partial slip and gross slip can be simply used to represent the coefficient of friction under partial slip. Following the approach of [Fouvry, Kapsa & Vincent, 1996], the representative friction coefficient of Al2024-T3 and S235JRC in this study has been determined as *0.67* and *0.8*, respectively from the Figure 5.8. This value of Al2024-T3 is comparable to [Hojjati Talemi et al., 2014]'s method which determined the friction coefficient under partial slip of this material to be *0.65*.

4.5 Test procedure

The tests are run with a fatigue ratio ($\sigma_{min}/\sigma_{max}$) equal to *0*, a tangential load ratio (Q_{min}/Q_{max}) equal to *-1*, and a loading frequency of *10 Hz*. The maximum fatigue load (σ_{max}) is increased step by step as shown schematically in Figure 5.9. This enables a step-by-step increase of the maximum tangential load (Q_{max}) too, since the test rig is a single actuator with a spring system as shown in Figure 5.6 (Chapter 3.3). The normal load, P, is kept constant for all load steps. Test conditions of each load block are specified in Table 5.2 and Table 5.3.

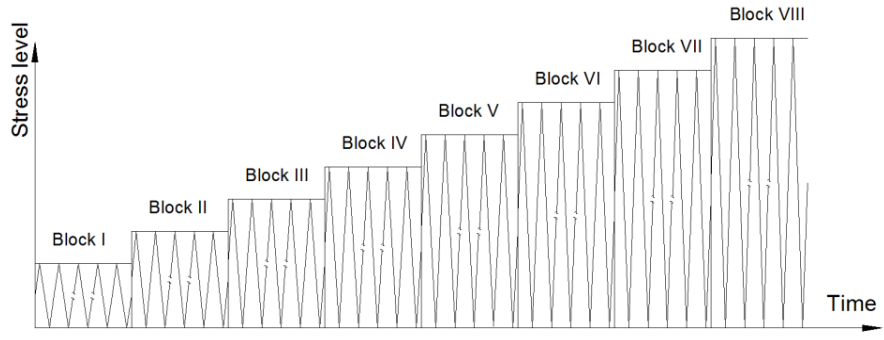

Figure 5.9 Stepwise block loading

Table 5.2 Test conditions for fretting fatigue limit of Al2024-T3

Blocks	σ_{max} [MPa]	Q_{max}/P [-]	Block duration [Cycles]	f [Hz]	R (σ_{min} / σ_{max}) [-]	P [kN]	R_{pad} [mm]
I	40	0.13	5 000	10	0	1	50
II	**60**	**0.18**	5 000				
III	80	0.24	5 000				
IV	100	0.29	5 000				
V	120	0.36	5 000				
VI	140	0.4	5 000				
VII	160	0.47	5 000				
VIII	180	0.5	5 000				

Each load step is run for *5 000 cycles* to ensure that a stabilized temperature is reached; the total duration of a test is only *40 000 cycles*. All data of the interacting forces are acquired with a sampling rate of *102.4 Hz* and logged into the ESH 100 kN control computer whereas thermal images are recorded with a frame rate of *100 Hz* on a separate laptop. Since the loading frequency is *10 Hz*, *10* data points are recorded for each load cycle, which can be considered to be oversampling and offers good accuracy of data processing, Chapter 4.2.2.

Table 5.3 Test conditions for fretting fatigue limit of S235JRC

Blocks	σ_{max} [MPa]	Q_{max}/P [-]	Block duration [Cycles]	f [Hz]	R (σ_{min} / σ_{max}) [-]	P [kN]	R_{pad} [mm]
I	80	0.08	5 000	10	0	1	150
II	120	0.12	5 000				
III	**160**	**0.17**	5 000				
IV	200	0.22	5 000				
V	240	0.27	5 000				
VI	280	0.31	5 000				
VII	320	0.4	5 000				
VIII	360	0.45	5 000				

4.6 Analysis of temperature response in fretting fatigue tests

4.6.1 Heat sources in fretting fatigue tests

As explained in section 3.2, temperature variation under cyclic loading is due to both elastic and inelastic effects. Likewise, heat generation in fretting fatigue experiments is due to these two effects. The inelastic effect in this case is caused by fretting friction, plastic dissipation, and other disturbing sources such as environmental temperature variations and heat conduction originating from the testing machine. Without any inelastic effect, the total temperature response will be determined by the thermoelastic effect which corresponds to the waveform of the mechanical load (a sinusoidal signal in this study). The sinusoidal function of the total temperature response will be distorted when an inelastic effect occurs, resulting in a temperature rise of the specimen towards a stabilization and then a non-perfect sinusoidal waveform, Figure 5.10.

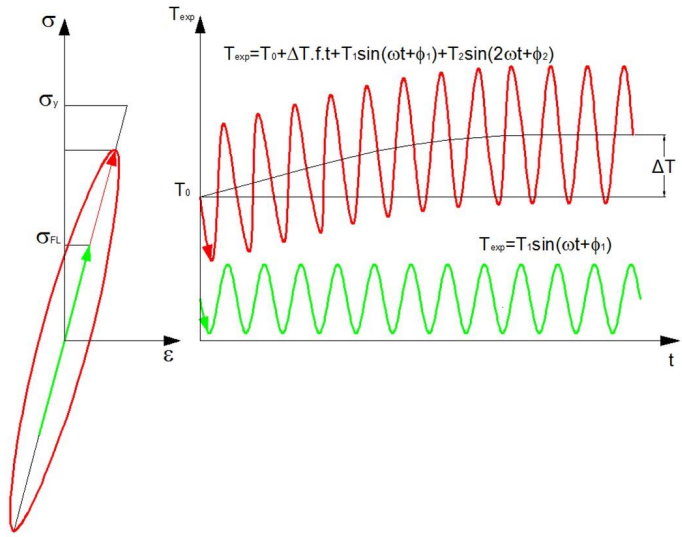

Figure 5.10 Heat sources in a fretting fatigue test

Two cases should be considered:

- If the total temperature response is periodic, a Fourier series decomposition allows any periodic function to be written as the sum of simple oscillating functions having a frequency equal to the multiples of the fundamental frequency, i.e. the loading frequency. Hence, the temperature variation at the specimen surface can be represented by equation (5-1) [Berthel et al., 2014; Krapez, Pacou & Gardette, 2000] where $T_1 sin(\omega t+\varphi_1)$ is the first harmonic effect (pure thermoelastic effect), $\Delta T.f$ and $T_2 sin(2\omega t+\varphi_2)$ are linear drift and second harmonic effect respectively, which account for friction,

plasticity and other disturbing factors. Higher harmonic effects are neglected. The temperature rise of the specimen, the second and higher harmonics are the results of the deviation from the thermoelastic response due to the inelastic effect.

- When the temperature response is not periodic, one can still decompose this function as a periodic function and a residue. Then, the periodic function is analyzed as in the first case. Therefore, the second harmonic and higher harmonics of the periodic function again account for most part of the inelastic effect. Of course, the residue function can also be used to study the inelastic effect [Ummenhofer & Medgenberg, 2009] but the second harmonic of the best fitted periodic function to the overall temperature response allows a more simple analysis.

Therefore, the second harmonic effect is used to study the fretting fatigue damage which is a combination of friction induced surface damage and plasticity.

4.6.2 Temperature decomposition and damage detection

Four regions of interest, ROIs, (see Figure 5.11) are selected from the recorded thermal images. The dimensions of each ROI are selected as *10* by *20* pixels which are approximately equal to *a* by 2*a,* where *a* is the Hertzian contact semi-width [Berthel et al., 2014; Chhith et al., 2017]. Such small region of interest allows a better sensitivity for the localized stress concentration occurring in fretting fatigue conditions [Szolwinski et al., 1999]. ROI's R_1 and R_2, see Figure 5.11, are the most important since they are located near the contact zones where the fretting fatigue damage or crack initiation will most likely occur [Chhith et al., 2017]. ROI's R_3 and R_4 are chosen above and below the contact regions respectively for reference purposes since they are only subjected to uniaxial fatigue load without fretting damage. The thermoelastic effect at these two ROIs allows to monitor the tangential force, which is measured by a calibrated strain gauge. The axial force distribution in a specimen subjected to fretting fatigue is discontinuous by a magnitude of $2Q$ at the contact points (see Figure 5.6). Equilibrium of forces in axial direction allows the tangential force to be determined as the difference between the axial forces above $F(R_3)$ and below $F(R_4)$ the contact points divided by *2*. Combining this with equation (5-2) allows to calculate the tangential force, Q, as a function of the temperature amplitudes at R_3 and R_4 as shown in equation (5-3). Here, A is a cross-sectional area of the specimen.

$$Q = \frac{F(R_3) - F(R_4)}{2} = \frac{\sigma_{kk}(R_3) - \sigma_{kk}(R_4)}{2} A = -\frac{A}{2k}\left(T_1(R_3) - T_1(R_4)\right) \qquad \textbf{(5-3)}$$

An FFT algorithm is used to determine the second harmonic temperature amplitude for each load block. The evolution of this temperature amplitude is used to determine the load block corresponding to the fretting fatigue

limit. This damage detection technique is believed to improve the method based on the self-heating of the specimen in which a separation of the different temperature contributions is not implemented [Brémond, 2004; Bremond & Potet, 2001; Krapez, Pacou & Gardette, 2000]. This technique is also assumed to be more robust in case the room temperature is not controlled.

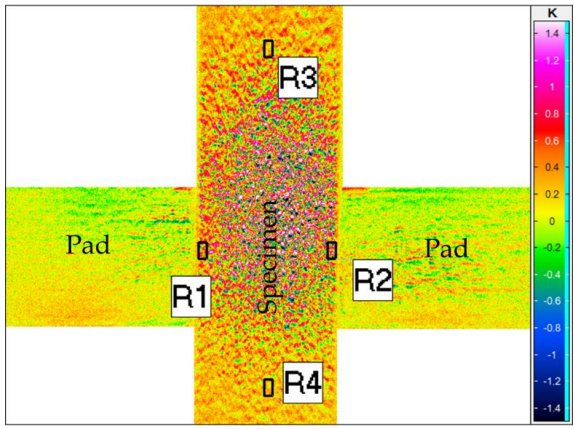

Figure 5.11 Temperature difference between the maximum and minimum axial stress at the beginning of the 7th load block (Al2024-T3)

Average temperature data corresponding to the four regions of interests are extracted from all recorded thermal images (*400 000* images) via the thermal CAM research software of InfraTec. The FFT is directly performed with Matlab for every series of *1 024* (=2^{10}) data points (corresponding to *102.4 cycles* or *10.24 seconds*) for all the ROIs in order to determine the first harmonic frequency, the frequency of the maximum temperature amplitude, since the temperature rise due to fretting fatigue is very small and its timing window is rather short, see Figure 5.12.

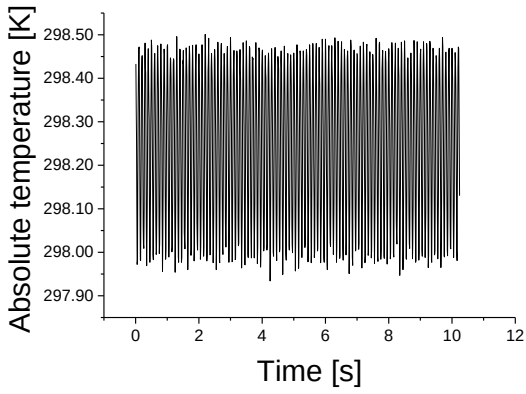

Figure 5.12 Temperature variation of the ROI R_2 in a time window of the 7th load block

Then, the second harmonic frequency is extrapolated so that the temperature amplitude at the second harmonic frequency can be determined. A result of the FFT analysis of the temperature recorded at ROI R_2 within one time window of load block I is shown in Figure 5.13 for material Al2024-T3. For this very low load level, the temperature response should be purely thermoelastic. However, higher modes at frequencies around 27 Hz and 45 Hz also exist. These frequencies do not correspond to multiples of the loading frequency. The magnitudes of these modes were found to be independent of the load levels. As an example, Figure 5.14 shows that their magnitudes for load block VII are very similar to those for load block I. It is therefore hypothesized that these modes are due to noises from the testing device. Hence, the temperature amplitudes at these modes (frequencies around 27 Hz and 45 Hz) are ignored in the following temperature analysis for the damage detection.

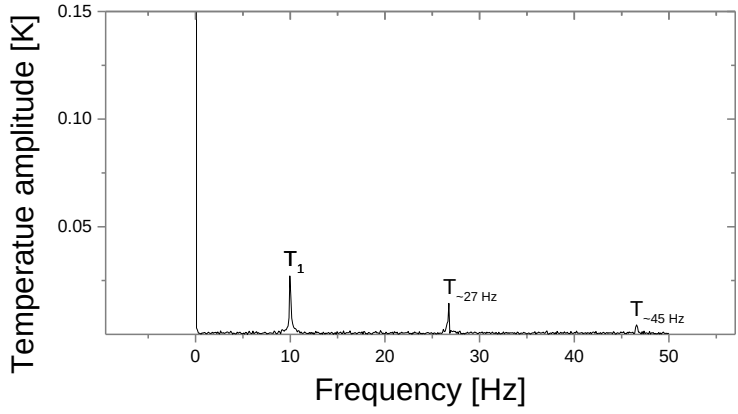

Figure 5.13 Frequency spectrum of the temperature at ROI R_2 during the 1st load block for material Al2024-T3

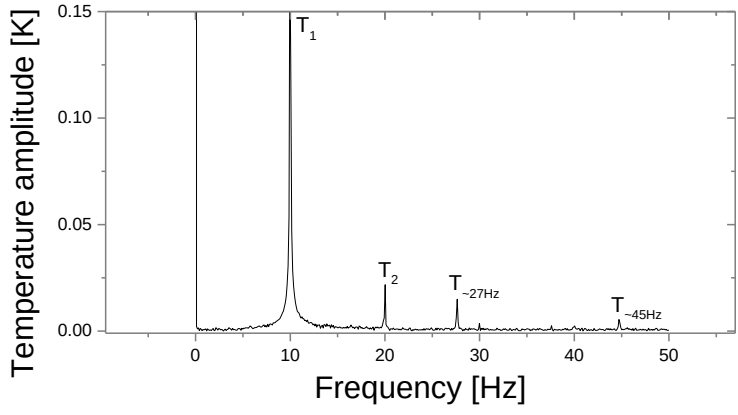

Figure 5.14 Frequency spectrum of the temperature at ROI R_2 during the 7th load block for material Al2024-T3

4.7 Results

Figure 5.15 and Figure 5.16 represent the evolutions of temperature amplitudes at the first harmonic and second harmonic frequencies respectively, during fretting fatigue tests on Al2024-T3 (see Table 5.2). The first harmonic temperature amplitude, T_1, is confirmed to be increasing with increasing load blocks due to the thermoelastic effect. From Figure 5.16, one can see that the first two load blocks do not generate any damage at all.

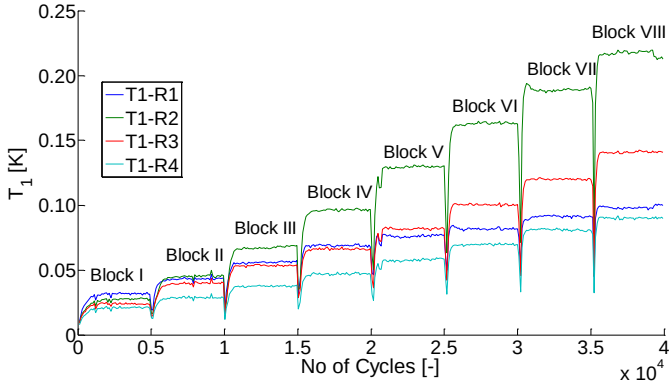

Figure 5.15 First harmonic temperature amplitude for Al2024-T3

The temperature levels T_2 at the contact areas R_1 and R_2 are at the same level as these at the remote areas R_3 and R_4. During the third load block, the temperature level at the right contact area R_2 starts to change and rises with increasing fatigue stress and tangential load level in the following blocks. However, a decrease in T_2 value is noticed during the last load block. In addition, the third harmonic, T_3, appears in this last load block (Figure 5.17). This phenomenon remains unexplained and needs further investigation. It is currently hypothesized that the damage mechanism may be different when the sliding regime shows a transition from a partial slip regime closer to gross slip conditions (see Figure 5.8).

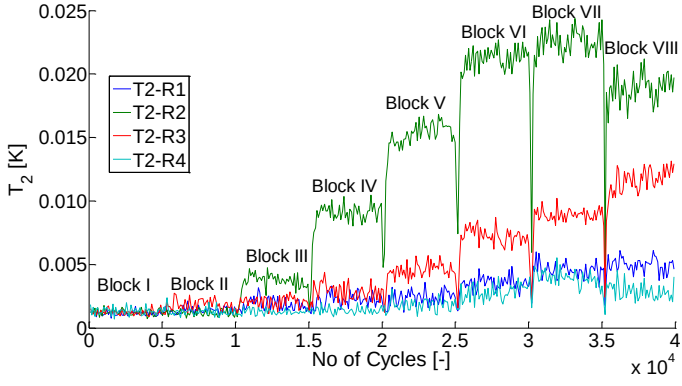

Figure 5.16 Second harmonic temperature amplitude for Al2024-T3

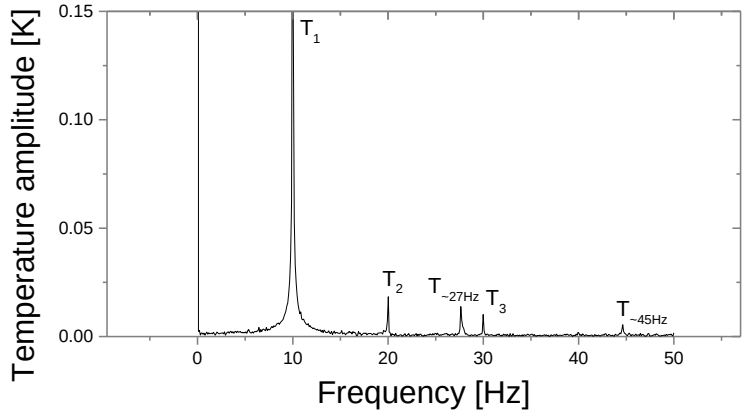

Figure 5.17 Frequency spectrum of the temperature at ROI R_2 during load block VIII for material Al2024-T3

Therefore, from Figure 5.16 one can conclude that the second load block is the best estimate of the fretting fatigue limit of the material since below this block, there is no sign of frictional energy loss. The test has been repeated three times to confirm this observation. Following, fretting fatigue tests with constant stress amplitude were run to verify the fretting endurance limit. For the aluminium alloy, the endurance limit is defined as the stress level that the specimen can survive for at least 10^7 cycles. The results in Figure 5.18 show that during a test with the load condition of the second load block, the specimen did indeed not fail at *10^7 cycles*.

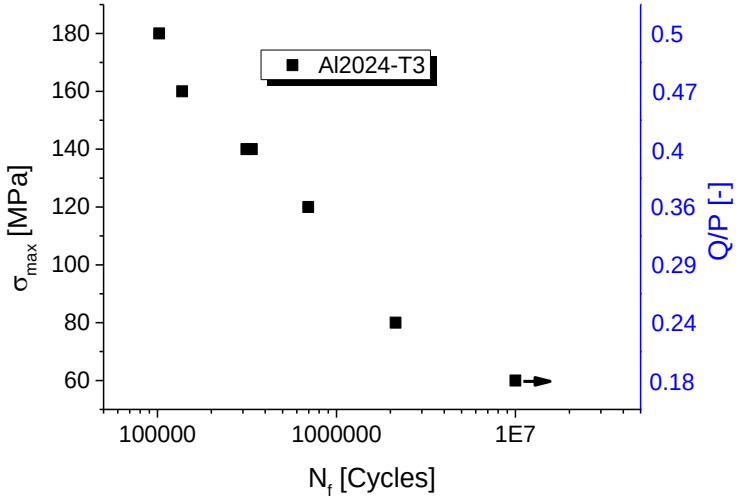

Figure 5.18 Lifetime curve for Al2024-T3

The same methodology has been applied to a specimen made of structural steel grade S235JRC. Test conditions are shown in Table 5.3. The thermoelastic temperature amplitude, T_1, is again observed to increase with

increasing load level (see Figure 5.19). The second harmonic temperature amplitude, T_2, at the left contact region R_1 deviates from the others after the fourth load block as illustrated in Figure 5.20. This means that the best estimate of the fretting fatigue limit corresponds to the stress level of the third load block. Again fretting fatigue tests with constant stress amplitude were performed and results are shown in Figure 5.21. The specimen remained intact at 10^7 *cycles* for the fretting fatigue test corresponding to the third load block.

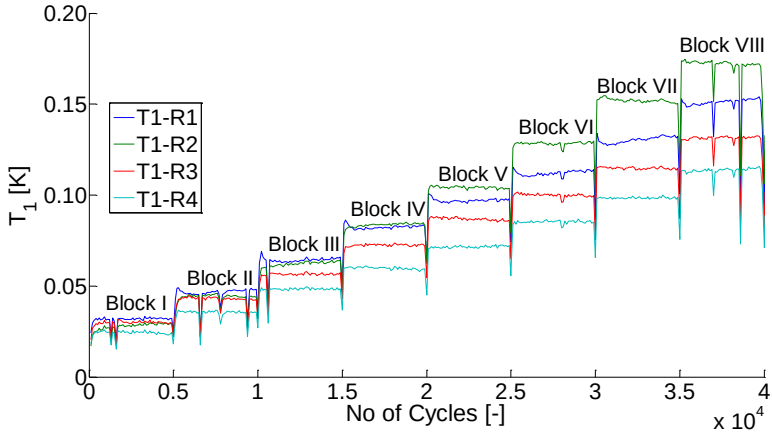

Figure 5.19 First harmonic temperature amplitude of S235JRC

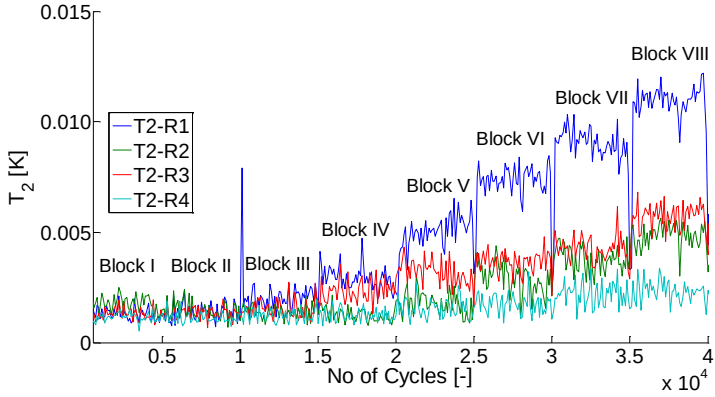

Figure 5.20 Second harmonic temperature amplitude of S235JRC

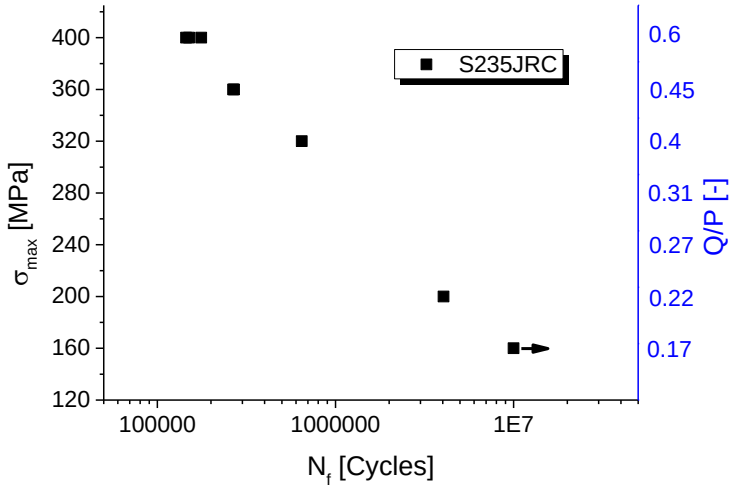

Figure 5.21 Lifetime curve for S235JRC

5 Summary and conclusions

The fretting fatigue limit (structural steel) or endurance limit corresponding to *10^7 cycles* (aluminium alloy) has been studied since fretting fatigue is considered as a high cycle fatigue regime with microscopic plastic deformation due to stress raisers by fretting. An analytical approach could be used to define a loading condition corresponding to crack arrest in order to obtain an infinite lifetime. This is done by ensuring that the stress intensity factor at the crack tip is lower than a (more or less) material property, the stress intensity factor threshold for micro-crack growth, which can be estimated by the approaches of Takashi-Kitagawa or El-Haddad. This threshold has been determined based on coupled experimental and numerical approaches [Kubota et al., 2017]. To that respect, plain fatigue tests on specimens containing a micro-crack have been conducted to determine an S-N curve. From the unbroken specimen at the endurance limit of 10^7 cycles, the corresponding stress level and its crack length revealed by optical microscopy has allowed to determine the stress intensity factor threshold of that short crack.

However, an experimental approach based on the S-N curve is known to be time consuming and expensive. Therefore an infrared thermographic method was developed for the rapid determination of the fretting fatigue limit. Fretting fatigue tests with a stepwise increased stress level (block loading) on Al2024-T3 and S235JRC specimens have been performed. Each load block was run for *5 000 cycles*, and the temperature evolution was monitored by an IR camera of InfraTec, model ImageIR8300. The temperature response of all load blocks has been post-processed in the frequency domain, using an FFT algorithm implemented in Matlab, to separate the different physical

contributions. The thermoelastic effect of the regions of interest above and below the contact zones, R_3 and R_4, allows to calculate the tangential force, Q. On the other hand, comparison of the second harmonic response at the contact zones, R_1 and R_2, to that of the remote regions, R_3 and R_4, gives a clear indication of that loading block which does not generate fretting fatigue damage. The stress at the transition from that load block which does not show any second harmonic response to that load block where the second harmonic response is visible, is determined as the best estimate of the fretting fatigue limit. Best estimates of the fretting fatigue and endurance limit for respectively steel and aluminium could be determined with one test lasting only a few hours. One additional sample was used for validation of the fretting fatigue limit. At this moment, a rather wide window between two load blocks is used to estimate the fretting fatigue limit. Increasing the number of load blocks would allow a more accurate determination of the fretting fatigue limit.

References

Araújo, J.A., Nowell, D. (1999) Analysis of Pad Size Effects in Fretting Fatigue Using Short Crack Arrest Methodologies. *International Journal of Fatigue*, 21, 947–56.

ASTM-E647-08 (2009) Standard Test Method for Measurement of Fatigue Crack Growth Rates 1.

Berthel, B., Moustafa, A.-R., Charkaluk, E., Fouvry, S. (2014) Crack Nucleation Threshold under Fretting Loading by a Thermal Method. *Tribology International*, 76, 35–44.

Brémond, P. (2004) IR Imaging Assesses Damage in Mechanical Parts: Determining the Fatigue Limit of Real Structures under Real Operating Conditions Saves Time. *Photonics Spectra*.

Bremond, P., Potet, P. (2001) Lock-In Thermography: A Tool to Analyse and Locate Thermo-Mechanical Mechanisms in Materials and Structures. In *SPIE*. pp. 560–6.

Chhith, S., De Waele, W., De Baets, P., Van Hecke, T. (2017) On-Line Detection of Fretting Fatigue Crack Initiation by Lock-in Thermography. *Tribology International*, 108, 150–5.

Colombo, C., Vergani, L., Burman, M. (2012) Static and Fatigue Characterisation of New Basalt Fibre Reinforced Composites. *Composite Structures*, 94, 1165–74.

De Pauw, J., De Baets, P., De Waele, W. (2013) Design of a Fretting Fatigue Test Rig. *Journal of Sustainable Construction and Design*, 4, 6 Pages.

El Haddad, M.., Smith, K.N., Topper, T.H. (1979) Fatigue Crack Propagation of Short Cracks. *Journal of Engineering Materials and Technology*, 101, 42–6.

Fargione, G., Geraci, A., Rosa, G. La, Risitano, A., Doria, V.A. (2002) Rapid Determination of the Fatigue Curve by the Thermographic Method. *International Journal of Fatigue*, 24, 11–9.

Forsyth, D., Genest, M., Shaver, J., Mills, T. (2007) Evaluation of Nondestructive Testing Methods for the Detection of Fretting Damage. *International Journal of Fatigue*, 29, 810–21.

Fouvry, S., Kapsa, P., Vincent, L. (1996) Quantification of Fretting Damage. *Wear*, 200, 186–205.

Fouvry, S., Nowell, D., Kubiak, K., Hills, D. a. (2008) Prediction of Fretting Crack Propagation Based on a Short Crack Methodology. *Engineering Fracture Mechanics*, 75, 1605–22.

Hills, D.A., Nowell, D. (1994) *Mechanics of Fretting Fatigue*. Kluiwer Academic

Publishers, Dordrecht.

Hirakawa, K., Toyama, K., Kubota, M. (1998) The Analysis and Prevention of Failure in Railway Axles. *International Journal of Fatigue*, 20, 135–44.

Hojjati-talemi, R., Wahab, M.A., De Pauw, J., De Baets, P. (2014) Prediction of Fretting Fatigue Crack Initiation and Propagation Lifetime for Cylindrical Contact Configuration. *Tribology International*, 76, 73–91.

Kitagawa, H., Takahashi, S. (1976) Application of Fracture Mechanics to Very Small Cracks or the Cracks in the Early Stage. *American society of metals*, 627–30.

Kondo, Y., Sakae, C., Kubota, M., Yanagihara, K. (2005) Non-Propagating Crack Behaviour at Giga-Cycle Fretting Fatigue Limit. *Fatigue Fracture of Engineering Materials and Structures*, 28, 501–6.

Krapez, J.. (1998) Compared Performances of Four Algorithms Used for Modulation Thermography. In *Quantitative Infrared Thermography 4*. pp. 148–53.

Krapez, J.C., Pacou, D., Gardette, G. (2000) Lock-in Thermography and Fatigue Limit of Metals. In *Quantitative Infrared Thermography 5*. pp. 277–82.

Kubota, M., Kataoka, S., Takazaki, D., Kondo, Y. (2017) A Quantitative Approach to Evaluate Fretting Fatigue Limit Using a Pre-Cracked Specimen. *Tribology International*, 108, 48–56.

Luong, M.P. (1998) Fatigue Limit Evaluation of Metals Using an Infrared Thermographic Technique. *Mechanics of Materials*, 28, 155–63.

Micone, N., De Waele, W. (2016) On the Application of Infrared Thermography and Potential Drop for the Accelerated Determination of an S-N Curve. *Experimental Mechanics*, 57, 143–53.

Miller, K.J. (1993) The Two Thresholds of Fatigue Behaviour. *Fatigue & Fracture of Engineering Materials & Structures*, 16, 931–9.

Montesano, J., Fawaz, Z., Bougherara, H. (2013) Use of Infrared Thermography to Investigate the Fatigue Behavior of a Carbon Fiber Reinforced Polymer Composite. *Composite Structures*, 97, 76–83.

Risitano, A., Risitano, G. (2010) Cumulative Damage Evaluation of Steel Using Infrared Thermography. *Theoretical and Applied Fracture Mechanics*, 54, 82–90.

Rosa, G. La, Risitano, A. (2000) Thermographic Methodology for Rapid Determination of the Fatigue Limit of Materials and Mechanical Components. *International Journal of Fatigue*, 22, 65–73.

Schijve J (2009) *Fatigue of Structures and Materials*. Springer Science+ Business Media, B. V.

Szolwinski, M.P., Harish, G., Farris, T.N., Sakagami, T. (1999) In-Situ Measurement of Near-Surface Fretting Contact Temperatures in an Aluminum Alloy. *Journal of Tribology-Transactions of the ASME*, 121, 11–9.

Ummenhofer, T., Medgenberg, J. (2009) On the Use of Infrared Thermography for the Analysis of Fatigue Damage Processes in Welded Joints. *International Journal of Fatigue*, 31, 130–7.

Wagner, D., Ranc, N., Bathias, C., Paris, P.C. (2009) Fatigue Crack Initiation Detection by an Infrared Thermography Method. *Fatigue & Fracture of Engineering Materials & Structures*, 12–21.

Chapter 6 Fretting fatigue crack initiation

"In this chapter, different components of temperature responses recorded during fretting fatigue tests are used to detect crack initiation. Both off-line and on-line methods are described. The on-line technique is evaluated using two different materials and two contact types under fretting fatigue conditions"

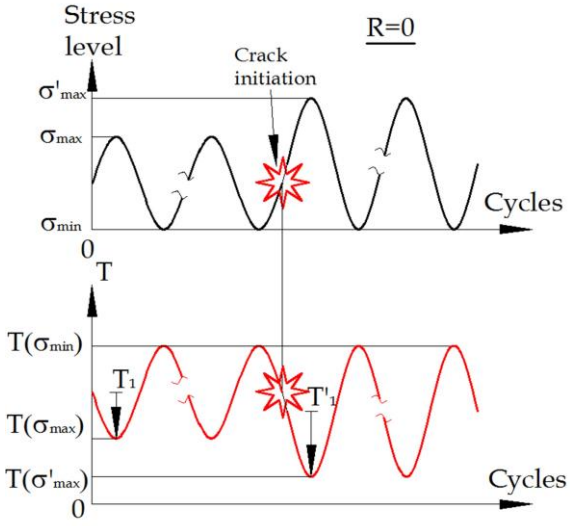

1 Introduction

A fatigue crack nucleates as a result of energy loss or damage accumulation. The origin of damage accumulation depends on the type of fatigue. For low cycle fatigue, the energy loss is a result of bulk plastic deformation while for high cycle fatigue damage is caused by localized plastic deformation due to persistent cyclic slip [Schijve J, 2009]. In ultra high cycle fatigue, the crack nucleates from material impurities like inclusions [Wagner et al., 2009]. Even though fretting fatigue is considered as high cycle fatigue, because of the localized plastic deformation from the contact loads, the exact origin of crack nucleation remains uncertain [Fellows, Nowell & Hills, 1997]. Fretting fatigue crack initiation occurs in a closed contact between two interacting bodies and generally at the centre of the contact bodies since it was shown that contact pressure is more severe in plane strain condition than in plane stress [Johnson, 1985]. This makes detection of fretting fatigue crack initiation very challenging and does not allow to adopt the optical techniques to visualize the crack initiation process as in plain fatigue experiments. So far, only a very limited number of techniques have been reported that allow detection of crack initiation in fretting fatigue conditions. To the author's best knowledge, only optical microscopy and electrical resistance changes [Endo & Goto, 1976] or voltage changes [Kondo et al., 2005; Meriaux et al., 2010] due to crack appearance have been successfully utilized. In this work, infrared thermography is used in an attempt to tackle this challenge.

Material damage and cracking can be studied by a straightforward temperature analysis or by a conversion from temperature field to stress field based on the thermoelastic effect, called Stress Pattern Analysis by Temperature Emission (SPATE) [Silva et al., 2000; Tomlinson & Patterson, 1997]. The latter methodology is limited by the spatial resolution of the camera in case materials are subjected to non-uniform stresses [Szolwinski et al., 1999], and the level of loading on the material must be in the elastic range. For the former methodology, two approaches of thermography have been used in plain fatigue and plain fretting. One is evaluating the mean temperature increase of samples, *D.C.* ("direct current") component [Colombo, Vergani & Burman, 2012; Fargione et al., 2002; Luong, 1998; Micone & De Waele, 2016; Montesano, Fawaz & Bougherara, 2013; Risitano & Risitano, 2010; Rosa & Risitano, 2000] and the other one is the analysis of the cyclic temperature response, *A.C.* ("alternating current") component [Ummenhofer & Medgenberg, 2009]. Combinations of the two approaches are used by [Bremond & Potet, 2001; Krapez, Pacou & Gardette, 2000] and [Berthel et al., 2014]. The second approach naturally provides a few more parameters (first harmonic, second harmonic, and phase shift) to evaluate material behaviour but requires advanced signal processing. All these approaches are adopted in this thesis to investigate the detectability of fretting fatigue crack initiation in a closed contact.

2 Off-line detection of fretting fatigue crack initiation by thermography

In this section, an infrared thermography technique to detect fretting fatigue crack initiation based on a component of the main temperature signal is elaborated. It is based on the absolute temperature corresponding to the maximum tensile stress within one fatigue cycle; since it is hypothesized that crack initiation will result in the largest temperature disturbance at the maximum tensile stress [Chhith, De Waele & De Baets, 2015].

2.1 Temperature at the maximum tensile stress as parameter to detect crack initiation

A fretting fatigue test (σ_{max} = *175 MPa*, *P = 600 N*, Q_{max}/P = *0.36*) on a dog-bone specimen and cylindrical pads is run at a frequency of *10 Hz* with a fatigue ratio of *R = 0.1* and a tangential force ratio of *-1*. All samples are made from aluminium alloy Al2024-T3. The IR camera, installed at a distance around *200 mm* perpendicular to the specimen surface, records thermal images at a frequency of *100 Hz* to have an oversampling rate, 10 data points per cycle. The typical size of a full-frame thermal image (*640* x *512 pixels*) is approximately *1.5 MB* so that for this test of *250 000 cycles* total lifetime a disk space of *3.75 TB* would be required to store and analyse all data. This storage issue forces the recording of thermal images with only a portion of the full-frame image, Figure 6.1 (spatial resolution lesser than *640* x *512 pixels*), and only during the last *50 000 cycles* of the test before the final rupture of the specimen since the space of the hard drive of the IR camera laptop is only *300 GB*. A large external hard drive can be a solution to monitor the whole fretting fatigue test, but recording thermal images on an external hard drive sometimes leads to freezing of the recording process and the IR camera could not work properly if millions of images need to be captured. This storage issue is not a surprise for the thermography method. [Ummenhofer & Medgenberg, 2009] and [Ranc, Wagner & Paris, 2008] had to find different solutions for the same storage problem. Even, [Berthel et al., 2014] mentioned that continuous measurement of the temperature by an IR camera is impractical.

After failure of the specimen, the evolution of temperature of each region of interest on the specimen surface is extracted with the thermal CAM research software IRBIS3 of InfraTEC, Figure 6.1. Dimensions and reasons for this selection of regions of interest are the same as discussed in Chapter 5.4.6.2. Among the *10* data points recorded in one cycle, a minimum temperature is searched and taken as the parameter for detection of the crack. Remember well that a minimum temperature corresponds to a moment of maximum elastic tensile stress in the cycle (see Figure 6.2) according to equation (3-2).

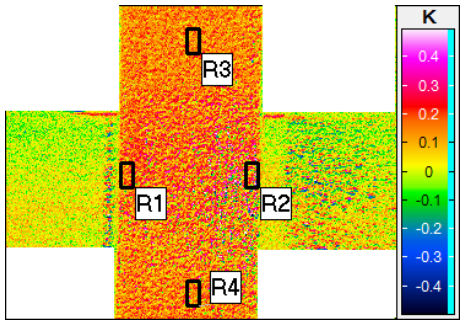

Figure 6.1 Portion of full-frame thermal image with four regions of interest

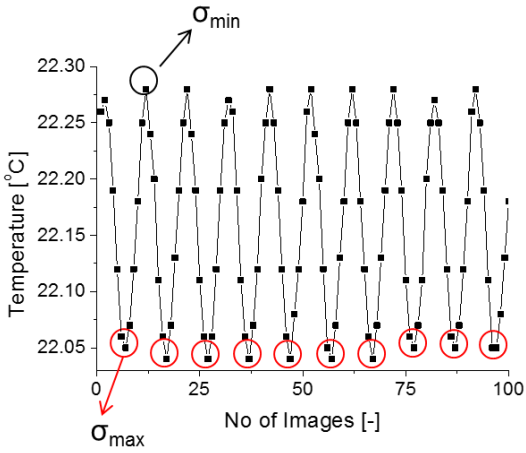

Figure 6.2 Selected temperature parameter for crack detection

The evolution of the temperature at the four ROIs corresponding to the maximum stress is plotted as a function of number of fatigue cycles in Figure 6.3. In this figure, the data at the start of the fretting fatigue test is missing due to storage issues. The temperature data is available only from *200 000 cycles* onwards (the last *50 000 cycles* before the estimated total lifetime of *250 000 cycles*). T_{ref} is the first temperature recorded. The lifetime to failure was estimated based on a trial test with the same loading conditions without the IR camera. The temperature change (T-T_{ref}) at all the ROIs stabilizes after a running-in stage until approximately *224 000 cycles* when the temperature change at R_2, right side of the contact zone, starts to deviate from the other three ROIs. Since a change in absolute temperature is reported, the stabilized regime is not a horizontal line but a curve common to the four regions of interest which follows the effect of the room temperature. The magnitude of the temperature change is increasing until the final rupture of the specimen (N_f = *242 000 cycles*). This is due to the presence of a crack at that contact zone, R_2. A fracture surface analysis of the failed specimen showed that the specimen failed due to a fretting fatigue crack initiating at this side, Figure 6.4. This result suggests that the technique can be used to detect fretting

fatigue crack initiation and thus separating lifetime of crack initiation, N_i, from crack propagation lifetime, N_p.

From the temperature evolution, the lifetime of crack propagation can be determined to be N_p = *18 000 cycles* if a temperature deviation from the stabilized temperature larger than the nominal noise of the camera, *25 mK*, is taken as the crack initiation criterion. As the temperature analysis is performed off-line, it is very difficult to determine the crack size at the assumed transition from initiation to propagation. Two approaches can be used to estimate this crack length based on the lifetime of crack propagation: counting the number of striations on the fracture face with a scanning electron microscope (SEM) or using analytical solutions. However, visualizing fatigue striations in fretting fatigue can be cumbersome [Lykins, Mall & Jain, 2001]. Therefore, an analytical approach is chosen and reported in the next section .

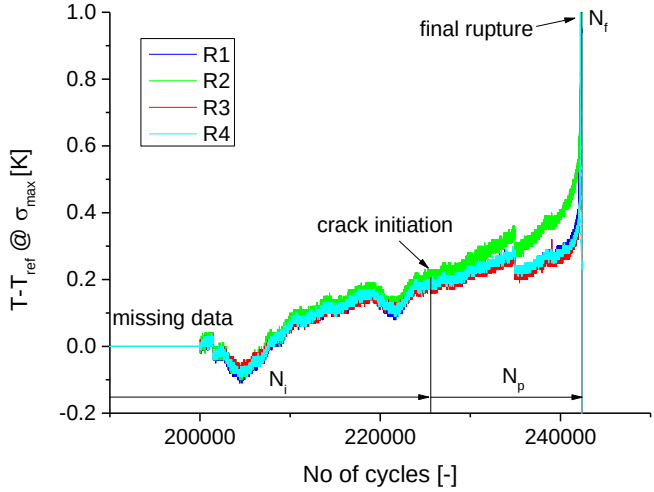

Figure 6.3 Temperature evolution at maximum fatigue load

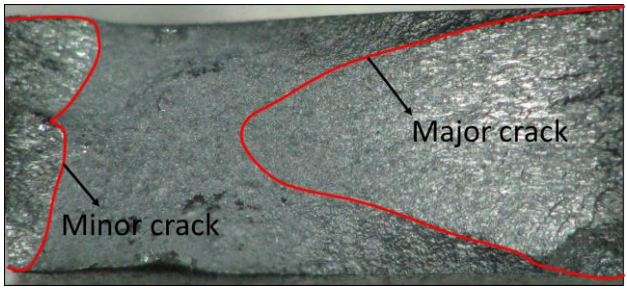

Figure 6.4 Fracture surface of the specimen illustrating that the dominant crack starts from the contact zone at the right side

2.2 Analytical solution for crack propagation

From a theoretical point of view, an initiated crack should be defined as that crack length below which continuum mechanics can be applied to predict the cycles needed to initiate that crack and above which fracture mechanics can be applied to predict the crack propagation stage. This boundary crack length is typically rather small, several microns, to ensure that there is no continuum breakdown and that application of the continuum mechanics is still valid [Dowling, 1979; Socie, Morrow & Chen, 1979]. However, from an experimental perspective, detecting such a micro-crack is almost impossible. Therefore, researchers define different crack lengths for the crack initiation depending on the detectability limit of the equipment used, even though they realize that this assumption could lead to a level of error in predicting lifetime from their models. [Araújo & Nowell, 2002; Szolwinski & Farris, 1998, 1996] defined crack initiation for their fretting fatigue study to be a crack length of *1 mm* because they didn't have any instrumentation to detect crack initiation. To obtain the experimental lifetime of crack initiation, subtraction of the number of cycles of crack propagation (initial crack length of *1 mm*) from the total number of cycles realized in the test was done. The propagation lifetime could be easily determined by the Paris law, equation (6-1) [Szolwinski & Farris, 1998, 1996].

$$\frac{db}{dN} = C\left(\Delta K_I\right)^{\mathrm{m}} \tag{6-1}$$

$$N_{\mathrm{p}} = \int_{\mathrm{b_{1mm}}}^{b_f} \frac{db}{C\left(\Delta K_I\right)^{\mathrm{m}}} \tag{6-2}$$

Where, b is the crack length, N is number of cycles, ΔK_I is the stress intensity factor range of mode I, C and m are constants of the Paris law. For the aluminium alloy Al2024-T3: $C = 3.59 \times 10^{-9}$ and $m = 3.387$ [Szolwinski & Farris, 1998]. Lifetime of crack propagation N_p from an initial crack length of *1 mm*, b_{1mm} until final rupture b_f (half of the specimen width) [Szolwinski & Farris, 1998] can be determined from the integration, equation (6-2), if the stress intensity factor range is known. A fretting fatigue crack is normally a semi-elliptical crack (see Figure 6.5) so that the stress intensity factor at the crack tip under mode I can be calculated by equation (6-3) [Szolwinski & Farris, 1996].

$$\mathrm{K_I} = 1.12\left(\frac{\sigma\sqrt{\pi b}}{\pi}\right) \tag{6-3}$$

Inserting equation (6-3) into equation (6-1) with the loading conditions from the experiment described in section 2.1, the number of cycles for crack propagation is found to be $N_p = 19\,000$ *cycles*. Note that this procedure cannot

take fretting loads, *P* & *Q*, into account. Only the effect of the fatigue load σ on the propagation lifetime can be studied (see equations (6-1),(6-2), and (6-3)). By comparing this analytical solution of crack propagation lifetime, $N_{p,analytical} = 19\ 000\ cycles$ to the experimental value reported in the previous section, $N_{p,experiment} = 18\ 000\ cycles$, one could conclude that the off-line thermography method, section 2.1, is able to detect crack initiation with a crack length around *1 mm*. This detection threshold is rather large, as it is not possible to study the effect of the fretting loads, *P & Q*, on the crack initiation lifetime. The interest of a fretting fatigue study should be on smaller cracks propagating near the contact zones. Otherwise, one is studying plain fatigue rather than fretting fatigue. Hence, it does not make sense to continue using this approach. In addition to that, a huge amount of experimental data at the beginning of the test is missed due to storage issues and it is also possible that as a result the moment of crack initiation is missed. If a lower stress level would be applied, a longer lifetime would be generated so that even a much larger amount of the experiment would be missed.

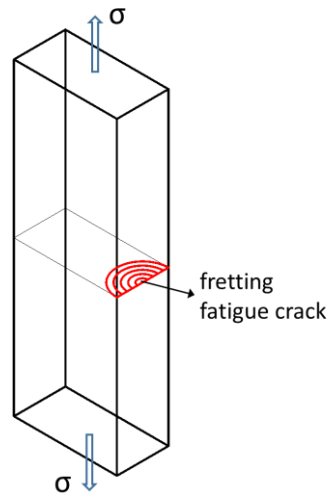

Figure 6.5 Semi-elliptical crack produced by fretting fatigue

3 On-line detection of fretting fatigue crack initiation by thermography

Usually thermal images are captured before the data (temperature) can be extracted and post-processed. This common practice does not allow continuous measurement during long experiments like fatigue, see section 2.1. This drawback has so far restricted researchers to a number of practices even though they realized the potential of thermography to investigate material damage under cylic loadings. The practices include intermittent capturing of sequences of thermal images, and indirect evaluation of the

material damage via intermediate analytical or numerical models. For the former issue, gaps between each sequence can be large while for the latter issue, the duration of the test needs to be short so that the temperature recoding can be done for the whole test. The temperature data from such short test are used as inputs to the models for prediction of fatigue limit, complete S-N curve, and crack initiation lifetime.

In this section, an on-line methodology for fretting fatigue crack initiation by thermography is discussed, based on the opportunity of the current IR camera model for on-line data acquisition using a Matlab script, Chapter 4.4.2. In addition to that, the *A.C.* component (its temperature amplitude T_a) instead of the temperature at the maximum stress is used as parameter to improve the detection threshold. The first harmonic temperature amplitude, T_1, is also extracted from the main signal in order to demonstrate that this is a better parameter for crack detection since T_1 is in a direct relation with the sum of the principal stresses, equation (3-2). Occurrence of a crack will cause a stress concentration which disturbs this equation. If the test is performed with a fatigue ratio $R = 0$, the maximum stress is increased at crack initiation while the minimum stress remains zero. Thus the maximum thermoelastic temperature stays constant whereas the minimum thermoelastic temperature drops. As a consequence, the thermoelastic temperature amplidue, T_1, is increased at crack initiation, Figure 6.6.

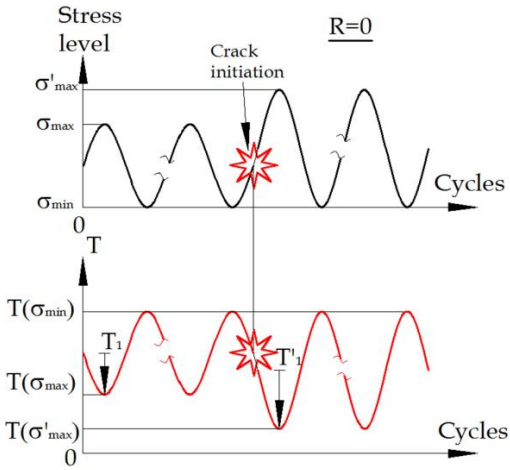

Figure 6.6 Effect of crack initiation on the thermoelastic relation at $R = 0$

3.1 Line contact

3.1.1 Test conditions and materials

Fretting fatigue tests using cylindrical pads against a flat specimen are performed and monitored with an infrared camera under ambient conditions, Figure 5.5. Materials of the pads and the specimen are identical

and made of aluminum alloy Al2024-T3 and structural steel S235JRC (see Table 6.1 for their strength properties). Specimen and pads were painted in black to improve their thermal emissivity. Their dimensions are illustrated in Figure 3.16. Conditions of fretting fatigue tests were selected to realize a partial slip regime and to ensure that no global plasticity would occur in the test specimens (see Table 6.2 and Figure 5.8). The maximum contact pressure, p_0, for Al2024-T3 and S235JRC is found to be *226 MPa* and *221 MPa* respectively (well below their yield strengths), based on the equation in Chapter 2.1.1. The tests are run with constant fatigue amplitude and a fatigue ratio ($\sigma_{min}/\sigma_{max}$) of *0.001*, constant amplitude of tangential force and a tangential load ratio (Q_{min}/Q_{max}) of *-1*, a constant normal load, *P*, and a loading frequency of *5 Hz*. The surface roughness of the aluminium alloy after milling resulted in an $R_a < 0.3\ \mu m$ while the structural steel samples had to be ground after milling to ensure an $R_a < 0.3\ \mu m$.

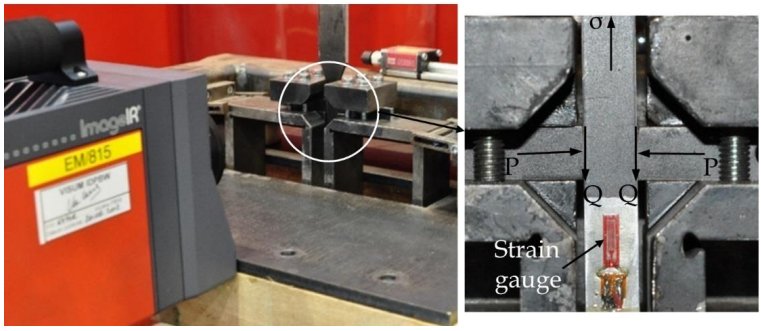

Figure 6.7 Experimental set-up

Table 6.1 Strength properties of Al2024-T3 and S235JRC

Materials	Young's Modulus E [GPa]	σ_y [MPa]	σ_{ult} [MPa]
Al2024-T3	73	383	506
S235JRC	210	650	700

Table 6.2 Test conditions

Test no.	σ_{max} [MPa]	f [Hz]	R (σ_{min} /σ_{max}) [-]	P [kN]	Q_{max} /P [-]	R_{pad} [mm]	p_0 [MPa]
CI_Al202401	200	5	0.001	1	0.61	50	226
CI_Al202402	200	5	0.001	1	0.61	50	226
CI _Al202403	187.5	5	0.001	1	0.59	50	226
CI _S235JRC01	440	5	0.001	1	0.71	150	221
CI _S235JRC02	400	5	0.001	1	0.6	150	221

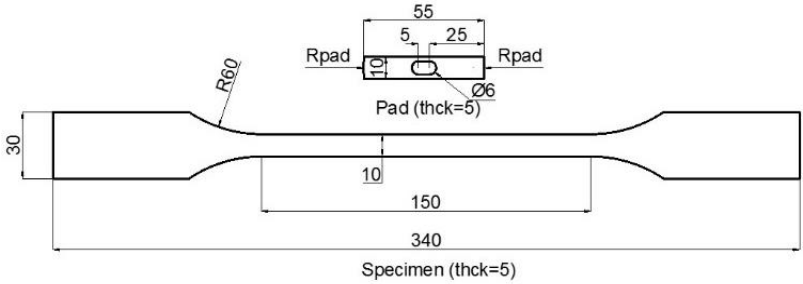

Figure 6.8 Dimensions of the specimen and the pad

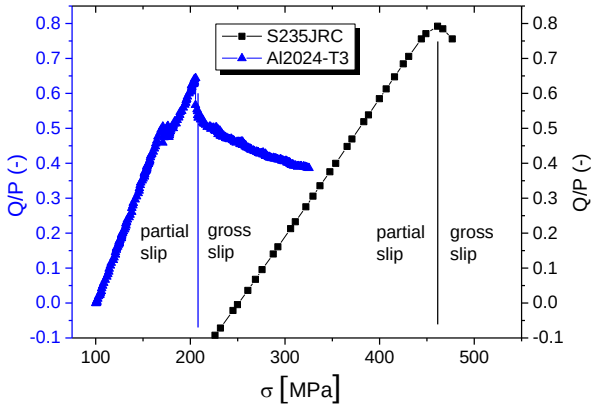

Figure 6.9 Sliding regimes under fretting for Al2024-T3 and S235JRC

3.1.2 Experimental procedure

With the infrared camera model ImageIR8300, access to temperature data is made possible with a Matlab script. The maximum on-line data acquisition rate is limited to *50 Hz* and therefore the loading frequency is set at *5 Hz*. The experimental procedure is schematically illustrated in Figure 6.10. Full-frame thermal images (*640* x *512 pixels*), Figure 4.4, are recorded via InfraTEC CAM software, IRBIS3, for the first *1 000 cycles* during which a steady state partial slip regime is reached [Hills & Nowell, 1994]. Locations of the highest temperature at the contacts, R_1 and R_2, can be defined as visualized in the thermal image. These regions are anticipated to be the regions with the highest stress concentration due to fretting and thus crack initiation. On the other hand, regions R_3 and R_4 are selected above and below the contact regions respectively. These are chosen for reference purposes, and their temperature difference allows to monitor the tangential force based on basic thermoelastic effect (direct relation between the temperature variation and the stress range). Dimensions of all regions of interest are *10* by *20* pixels, which is around *a*x2*a* as selected in [Berthel et al., 2014] where *a* is the contact half-width (*63 μm* for Al2024-T3).

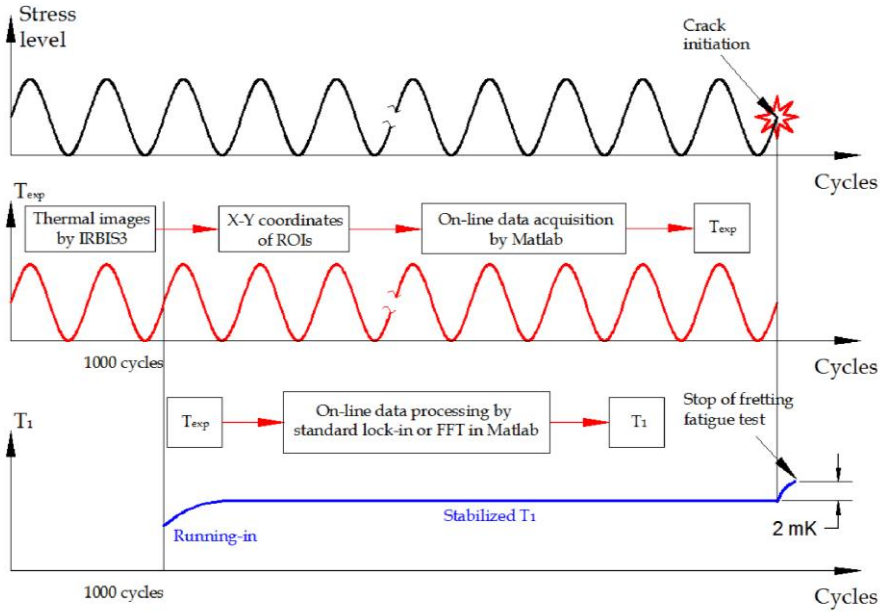

Figure 6.10 Schematic drawing showing the experimental procedure

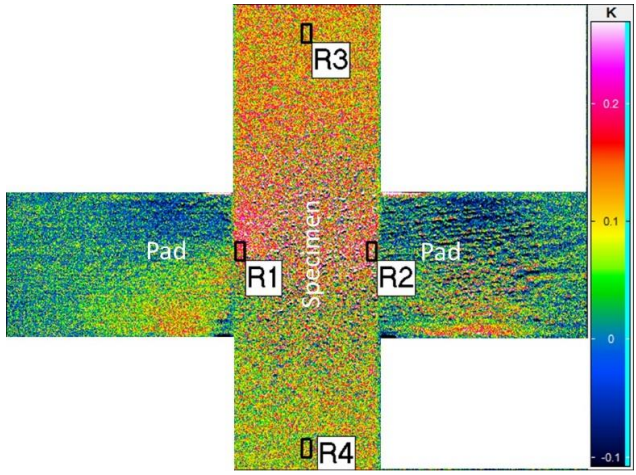

Figure 6.11 Full-frame thermal image visualized by InfraTEC CAM software IRBIS3

The smaller the region of interest, the smaller the detection threshold can be. However one risks that the locations of the regions of interest are misplaced, i.e. away from the real crack initation location, because the location of the contact area is estimated with larger uncertainty. After the first *1 000 cycles*, the coordinates of all regions of interest are inserted into a Matlab script and from then on average temperature data are recorded on-line at the maximum frame rate of *50 Hz*. The data acquisition is continuous during the entire

duration of the fretting fatigue test. The accuracy of this on-line data acquisition has been verified with the off-line data extraction for all regions of interest as discussed in Chapter 4.4.2. An excellent data matching can be observed. The thermoelastic temperature amplitude, T_1, is processed on-line with a standard lock-in algorithm or Fast Fourier Transform which allows to stop the fretting fatigue test at the moment a stabilized thermoelastic temperature amplitude, T_1, increases more than a filtered signal noise ($2\ mK$). After the test is finished, optical microscopy is performed to inspect for crack length, which is defined as the detection threshold for this thermography method.

3.1.3 Results

To evaluate the hypothesis that monitoring the thermoelastic temperature amplitude, T_1, will enable detection of crack initiation, several fretting fatigue tests are conducted (see Table 6.2). The overall experimental temperature amplitude, T_a, is also evaluated in order to confirm that the better parameter for crack detection is T_1. Figure 6.12 shows a representative evolution of the temperature amplitudes in the four regions of interest for an Al2024-T3 specimen (CI_Al202401). The data shown is simply the amplitude of the overall measured temperature, T_a, corresponding to one cycle.

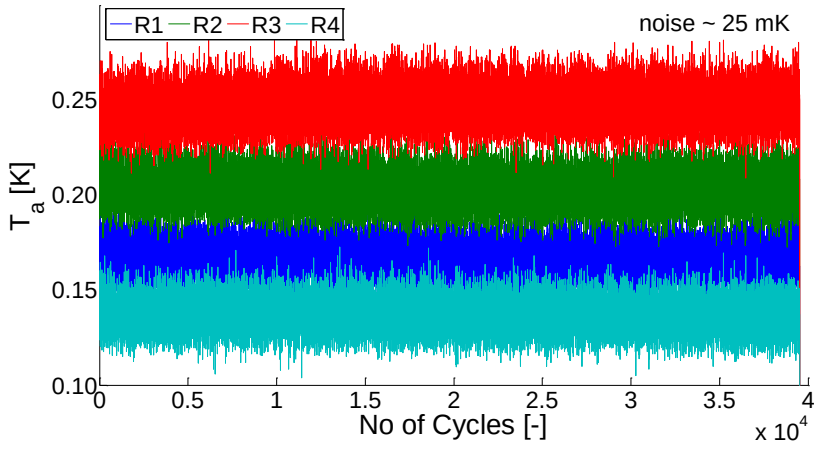

Figure 6.12 Variation of the overall temperature amplitude at the four regions of interest

This parameter is easily processed as the difference between the maximum and the minimum temperature among the *10* data points recorded in one fatigue cycle, Figure 6.2. To avoid overlapping between the four sets of data, the temperature amplitude of R_2 and R_3 have been shifted upwards with a value of *0.01* and *0.05 K*, respectively. The signal noise (*25 mK* is the nominal noise of the camera) is clearly too large to interpret the evolution of the temperature amplitude. This requires an extraction of the thermoelastic temperature amplitude, T_1, out of the overall temperature signal containing

various noises as parameter for crack initiation. To improve the nominal sensitivity of the camera (*25 mK*), four lock-in algorithms have been compared in [Krapez, 1998]. It was concluded that the least mean squares method was the most accurate one, especially at higher fatigue stress amplitude. However this method cannot be implemented on-line because it is based on an iterative solution of the best possible data fitting, which requires long calculation time. For our purpose, the most suitable algorithm is the standard lock-in algorithm (see equations (6-4) and (6-5) [Krapez, 1998]) because it allows on-line data processing and extraction of a temperature amplitude at any lock-in frequency (in this study *5 Hz*) from the overall data. Hence, this algorithm has been implemented for on-line data processing in order to reduce the signal noise.

$$S^0 = \sum_{i=1}^{N} T_{\exp}(t_i)\, p_f(t_i)$$
$$S^{90} = \sum_{i=1}^{N} T_{\exp}(t_i)\, q_f(t_i) \qquad \textbf{(6-4)}$$

$$T_1 = \sqrt{\left(S^0\right)^2 + \left(S^{90}\right)^2} \qquad \textbf{(6-5)}$$

Where N is the number of images over a certain period, t_i is the sampling interval, p_f and q_f are in-phase ($sin(2\pi ft)$) and quadrature-phase ($cos(2\pi ft)$) reference functions respectively, and f is the loading or lock-in frequency. Here, synchronisation between the signal, $T_{exp}(t)$, and the correlation or reference functions, p_f and q_f, is impossible. More details on the timing strategy of the lock-in processing can be found in Chapter 4.2.2. Therefore, it is assumed that the sampling interval is perfectly *0.02 s* from one data point to another within each correlation period since the frame rate is *50 Hz*. This allows simple digital discretization of the correlation functions. In practice, there is always a small error on the acquisition rate (*50 ± error Hz*), but with *10* data points per cycle, this error is considered to have a negligible effect on the sampling interval t_i.

By applying the standard lock-in algorithm, the overall experimental temperature is filtered to obtain only thermoelastic temperature amplitude, T_1, and the signal noise is reduced to *2 mK* for a lock-in period of *10.24 s*. As a result, a much clearer trend in the evolution of the thermoelastic temperature amplitudes can be seen in Figure 6.13. The test begins with a running-in period which then gradually evolves into a stabilization stage (horizontal line). Next, around *39 500 cycles*, the thermo-elastic temperature amplitude at the contact regions of interest R_1 and R_2 shows an increase higher than a predefined threshold of *2 mK* corresponding to the filtered signal noise.

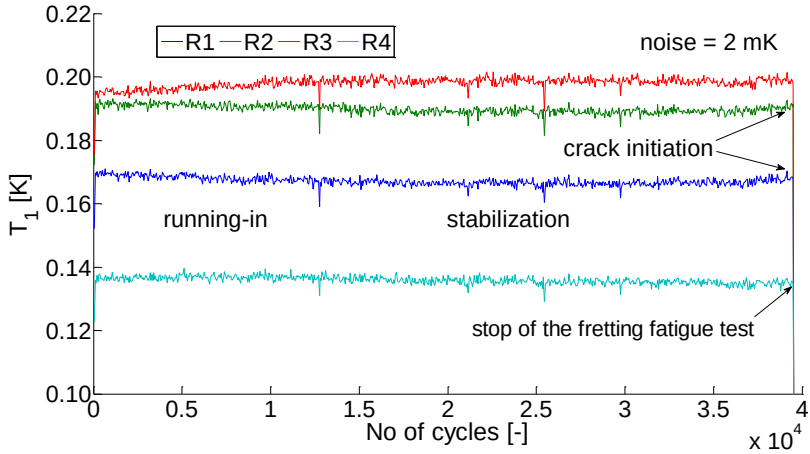

Figure 6.13. Variation of the thermo-elastic temperature amplitude at the four regions of interest

3.1.3.1 Statistical analysis

In order to verify the credibility of this criterion, the data evolution just before the end of the test is evaluated in more detail off-line. A portion of the thermoelastic temperature amplitude data at R_1 and R_2 (from *17 000* to *39 500 cycles*) is analyzed by the commercial statistical software *SPSS* version 21 (see Figure 6.14 and Figure 6.15). From Figure 6.14, a constant thermoelastic temperature amplitude is observed until N_0 = *36 500 cycles*, which is covered by Gaussian noise. The best fitting model is therefore $T_1(R_1) = 0.166$ ($N_0 \in [17\,000, 36\,500]$) , the mean value of the sample. At the turning point, N_0 = *36 500 cycles*, the inclination of the strip of data requires an adapted linear model. Parameter β_0 as well as parameter β_1 of the regression model (equation (6-6)), are significantly different from *0* (*p-value* < *0.0001* for *95%* confidence interval). Hence, it can be said that the model $T_1(R_1) = 0.144 + 6.023*10^{-7}\ N_0$ ($N_0 \in [36\,500, 39\,500]$) is a valid estimation of the linear increase of the temperature starting from N_0 = *36 500 cycles*. With the same regression analysis for the region of interest R_2 (Figure 6.15), a constant thermo-elastic temperature $T_1(R_2) = 0.18902$ ($N_0 \in [17000, 36500]$) and the inclination $T_1(R_2) = 0.167 + 6.053*10^{-7}\ N_0$ ($N_0 \in [36\,500, 39\,500]$) are found. From this statistical analysis, the criterion to stop the test when the average thermoelastic temperature amplitude is increased above the filtered signal noise (*2 mK*) is good enough but a bit conservative since there is a rise of the thermoelastic temperature amplitude from N_0 = *36 500 cycles* onwards. However, this statistical analysis cannot be implemented on-line, and the test has to be stopped based on the operator skills.

$$T_1(R_1) = \beta_0 + \beta_1 N_0 \qquad \textbf{(6-6)}$$

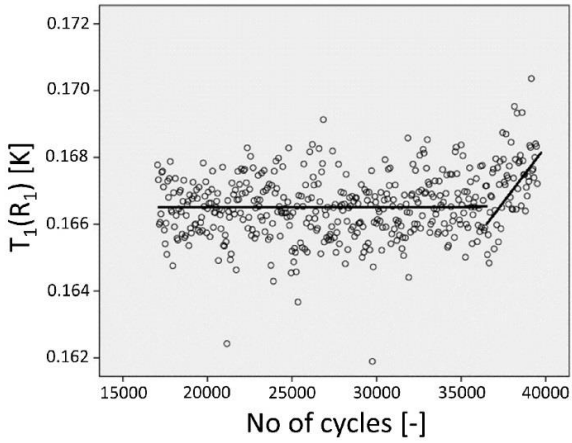

Figure 6.14 Scatter plot with regression lines for temperature $T_1(R_1)$ at $N_0 \in$ *[17 000, 39 500] cycles*

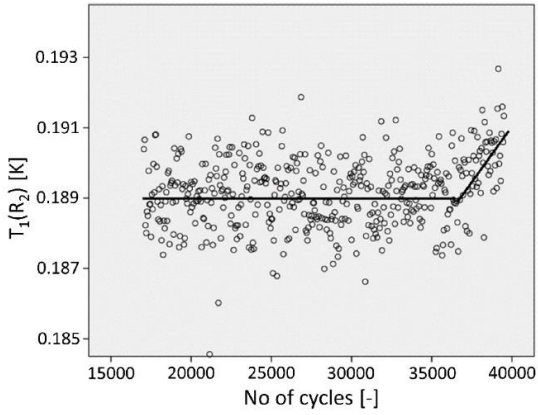

Figure 6.15 Scatter plot with regression lines for temperature $T_1(R_2)$ at $N_0 \in$ *[17 000, 39 500] cycles*

3.1.3.2 Optical microscopy

It is hypothesized that the thermo-elastic temperature amplitude increase is due to crack initiation and short crack propagation. The fretting fatigue test was stopped immediately at *39 500 cycles* and the sample was inspected for cracks by optical microscopy (see Figure 6.16). Hereto the sample was ground from the surface towards the center of the line contact in steps of *500 µm*. After each grinding step, the sample surface is polished and crack length is measured by a microscope. The maximum crack length along this grinding direction is taken as the threshold crack size (the minimum crack length that can be detected) for this thermography technique. A maximum crack length

of *400 μm* is found at region R_1 while a maximum crack length of *130 μm* is found at region R_2.

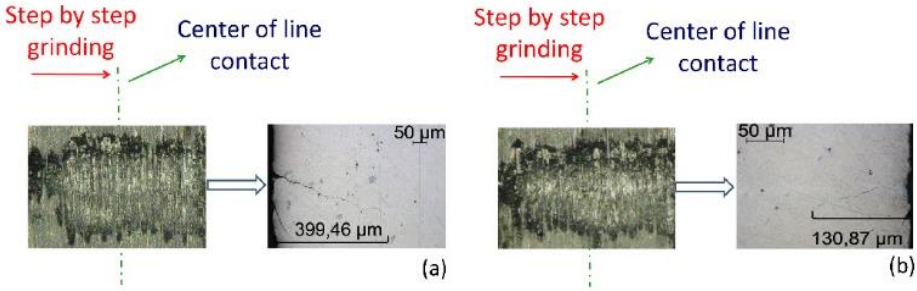

Figure 6.16. Off-line optical microscopy a) at the left contact and b) at the right contact

The results of all other tests performed are summarized in Table 6.3. In all tests there is a thermal indication of crack presence at the right contact, i.e an increase of T_1. The detected crack length in the closed fretting fatigue contact is in the range of *130-220 μm*. At the left contact, where the maximum crack lengths along the grinding direction are below *100 μm* (for all tests except one), there is no thermal indication of crack presence as can be seen for example in Figure 6.17 for the test *CI_S235JRC02*.

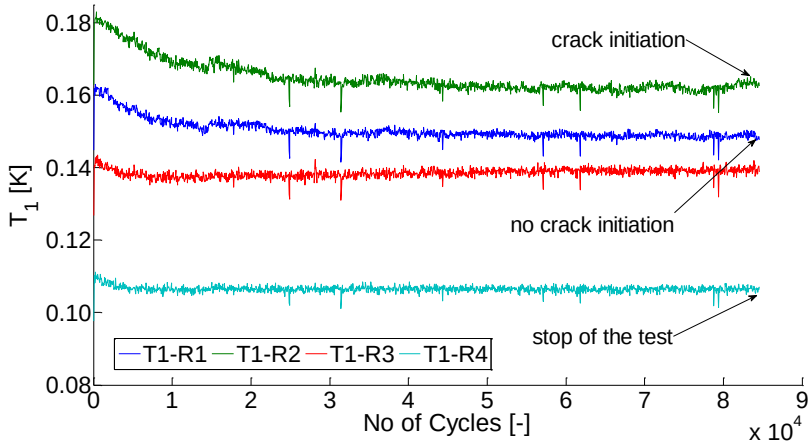

Figure 6.17 Variation of the thermoelastic temperature amplitude when there is a crack at R_2 but not at R_1 (CI_S235JRC02)

The standard lock-in algorithm is actually a discrete Fourier transform (DFT) at a specific frequency. In this sense, a Fast Fourier Transform (FFT) could also be performed for noise reduction since it allows DFTs for various frequency ranges. Selecting the maximum DFT will give the value of the temperature amplitude at the first harmonic frequency. The FFT necessitates

a number of data samples equal to 2^M, where M is an integer, but this is not at all an issue for the reported application. The two processing techniques have been evaluated and it was evidenced that they result in comparable results. However, the FFT-based processing would be more robust in the case that the testing machine does not operate at a proper controlled and constant frequency and does not require that the data acquisition is perfectly *50 Hz*. Picking the maximum temperature amplitude from the FFT frequency spectrum does not require to know a sampling interval nor the frequency value where the signal amplitude is maximum.

Table 6.3 Summary of fretting fatigue results

Test no.	Crack length [µm]		N_i [Cycles]
	At left contact	At right contact	
CI_Al202401	**400**	42 962	42 962
CI_Al202402	97	66 134	66 134
CI_Al202403	99	70 044	70 044
CI _S235JRC01	0	58 548	58 548
CI _S235JRC02	60	89 284	89 284

3.1.4 Proportion of crack initiation and total lifetime

Once the experimental methodology to detect crack initiation was developed and a detection threshold was defined (*130-220 µm*), another series of fretting fatigue tests (see Table 6.4) until final rupture of the specimen have been performed. These tests allow to check which portion of lifetime, crack initiation or crack propagation, dominates for the two materials subjected to fretting fatigue. To accelerate the tests, the loading frequency is increased from *5 Hz* to *10 Hz* so that the number of temperature samples per cycle is reduced to *5* points since the maximum data acquisition rate equals *50 Hz*. Figure 6.18 illustrates a representative evolution of the thermoelastic temperature amplitude. Similar to previous series of tests, three stages are observed in the temperature variation: running-in, stabilization and crack propagation until final rupture. Tests are not stopped in this series but continued until final rupture of the specimen; N_f = *696 306 cycles* for the illustrated test. From Figure 6.18, one can determine the lifetime of crack initiation, N_i, as the moment when the stabilized T_1 at region R_2 increases above the filtered signal noise, which is around *407 000 cycles*. The region R_2 is selected since from this contact side the dominant crack at failure occurred. On the other hand, T_1 at the region R_1 decreases after the stabilization. The drop can be due to the presence of a crack as well, but this crack might have initiated close to the front surface where the surface temperature of the specimen is measured. A surface crack will cause a void in the region of interest and therefore a drop in the thermoelastic temperature amplitude.

Anyhow, the dominant crack is at the region R_2 and not at R_1 in this test. All data N_i and N_f from the other tests are collected and summarized in Table 6.4.

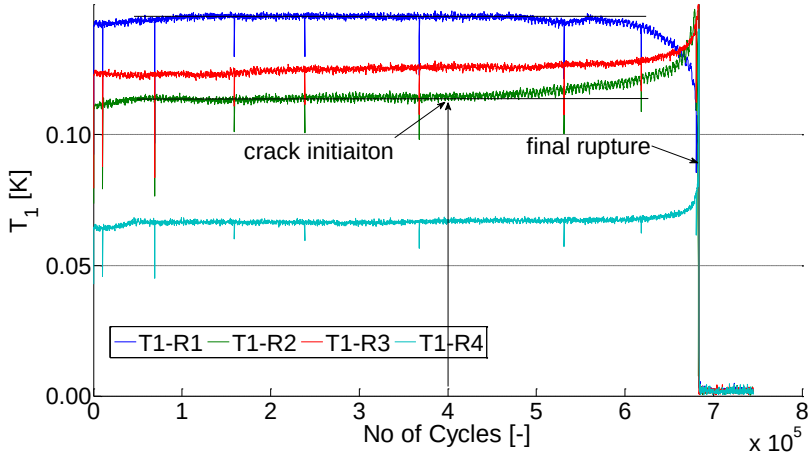

Figure 6.18 Variation of thermo-elastic temperature amplitude T_1 of the four regions of interest for the complete test (*FF_Al202404*)

Table 6.4 Proportions of crack initiation lifetime to total lifetime

Test no.	σ_{max} [MPa]	f [Hz]	P [kN]	Q_{max}/P [-]	N_i [Cycles]	N_f [Cycles]	N_i/N_f [%]
FF_Al202401	160	10	1	0.47	81 000	137 456	**58.9**
FF_Al202402	140	10	1	0.4	200 000	336 886	**59.4**
FF_Al202403	140	10	1	0.4	175 000	313 951	**55.7**
FF_Al202404	120	10	1	0.36	407 000	696 306	**58.5**
FF_S235JRC01	400	10	1	0.6	95 000	150 671	**63.1**
FF_S235JRC02	360	10	1	0.45	155 000	269 710	**57.5**
FF_S235JRC03	360	10	1	0.45	175 000	266 160	**65.8**

From these results, it can be concluded that the proportion of crack initiation lifetime to total lifetime is around 60%, which is similar to the findings of [Hojjati-talemi et al., 2014]. [Szolwinski & Farris, 1998] reported that this proportion is around 80% but their defined crack length for the initiation lifetime was *1 mm* while in this work an initiated crack could be detected with a length of a few hundred microns. The difference in crack initiation length most probably causes this discrepancy. This experimental finding is also confirmed by analytical solutions of [Hills, Nowell & O'Connor, 1988] which state that the crack initiation stage dominates in fretting fatigue. In

contrast, [Endo & Goto, 1976] found that most of fretting fatigue lifetime is taken by crack propagation. Even though a number of researchers, including this study, have confirmed that the crack initiation dominates, it may not be sufficient yet to draw a general conclusion. [Hills, Nowell & O'Connor, 1988; Hojjati-talemi et al., 2014; Szolwinski & Farris, 1998] and the author of this dissertation, all use a single actuator fretting fatigue test rig where the tangential force is induced by the elongation of the specimen. This practice requires a high fatigue load to get enough tangential force; therefore it is logical that crack initiation dominates as suggested by another work of [Hills & Nowell, 1994]. They discussed that a combination of low and high level of fatigue load and low and high level of fretting loads have an effect on this proportion. However, because of the limit of the single actuator test rig, other combinations of fatigue and fretting loads, particularly for low fatigue load and high fretting loads, cannot be investigated.

3.2 Elliptical contact

3.2.1 Introduction

The coupon scale fretting fatigue tests in this work are categorized as idealised fretting fatigue tests, Chapter 3, whose intention is to develop a general understanding of the fretting fatigue phenomenon based on a simple and well-defined contact and then to apply the knowledge to more complex contact problems as encountered in real engineering problems. The separation of the crack initiation and the crack propagation lifetime has been hardly achieved in experiments even for a simple and well-defined contact, most commonly a line contact. [Szolwinski et al., 2000] used their multiaxial SWT model validated by the coupon scale test to predict crack initiation lifetime of a medium scale test of riveted lab joints. The experimental method to define crack initiation lifetime was based on the registered total lifetime and subtraction of the crack propagation lifetime obtained from analytical solutions, section 2.2. With the data developed in this dissertation (sections 3.1 and 3.1.4), numerical and analytical models based on multiaxial fatigue criteria and other methods such as damage mechanics could possibly be better validated. However, whether the validated models are valid for real engineering problems remains doubtful because of the size effect. The size effect suggests that a stress-based approach alone cannot be used to study fretting fatigue problems (see Chapter 2.2). This is a reason why [Mugadu, Hills & Nowell, 2002] argued that data from a typical line contact could not be used to understand a more complex contact type in real engineering problems.

Researchers have been working on explaining this size effect. [Fouvry, Kapsa & Vincent, 2000] incorporated the size effect into multiaxial fatigue models by averaging the multiaxial fatigue parameters over an area instead of a single critical point. [Araújo & Nowell, 2002] adopted the methodology and implemented it into the criteria of SWT (Smith-Watson-Topper) and FS

(Fatemi-Socie), and found that these approaches allow to explain the size effect but the challenge was the selection of the dimension of that averaging area. [Fouvry & Kubiak, 2009] chose the dimension of this area by a calibration based on one plain fretting test. Still, the error between the model compared to fretting fatigue experiments was around *10 %*. Later, [Fouvry, Gallien & Berthel, 2014] realized that the area to be averaged was not constant but dependent on the stress gradient, and its correlation needed to be determined. Hence, the error between the model and the experimental result was reduced to less than *5 %*. In this sense, one could conclude that the size effect is no longer a concern by an appropriate selection of the area to average the multiaxial damage parameter or in other words that the stress based approach alone is enough to correlate laboratory tests to real engineering problems. However, the averaging method was only investigated for a line contact. To ensure that it can be extended to a more complex contact like in real engineering problems, an elliptical contact is used for the determination of crack initiation data with the well-developed experimental methodology of section 3.1. In addition, an elliptical contact intends to open the contact a little bit for the infrared camera. So, the detection threshold of the crack length is expected to be improved.

3.2.2 Test conditions and materials

Several fretting fatigue tests with different levels of maximum fatigue load are performed and monitored by the infrared camera positioned at a distance of *200 mm* from the specimen surface. The specimen and the pads are designed to have an elliptical contact at the right hand side and a line contact at the left hand side, Figure 6.19. This design should ensure that failure occurs at the contact of interest, i.e. the elliptical contact and that its sliding regime is under partial slip and the overall loading level is within the elastic range.

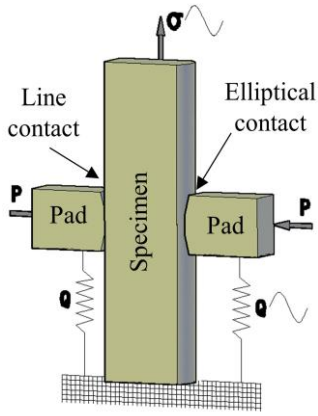

Figure 6.19 Schematic drawing of fretting fatigue tests with line contact at the left hand side and elliptical contact at the right hand side

To avoid failure from the opposite contact side, the pad radius at that side is designed to be as small as possible ($R_{pad\_R1} = 10\ mm$) . The size effect due to this difference in reduce is expected shift the total lifetime with some orders of magnitude. Also, the contact at this side should not allow any macroscopic slipping in order to avoid unbalance of the tangential forces between the left and right side of the compliant springs. Plasticity at this contact is allowed since it is not the contact of interest. The geometries and dimensions of the specimen and the pads are shown in Figure 6.20. The materials and their strengths are given in Table 6.5; their material certificates can be found in Appendix C. The sliding regime under fretting fatigue is determined by the same methodology as for the previous contact type, Figure 6.21.

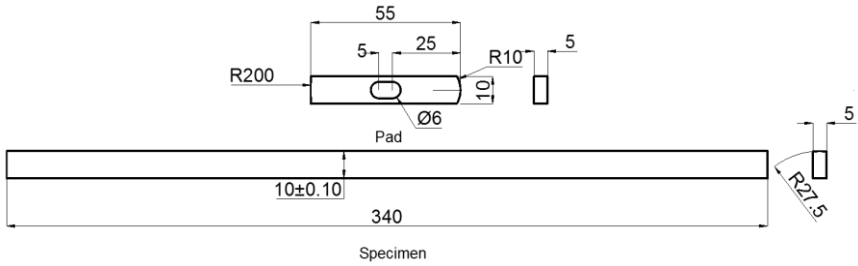

Figure 6.20 Dimensions of the samples

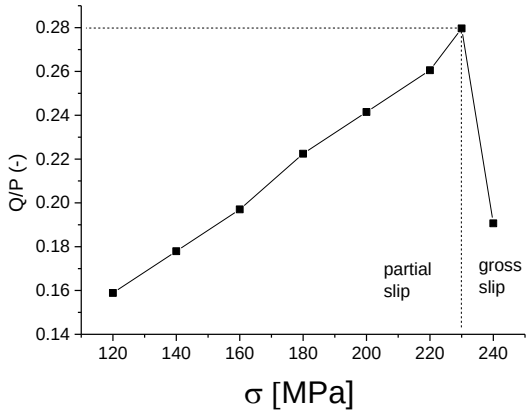

Figure 6.21 Sliding regimes in fretting of elliptical contact

Table 6.5 Material strength properties

Materials	Young's Modulus [GPa]	σ_y [MPa]	σ_{ult}[MPa]
Specimen (Al2024-T3511)	73	450	570
Pads (Al2024-T3)	73	383	506

The representative friction coefficient under partial slip can be estimated from the *Q/P* ratio at the transition between the partial slip and gross slip regimes. For this contact type and materials, it is estimated to be *0.28*. By keeping the normal load as in the previous contact type, $P = 1\ kN$, the maximum contact pressure is $p_0 = 420\ MPa$. This calculation is based on Appendix D or a webpage [Elliptical Hertzian contact, 2017]. Loading frequency is *5 Hz* to have *10* samples of temperature data per cycle as the maximum on-line data acquisition rate is *50 Hz*. The fatigue ratio is $R = 0.001$ while the ratio of the tangential force is *-1*. Detailed loading conditions of all fretting fatigue tests are given in Table 6.6.

Table 6.6 Test conditions of fretting fatigue with elliptical contact

Test no.	σ_{max} [MPa]	f [Hz]	R (σ_{min} /σ_{max}) [-]	P [kN]	Q_{max} /P [-]	$R_{specimen}$ [mm]	R_{pad} [mm]	p_0 MPa
CI_CoC01	200	5	0.001	1	0.22	27.5	200	420
CI_CoC02	220	5	0.001	1	0.24	27.5	200	420
CI_CoC03	180	5	0.001	1	0.20	27.5	200	420
CI_CoC04	220	5	0.001	1	0.24	27.5	200	420

3.2.3 Experimental procedure

The same experimental procedure as in the fretting fatigue tests with line contact is utilized. Full-frame thermal images (*640* x *512 pixels*), one of which is shown in Figure 6.22, are recorded via InfraTEC CAM software IRBIS3, for the first *1000 cycles* only.

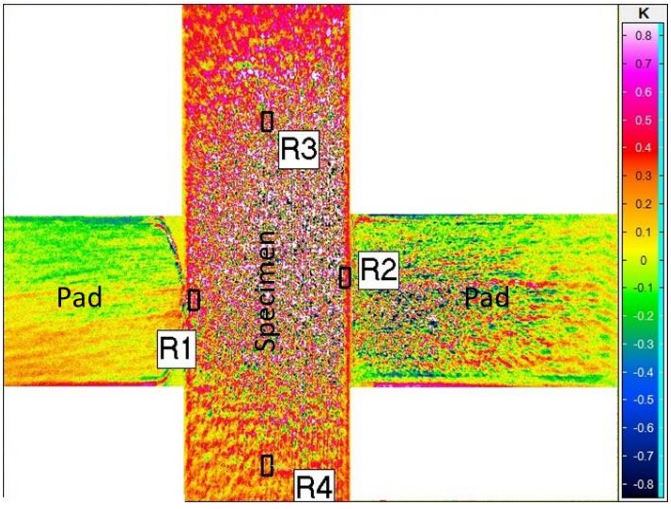

Figure 6.22 Thermal image with four ROIs for a fretting fatigue test with elliptical contact at the right hand side

Four regions of interest are selected. Dimensions of all regions of interest are *10* by *20* pixels. For this contact type, the R_2 y-position is set *2 mm* above R_1 since the trailing edge (crack location) of the elliptical contact is higher than this of the line contact at the left hand side. After the first *1000 cycles*, the coordinates of all regions of interest are inserted into a Matlab script and from then on average temperature data are recorded on-line at the maximum frame rate of *50 Hz*. The data acquisition is continuous during the entire duration of the fretting fatigue tests. The thermoelastic temparature amplitude, T_1, is processed on-line with a standard lock-in algorithm or Fast Fourier Transform which allows to stop the fretting fatigue tests at the moment a stabilized (horizontal) thermoelastic temperature amplitude, T_1, has increased more than the filtered signal noise (*2 mK*). After a test is finished, optical microscopy is performed to inspect for the crack length which is defined as the detection threshold for this new contact type.

3.2.4 Results

Before discussing the results, a feature of failure due to fretting fatigue at an elliptical contact, Figure 6.23, is introduced based on observations from a fretting fatigue test until final rupture of the specimen. The wear scar of this contact type is elliptical since the radii of both cylinders are not identical.

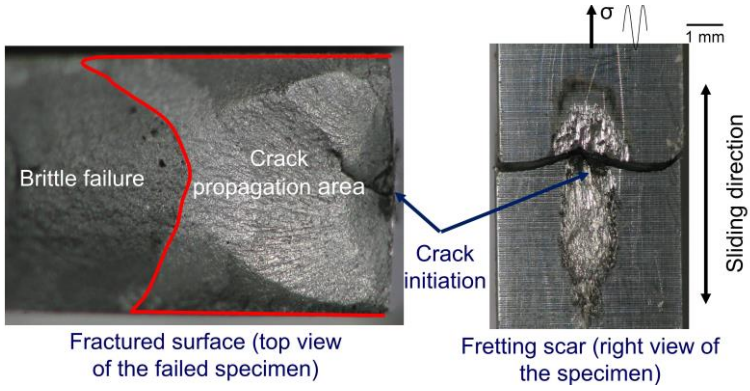

Figure 6.23 Features of failure due to fretting fatigue for a perpendicular elliptical contact

The difference in contact radii results in a less straightforward analytical contact solution for contact pressure but cannot be avoided to facilitate the machining of the specimen and ensure that the maximum contact pressure does not exceed the yield strength of the specimen. The semi-axes of the elliptical scar can be determined, following Appendix D or [Elliptical Hertzian contact, 2017]. Multiple cracks initiate from the trailing edge within the contact area. This location of crack initiation was also observed for a specimen with line contact. These small cracks merge together and grow inwards the specimen on a plane perpendicular to the fatigue load. Figure 6.24 shows a representative evolution of the thermoelastic temperature at the

four regions of intrest. The test begins with a running-in period which then gradually evolves into a stabilization stage (horizontal line) around *15 000 cycles*. Next, around *46 580 cycles*, the thermoelastic temperature amplitude at the contact region of interest R_2 shows an increase higher than a predefined threshold of *2 mK* corresponding to the filtered signal noise. The test is immediately stopped, and the sample is inspected by optical microscopy.

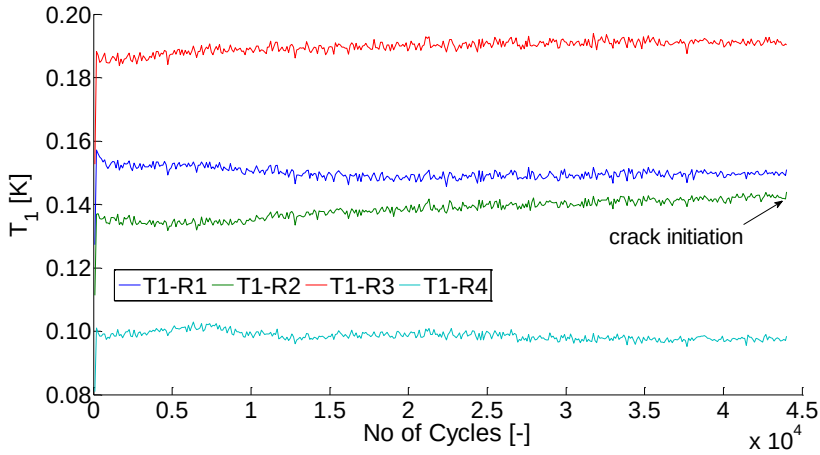

Figure 6.24 Representative evolution of thermoelastic temperature amplitude at the four regions of interest

For this contact type, the sample was ground from the front surface up to the centre of the specimen where the fretting scar occurs. This scar does not spread over the entire thickness of the specimen as was the case for the worn surface of the line contact. Then, the surface is polished and inspected for cracks by optical microscopy. The surface is then ground for two more steps each of which is *500 µm*. At each step, the surface is polished and inspected for crack length. The maximum crack length along this grinding direction is defined as the detection threshold. As a result, a maximum crack length of *221 µm* is found at the elliptical contact of interest, R_2, while no crack is found at the opposite contact, R_1, Figure 6.25. Results for other tests are summarized in Table 6.7. The maximum crack lengths detected are around *200 µm* except for the first test, *FF_CoC01*. For that test the maximum crack length was found to be *580 µm* as the region of interest R_2 was misplaced with respect to the location of the crack. In this test, R_2 was placed at the same horizontal level as R_1, but the trailing edge (crack location) at R_2 is a bit higher than that at R_1 because of its elliptical contact.

Even though the contact region of this configuration is partially accessible by the infrared camera, the detection threshold is not improved. The detected crack length is around *200* µm. One reason is that the crack width is smaller than for a line contact configuration where the crack is spread across the entire specimen thickness. These results can however be used to further validate analytical and numerical models of crack initiation.

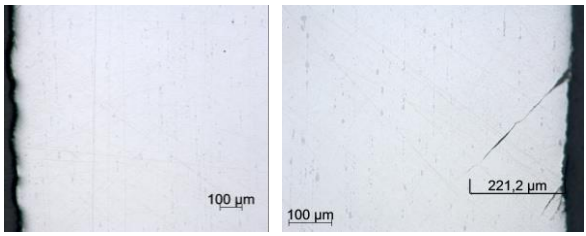

Figure 6.25 Optical microscopy for crack inspection at the left contact and the right contact

Table 6.7 Summary of results of fretting fatigue tests with elliptical contact

Test no	Maximum crack length (µm)	Cycles to crack initiation [cycles]
FF_CoC01	580	110 975
FF_CoC02	221	46 580
FF_CoC03	207	135 515
FF_CoC04	208	54 702

4 Limitations of the thermography method

4.1 Room temperature effect

So far, mainly positive features of infrared thermography have been mentioned. The temporal resolution is excellent; at room temperature it is *25 mK* and can be reduced to *2 mK* by signal processing. Such a high sensitivity allowed to detect micro-cracks in fretting fatigue tests for two different materials and two different contact types. In contrast, such a high sensitivity is also a drawback of the method. Lots of noise sources such as light intensity, room temperature, and any kind of thermal disturbance, are included in the measurement. These noises can of course be filtered by signal processing methods such as lock-in or FFT. A particular noise is the room temperature. Normally, this effect can be easily filtered by the lock-in processing since it is mostly a *D.C.* component. Figure 6.26 illustrates the influence of the room temperature on the thermoelastic temperature amplitude T_1 for the region of interest R_1. The room temperature is measured by a separate thermocouple mounted on the fretting fatigue test rig and is shown to be disrupted at *125 000 cycles* by a sharp increase of *5* ^{o}*C*. Clearly, the noise of the thermocouple is larger than that of the IR camera. From the figure, it is not possible to find a stabilization stage for T_1. T_1 probably almost reaches the stabilization after the running in stage but drops sharply around *125 000 cycles*.

This phenomenon makes the detection of the crack impossible and it is a surprising effect since the room temperature should have been filtered in a way that T_1 is an extracted parameter from the main signal. However, if the displacement of the cross-head of the ESH machine is analysed (only the minimum displacement within a cycle is shown), it can be observed that the displacement - which should be stable when the fatigue force is controlled - follows the same trend as the room temperature variation. The reason behind this fact is not fully understood yet but a possible reason is that the room temperature in this case is not just a noise factor but that it may change physical parameters of the test such as the friction coefficient or the contact point between the pads and the specimen. Therefore, it is recommended that the developed thermography technique is performed in a controlled room temperature or at least where it only smoothly changes.

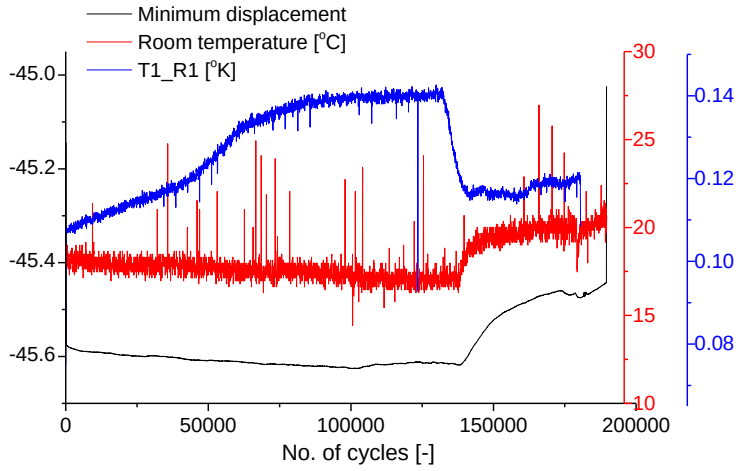

Figure 6.26 Influence of room temperature

4.2 Second harmonic T_2 as parameter for on-line crack detection

For on-line detection of fretting fatigue crack initiation, the first harmonic temperature amplitude, T_1, has been shown to be an effective parameter. A few hundred microns of crack length could be detected. In addition to that, the second harmonic temperature amplitude T_2, can be a potential parameter for crack detection. T_2 accounts for plasticity so the occurrence of cracks will surely lead to an increase of this parameter, but to extract T_2 from the overall experimental data is somewhat more challenging. Firstly, the magnitude of T_2 is almost at the same level as the signal noise, i.e. a few *mK's*. Secondly, if the FFT algorithm is used to check the evolution of T_2 on-line, it requires a longer calculation time since it first needs to find T_1 (the maximum of peak signal amplitudes) and its corresponding frequency. Then it requires an

extrapolation to find the second harmonic frequency from the first harmonic frequency and finally T_2 can be obtained. Lastly, if the standard lock-in algorithm is used to find T_2, the frequency of the correlation functions (*sine* and *cosine*) is not anymore the same as the loading frequency but twice that value. This problem requires a synchronization between the two sampling rates. Otherwise, like the FFT algorithm, the lock-in correlation process needs to be performed off-line.

5 Summary and conclusions

Detection of fretting fatigue crack initiation is attempted by analysing both *D.C.* and *A.C.* parameters of the thermographic method. The *D.C.* parameter is basically related to crack-induced plasticity at the maximum fatigue stress. Off-line data processing of the *D.C.* parameter allows to detect a crack around *1 mm* in depth while the *A.C.* parameter could allow detection of a smaller crack. The *A.C.* parameter is the thermoelastic temperature amplitude, T_1, rather than the overall experimental temperature amplitude, T_a, for noises reduction. A reason that the *A.C.* parameter is more sensitive to crack initiation than the *D.C.* parameter is probably the fact that a heat dispatch (*D.C.* component) produced by the plasticity from a subsurface crack needs to be diffused to the front surface to become detectable, whilst the thermoelastic effect (*A.C.* component) caused by a stress concentration is detectable even when the crack is in the subsurface. Therefore, the *A.C.* parameter has been selected for on-line detection. Two algorithms, standard lock-in and FFT, were used to extract the first harmonic T_1 from the overall experimental temperature. Synchronization between the loading frequency and the data acquisition rate of the IR camera is not possible so that an assumption of a perfectly equal sampling interval was made.

Two materials and two contact types were used for the fretting fatigue tests. The evolution of the first harmonic of all tests is shown to consist of three stages: running-in, stabilization, and crack initiation. The stabilization of T_1 is defined to be a horizontal line and at the moment this value of T_1 increases above the filtered signal to noise ratio, the fretting fatigue test is stopped immediately to inspect for cracks by optical microscopy. A statistical analysis by SPSS 21 is performed to check the credibility of this increase as indicator for crack initiation and shows that it is slightly conservative to wait until the stabilized T_1 is above the noise level, but the statistical analysis cannot be performed on-line and the test needs to be stopped by the operator based upon his observations. The optical inspection reveals that the detection threshold for both materials and contact types is around a few hundred micrometres. Once the methodology was developed, fretting fatigue tests until complete rupture were performed on the two materials with line contact to determine if either crack initiation or either propagation determine total lifetime. The results show that the crack initiation takes around 60% on average which is confirmed by literature sources using a similar single

actuator test rig with adjustable stiffness of the compliant springs. This ratio seems to be independent of fatigue load. Other combinations of fatigue load and fretting load need to be experimentally analysed to verify this conclusion. However, the UGent test set-up currently does not allow other combinations, and especially not very low fatigue loads combined with high fretting loads.

The developed infrared thermography methodology is able to detect a micro-crack (*130-220 μm*) hidden in the closed contact for both materials and contact types during fretting fatigue. It also allows to separate crack initiation from crack propagation lifetime. The most important progress beyond the state of the art is that the developed methodology can be applied on-line. Continuous measurement for long test durations such as fretting fatigue is made feasible. The methodology looks promising to detect crack initiation in specimens subjected to any harmonic loading if the crack location can be accurately estimated prior to the tests. The developed experimental results could be used to better validate analytical/numerical models and could be useful to conclude on the size effect in fretting fatigue since it is a very important challenge whether the correlation of the coupon scale test results to real engineering problems is valid or not. However, attention needs to be paid with respect to the effect of the room temperature on the physical process of fretting fatigue. On the other hand, further improvements are possible if the T_2 component could also be processed on-line.

References

Araújo, J.A., Nowell, D. (2002) The Effect of Rapidly Varying Contact Stress Fields on Fretting Fatigue. *International Journal of Fatigue*, 24, 763–75.

Berthel, B., Moustafa, A.-R., Charkaluk, E., Fouvry, S. (2014) Crack Nucleation Threshold under Fretting Loading by a Thermal Method. *Tribology International*, 76, 35–44.

Bremond, P., Potet, P. (2001) Lock-In Thermography: A Tool to Analyse and Locate Thermo-Mechanical Mechanisms in Materials and Structures. In *SPIE*. pp. 560–6.

Chhith, S., De Waele, W., De Baets, P. (2015) Detection of Fretting Fatigue Crack Initiation by Thermography. In SZABÓ, I. and KALÁCSKA, G. (eds.), *Synergy 2015 International Conference*. Szent István University. Faculty of Mechanical Engineering, Gödöllő, Hungary, pp. 36–42.

Colombo, C., Vergani, L., Burman, M. (2012) Static and Fatigue Characterisation of New Basalt Fibre Reinforced Composites. *Composite Structures*, 94, 1165–74.

Dowling, N.E. (1979) Notched Member Fatigue Life Predictions Combining Crack Initiation and Propagation, 2, 129–38.

Elliptical Hertzian Contact (2017) *Http://www.tribology-abc.com*.

Endo, K., Goto, H. (1976) Initiation and Propagation of Fretting Fatigue Cracks. *Wear*, 38, 311–24.

Fargione, G., Geraci, A., Rosa, G. La, Risitano, A., Doria, V.A. (2002) Rapid Determination of the Fatigue Curve by the Thermographic Method. *International Journal of Fatigue*, 24, 11–9.

Fellows, L.J., Nowell, D., Hills, D.A. (1997) On the Initiation of Fretting Fatigue Cracks. *Wear*, 205, 120–9.

Fouvry, S., Gallien, H., Berthel, B. (2014) From Uni- to Multi-Axial Fretting-Fatigue Crack Nucleation : Development of a Stress-Gradient-Dependent Critical Distance Approach. *International Journal of Fatigue*, 62, 194–209.

Fouvry, S., Kapsa, P., Vincent, L. (2000) A Multiaxial Analysis of Fretting Contact Taking into Account the Size Effect. In *Fretting Fatigue: Current Technology and Practices, ASTM STP 1367, D. W. Hoeppner, V. Chandraskaran, and C. B. Elliot*. ASTM, West Conshohocken, PA.

Fouvry, S., Kubiak, K. (2009) Introduction of a Fretting-Fatigue Mapping Concept: Development of a Dual Crack Nucleation – Crack Propagation Approach to Formalize Fretting-Fatigue Damage. *International Journal of Fatigue*, 31, 250–62.

Hills, D.A., Nowell, D. (1994) *Mechanics of Fretting Fatigue*. Kluiwer Academic Publishers, Dordrecht.

Hills, D.A., Nowell, D., O'Connor, J.J. (1988) On the Mechanics of Fretting Fatigue. *Wear*, 125, 129–46.

Hojjati-talemi, R., Wahab, M.A., De Pauw, J., De Baets, P. (2014) Prediction of Fretting Fatigue Crack Initiation and Propagation Lifetime for Cylindrical Contact Configuration. *Tribology International*, 76, 73–91.

Johnson, K.L. (1985) *Contact Mechanics*. Cambridge University Press.

Kondo, Y., Sakae, C., Kubota, M., Yanagihara, K. (2005) Non-Propagating Crack Behaviour at Giga-Cycle Fretting Fatigue Limit. *Fatigue Fracture of Engineering Materials and Structures*, 28, 501–6.

Krapez, J.. (1998) Compared Performances of Four Algorithms Used for Modulation Thermography. In *Quantitative Infrared Thermography 4*. pp. 148–53.

Krapez, J.C., Pacou, D., Gardette, G. (2000) Lock-in Thermography and Fatigue Limit of Metals. In *Quantitative Infrared Thermography 5*. pp. 277–82.

Luong, M.P. (1998) Fatigue Limit Evaluation of Metals Using an Infrared Thermographic Technique. *Mechanics of Materials*, 28, 155–63.

Lykins, C.D., Mall, S., Jain, V.K. (2001) Combined Experimental – Numerical Investigation of Fretting Fatigue Crack Initiation. *International Journal of Fatigue*, 23, 703–11.

Meriaux, J., Fouvry, S., Kubiak, K.J., Deyber, S. (2010) Characterization of Crack Nucleation in TA6V under Fretting–fatigue Loading Using the Potential Drop Technique. *International Journal of Fatigue*, 32, 1658–68.

Micone, N., De Waele, W. (2016) On the Application of Infrared Thermography and Potential Drop for the Accelerated Determination of an S-N Curve. *Experimental Mechanics*, 57, 143–53.

Montesano, J., Fawaz, Z., Bougherara, H. (2013) Use of Infrared Thermography to Investigate the Fatigue Behavior of a Carbon Fiber Reinforced Polymer Composite. *Composite Structures*, 97, 76–83.

Mugadu, A., Hills, D.A., Nowell, D. (2002) Modifications to a Fretting-Fatigue Testing Apparatus Based upon an Analysis of Contact Stresses at Complete and Nearly Complete Contacts. *Wear*, 252, 475–83.

Ranc, N., Wagner, D., Paris, P.C. (2008) Study of Thermal Effects Associated with Crack Propagation during Very High Cycle Fatigue Tests. *Acta Materialia*, 56, 4012–21.

Risitano, A., Risitano, G. (2010) Cumulative Damage Evaluation of Steel Using Infrared Thermography. *Theoretical and Applied Fracture*

Mechanics, 54, 82–90.

Rosa, G. La, Risitano, A. (2000) Thermographic Methodology for Rapid Determination of the Fatigue Limit of Materials and Mechanical Components. *International Journal of Fatigue*, 22, 65–73.

Schijve J (2009) *Fatigue of Structures and Materials*. Springer Science+ Business Media, B. V.

Silva, L.F.M., Gonçalves, J.P.M., Oliveira, F.M.F., de Castro, P.M.S.T. (2000) Applicability of the SPATE Technique to the Detection of Hidden Cracks. *NDT & E International*, 33, 7–13.

Socie, D.F., Morrow, J., Chen, W.C. (1979) A Procedure for Estimating the Total Fatigue Life of Notched and Cracked Members. *Engineering Fracture Mechanics*, 11, 851–9.

Szolwinski, M.P., Farris, T.N. (1996) Mechanics of Fretting Fatigue Crack Formation. *Wear*, 98, 93–107.

Szolwinski, M.P., Farris, T.N. (1998) Observation, Analysis and Prediction of Fretting Fatigue in 2024-T351 Aluminum Alloy. *Wear*, 221, 24–36.

Szolwinski, M.P., Harish, G., Farris, T.N., Sakagami, T. (1999) In-Situ Measurement of Near-Surface Fretting Contact Temperatures in an Aluminum Alloy. *Journal of Tribology-Transactions of the ASME*, 121, 11–9.

Szolwinski, M.P., Harish, G., McVeigh, P.A., Farris, T.N. (2000) Experimental Study of Fretting Crack Nucleation in Aerospace Alloys with Emphasis on Life Prediction. In Hoeppner, D.W., Chandraskaran, V. and and Elliot, C.B. (eds.), *Fretting Fatigue: Current Technology and Practices, ASTM STP 1367*. ASTM, West Conshohocken, PA, pp. 267–81.

Tomlinson, A., Patterson, A. (1997) On Determining Stress Intensity Factors for Mixed Mode Cracks from Thermoelastic Data. *Fatigue & Fracture of Engineering Materials & Structures*, 20, 217–26.

Ummenhofer, T., Medgenberg, J. (2009) On the Use of Infrared Thermography for the Analysis of Fatigue Damage Processes in Welded Joints. *International Journal of Fatigue*, 31, 130–7.

Wagner, D., Ranc, N., Bathias, C., Paris, P.C. (2009) Fatigue Crack Initiation Detection by an Infrared Thermography Method. *Fatigue & Fracture of Engineering Materials & Structures*, 12–21.

Chapter 7 Extension of the application field of the developed experimental methodologies

"In this chapter, the developed experimental methodologies for studying fretting fatigue damage and crack initiation are applied to low cycle fatigue tests of a bent sample of high strength steel. Similar to fretting fatigue, the location of crack initiation can be predicted prior to the tests. For fretting fatigue it is situated at the trailing edge of the contact area, while for fatigue of the bent sample it is along the valley of the bend root."

1 Fatigue of high strength steels

High-strength steel (HSS) grades thank their excellent mechanical properties (high strength and good toughness) to an accurate control of the very fine grain size during processing. They are also well-known for having better controlled internal impurities. HSS grades are used to replace conventional carbon steels in structural applications where weight reduction is required while maintaining the overall high performance. Lower thickness of structural components allows additional savings through a lower cost of transport and less welding operations. However, fatigue properties of these new steel grades are typically less good as compared to carbon steels, and particularly there are not many research works focusing on the effect of the forming process on the fatigue properties of components.

To evaluate the fatigue behaviour of structural components, it may not be sufficient for designers to rely on fatigue properties derived from standardized specimens. In a conventional fatigue test, different levels of stress or strains are applied to standardized samples, e.g. dog-bone or compact tension specimen, to determine fatigue properties such as fatigue strength and crack growth rate. In practice, materials are used in diverse size and shapes and subjected to more complex loadings. Once an equivalent stress or strain level in the components is determined, their fatigue behaviour can be estimated based on the results of standardized tests. However, the forming operation of components may affect their fatigue properties.

2 Motivation of the IR based experimental study

To investigate the effect of plastic forming operations on fatigue life, a simple bent specimen made of steel S700MC has been designed for a low cycle fatigue test [Talemi, Chhith & De Waele, 2017]. A punch is used to bend dog-bone shaped specimens at their centre to an angle of 90^0 (Figure 7.1). Subsequently, two such specimens are welded together to avoid eccentric loading of the load cell of the test machine, under the assumption that a perfectly symmetric cyclic force is applied to both sides of the sample. Determination of the fatigue properties of the bent sample is very challenging. In earlier work a numerical model has been developed to analyse the stress and strain at the critical location, i.e. the root of the bend, and a method to detect crack initiation based on cross-head displacement of a testing machine has been proposed. During force controlled fatigue testing of the bent specimen, the cross-head displacement is monitored to determine the crack initiation time. A criterion based on an increase of the stabilized displacement equal to *0.1 mm* (see Figure 7.2) has been suggested.

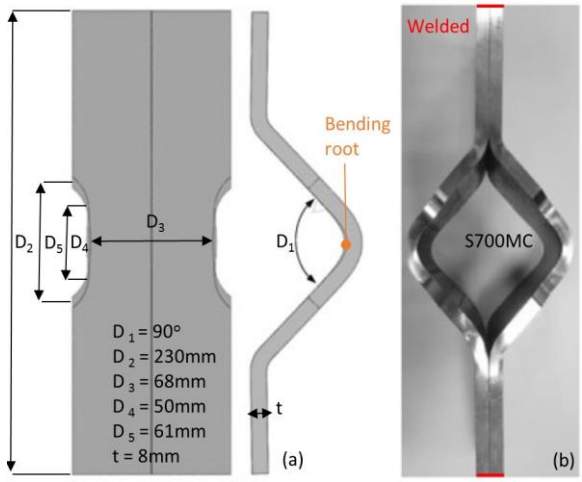

Figure 7.1 Bent specimen [Talemi, Chhith & De Waele, 2017]

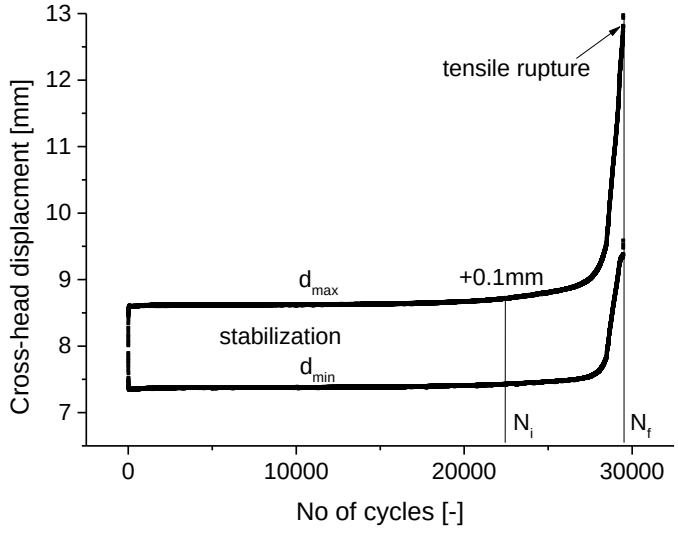

Figure 7.2 Detection of crack initiation by cross-head displacement (d_{min} and d_{max} are respectively the minimum and maximum displacements during a fatigue cycle)

The test is stopped at that value and the specimen is cross-sectioned to evaluate the presence of cracks. A crack length of approximately *600 µm* was revealed by optical microscopy. Based on this criterion, the ratio of crack initiation time to total lifetime has been calculated to be around *80 %*, i.e. the crack initiation time dominates. Hence, to improve the lifetime of the bent specimens, techniques for extension of crack initiation time have been adopted like shot peening or blasting in order to introduce residual compressive stresses. However, the threshold of *600 µm* for crack initiation is not sufficient for the HSS grade with a much smaller grain size around *50 µm*.

Therefore, an advanced test and monitoring methodology based on infrared thermography has been developed. Preliminary results suggested that the ratio of the crack initiation time to total lifetime is around *50 %* with the detection threshold to be further investigated.

Fatigue properties of materials have been shown to have a clear relation with their temperature responses; whether based on a temperature rise of the specimen or on the harmonics responses [Colombo, Vergani & Burman, 2012; Fargione et al., 2002; Luong, 1998; Micone & De Waele, 2016; Montesano, Fawaz & Bougherara, 2013; Risitano & Risitano, 2010; Rosa & Risitano, 2000]. As discussed in a previous chapter, the total temperature response under sinusoidal load can always be best fitted by equation (7-1). The first term refers to the linear drift of the mean temperature, while the first and second harmonics are linear and non-linear responses, respectively. The first harmonic temperature amplitude is quantified by the thermoelastic effect, equation (7-2), whilst the second harmonic can be linked to any fatigue damage. Particularly in this thesis, the fretting fatigue limit has been predicted by analysing the second harmonic response. An on-line micro-crack detection has been achieved, and the crack initiation and propagation times could be separated by monitoring the first harmonic response.

$$T_{\exp}(t) = T_0 + \Delta T.f.t + T_1 \sin(\omega t + \varphi_1) + T_2 \sin(2\omega t + \varphi_2) \quad \textbf{(7-1)}$$

$$T_1 = \left| -\frac{\alpha T_0}{\rho C_p}\sigma_{kk} \right| = \left| -k\sigma_{kk} \right| \quad \textbf{(7-2)}$$

The developed experimental methodologies based on temperature analysis for studying fretting fatigue damage and crack initiation are explored to investigate the fatigue properties of the bent specimens. The location of fatigue crack initiation is predicted to be along the valley of the bend root. The block loading method is applied, and the evolution of the second harmonic response is analysed using the Matlab FFT algorithm to predict the fatigue limit of the bent sample. Monitoring of the first harmonic response is used to detect on-line the crack initiation and to inspect the corresponding crack length. The separation of crack initiation time to crack propagation time is also performed by monitoring the first harmonic response in a test run until the final specimen rupture.

3 Infrared thermography based evaluation of low cycle fatigue properties of S700MC

3.1 Set-up and material

The experimental set-up for fatigue testing of bent specimen together with the infrared thermographic camera, is shown in Figure 7.3a. The bent

specimen is mounted in an ESH 100 kN testing machine which was also used for the fretting fatigue tests. The lower clamping is fixed, while the force is cyclically controlled as a sinusoidal waveform by the upper clamp. Since two specimens are welded together, the IR camera has to be installed obliquely to one of the specimen surfaces to ensure that the full width of the specimen along the valley can be visualized. The IR camera is used with a default standard calibration, a temperature range of *5-60°C* and an integration time of *1050 µs*. The camera distance is around *500 mm* from the specimen, which gives an approximate pixel size of *100 µm*. Observation of the temperature distribution on the thermal image allows to confirm the most critical region of the specimen, along the valley of the bending root (Figure 7.3b).

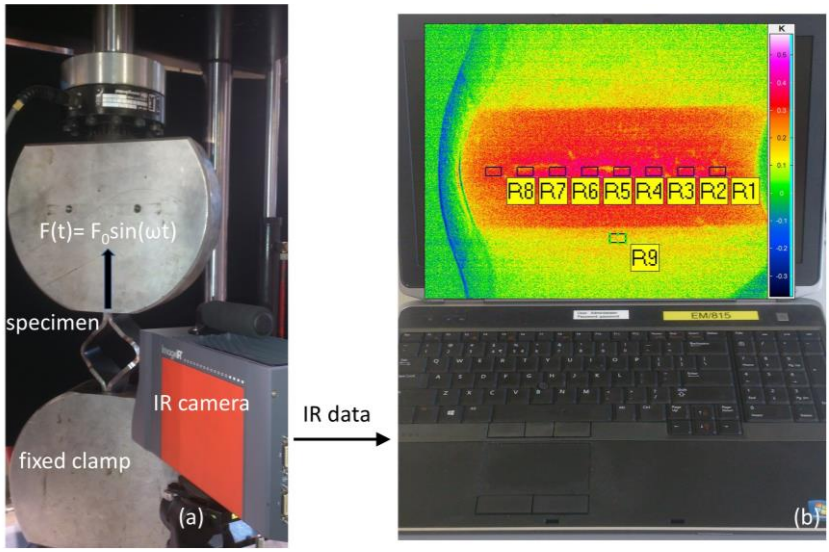

Figure 7.3 Experimental set-up for low cycle fatigue tests on bent samples

The temperature evolution is monitored for nine regions of interest. ROIs R_1-R_8 are selected along the valley and ROI R_9 is chosen outside the valley as a reference for the temperature analysis. Each ROI dimension is *10* by *20 pixels*, and they are equally spaced from each other by *40 pixels*. The material used is a high strength steel of grade *S700MC* with average yield stress and tensile strength equal to *841 MPa* and *882 MPa*, respectively and the fatigue limit of *570 MPa* at *2 10^6 cycles*.

3.2 Determination of the fatigue limit

A stepwise increased block loading scheme consisting of five load levels is applied to the bent specimen. Each load block is run with a frequency of *10 Hz*, a fatigue ratio (*R-ratio* = F_{min}/F_{max}) of *0.1* and a duration of *2 000 cycles*. The maximum force (F_{max}) and the corresponding stress levels which are obtained from [Talemi, Chhith & De Waele, 2017] of all blocks are *5 kN (110 MPa), 10 kN (200 MPa), 15 kN (325 MPa), 20 kN (400 MPa)* and *25 kN (500 MPa)*. The IR

camera captures thermal images continuously for the whole test duration at a frame rate of *100 Hz*. A total number of *100 000* thermal images are stored in the infrared laptop.

Averaged temperature data of the nine ROIs, described in the previous section, are extracted from all thermal images via the thermal CAM software of InfraTEC. These data are then analysed in the frequency domain with an FFT algorithm of the commercial software Matlab. The FFT analysis is performed for every *1 024 samples* (=2^{10}) which corresponds to *102.4 cycles* or *10.24 seconds*. After that, the frequency of the maximum temperature amplitude (the first harmonic) is determined and extrapolated to search for the second harmonic frequency. Finally, the second harmonic temperature amplitude is extracted. Figure 7.5 and Figure 7.6 illustrate the evolutions of the first harmonic and the second harmonic responses, respectively.

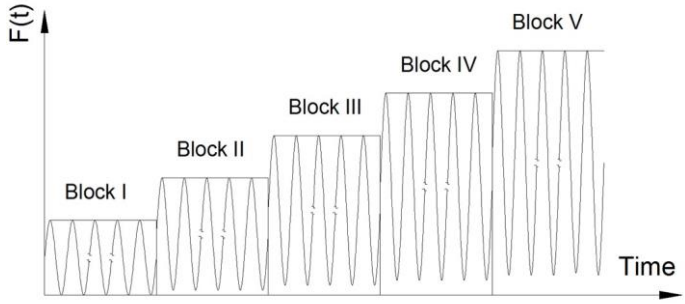

Figure 7.4 Schematic illustration of block loading fatigue test

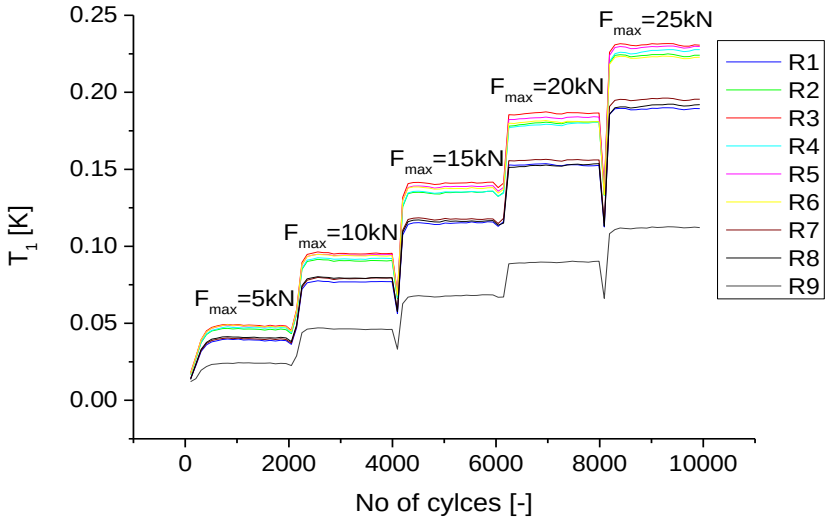

Figure 7.5 Evolution of the thermoelastic effect during the block loading test

The amplitude of the first harmonic is confirmed to increase with the stepwise load due to the thermoelastic effect. The lowest amplitude occurs in the ROI R_9 outside the valley, and the observed amplitude difference between ROIs along the valley is due to a local plane strain or plane stress condition. The closer to the centre of the specimen width, the closer to a plane strain condition. On the other hand, the second harmonic response allows to indicate which loading block does not generate any fatigue damage. Clearly, the second harmonic effect only appears after the third block and only along the valley of the bend. The second harmonic response at ROI R_9 is almost independent of the loading block. This observation enables to conclude that a best estimate of the fatigue limit of the bent specimen is the stress level corresponding to the second load block (F_{max} = *10 kN* or σ_{max} = *200 MPa*). This estimated fatigue limit of the bent sample is almost three times lower than the material fatigue limit of the dog-bone specimen *(570 MPa)*. At a first look, we may think that the bending process lowers the fatigue strength, but more experiments need to be performed to come to this conclusion since the duration to define the fatigue limit is different. The one of the standard dog-bone sample is at *2 10^6 cycles* whilst the estimated value of the bent specimen should be infinite, i.e. at *10^7cycles*, the upper boundary of the high cycle regime.

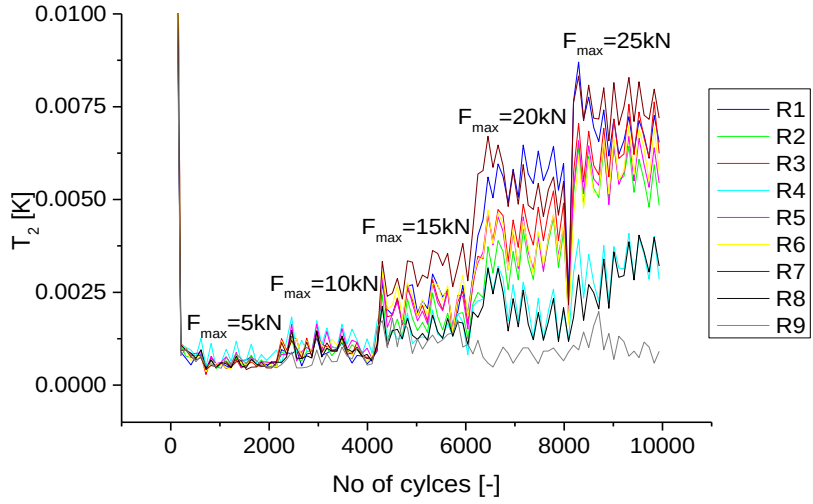

Figure 7.6 Evolution of the second harmonic effect during the block loading test

3.3 On-line detection of crack initiation

Monitoring the first harmonic response at the most damaging region of interest allows to detect on-line the moment of crack initiation. Unlike for fretting fatigue tests where thermal images needed to be captured for the first *1 000 cycles* to determine the most critical region of interest, the most damaging area of the bent specimen is known to be along the valley of the

bend root. These locations are easily obtained from the live thermal images of the camera. Their coordinates are implemented in the Matlab code for the on-line data acquisition and processing to calculate the thermoelastic effect. Results of two preliminary tests with identical test conditions, F_{max}*=40kN, R-ratio=0.1, f=5 Hz*, frame rate *50 Hz*, are shown in Figure 7.7 and Figure 7.8. The former test is on a sample with ground surface, and the latter test is on a sample with peened surface at the bend root. The maximum on-line data acquisition rate is *50 Hz* so that the loading frequency is reduced to *5 Hz* to maintain a sampling rate of *10 samples* per one cycle.

In fretting fatigue, the evolution of the first harmonic response is divided into three stages: running-in, stabilization and crack propagation. The thermoelastic temperature amplitude in fretting fatigue is supposed to result in a temperature rise during the crack propagation, according to equation (7-1), but this parameter drops when the crack reaches the front surface. Similarly to fretting fatigue, the thermoelastic temperature amplitude should increase when a crack occurs as observed in the first test at the ROI R_3, Figure 7.7. However, it drops at the ROI R_6 in the second test after the stabilization stage (see Figure 7.8). For this test, a possible reason for the difference in the evolution of the thermoelastic temperature amplitude during the crack propagation stage is the position of the ROI relative to the crack zone. The temperature rises if the crack is nearby the ROI due to stress concentration but drops if the crack is inside the ROI since it generates a void inside the ROI. A similar observation has been made for a voided surface crack of a welded joint [Ummenhofer & Medgenberg, 2009].

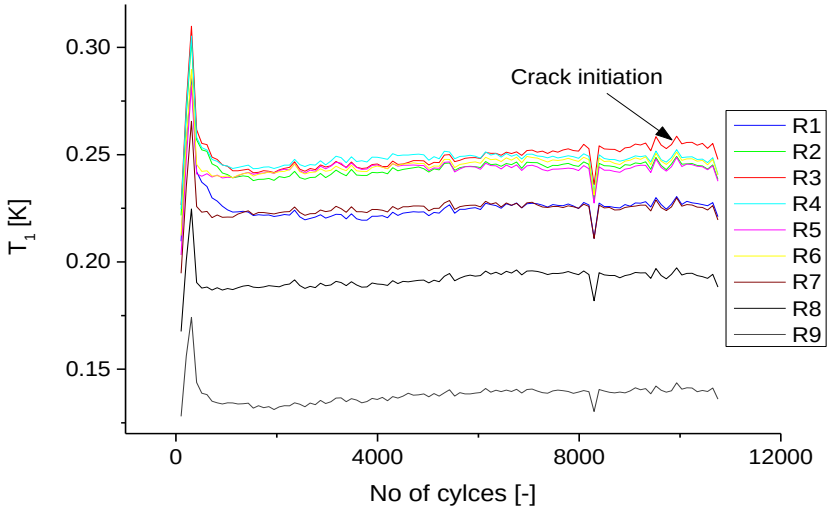

Figure 7.7 Evolution of the thermoelastic effect during a low cycle fatigue test (F_{max}*=40kN, R-ratio=0.1, f=5 Hz*, ground surface) until indication of crack initiation

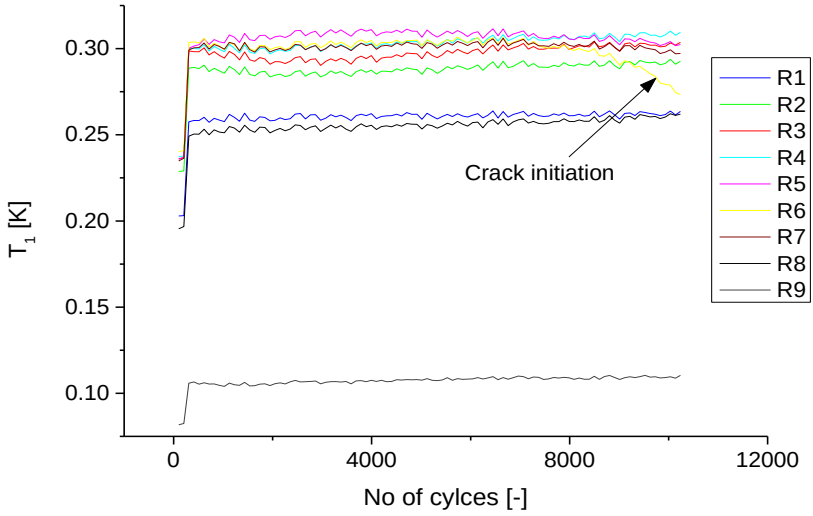

Figure 7.8 Evolution of the thermoelastic effect during a low cycle fatigue test (F_{max}=40 kN, R-ratio=0.1, f=5 Hz, peened surface) until indication of crack initiation

The testing machine and the on-line data processing with Matlab are stopped when a thermal indication of crack initiation appears, i.e. an increase or decrease of the thermoelastic temperature amplitude after the horizontal stabilized regime with a value larger than the filtered signal-to-noise ratio around *2 mK*. A scratch is marked on the sample surface at the specific region of interest, i.e. at R_3 for the first test and at R_6 for the second test, determined from the live thermal images of the camera. The sample is first cut transversely to take out the bend root of the specimen, and then along the longitudinal direction of the specimen passing through the scratched mark. After that, it is embedded in a bakelite epoxy, ground and polished to inspect for crack length by a scanning electron microscope. The procedure is shown in Figure 7.9a and a micro-crack of *54 μm* is revealed in Figure 7.9b for the second test.

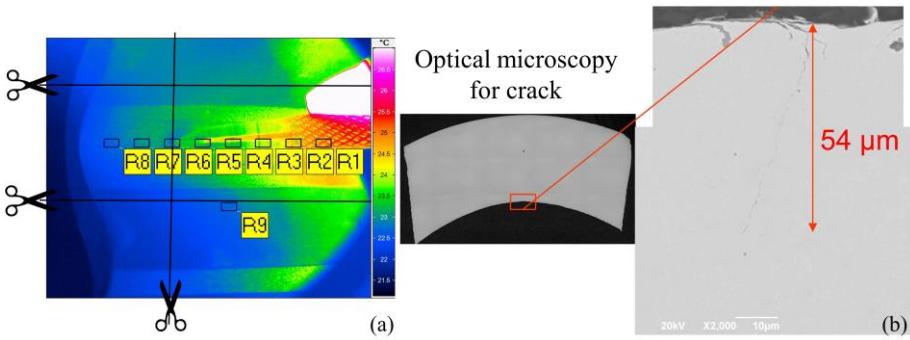

Figure 7.9 Off-line crack inspection by SEM

Unfortunately, no crack has been found for the first test, which can be due to a few reasons. Firstly, the off-line inspection for the crack is performed on a single plane passing through the exact marked region of interest. Several sectional planes in the vicinity of the specific region of interest should be made. Secondly, the grinding and polishing process may have removed the crack from the embedded sample.

3.4 Ratio of crack initiation to total lifetime

Continuing the fatigue test until the final rupture of the specimen, the evolution of the thermoelastic effect allows to separate the crack initiation and propagation lifetimes. In an exploratory test whose conditions are F_{max} = *30 kN, R-ratio = 0.1*, and f = *5Hz*, the thermoelastic effect of some regions of interest begins to drop (R_7 & R_8) but increases for other regions of interest (R_2 R_3 & R_4) during an early stage of the crack propagation at the cycle number *11 000 cycles* as shown in Figure 7.10.

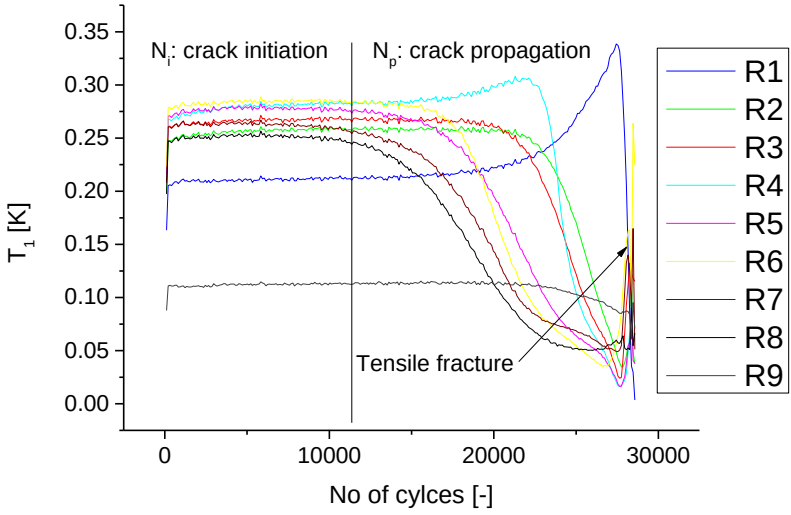

Figure 7.10 Evolution of the thermoelastic effect during a low cycle fatigue test (F_{max}=*30 kN, R-ratio=0.1, f=5 Hz*) until final rupture

The change of the first harmonic at the other regions of interest seems to be influenced by cracking, which likely appears around the five mentioned regions of interest. Again this observation confirms the possible influence on the thermoelastic effect of the position of the crack compared to the region of interest. Hence, to discriminate the crack initiation from crack propagation lifetimes, one can take the moment when an increase or a drop of the thermoelastic temperature amplitude larger than the filtered signal-to-noise ratio, *2 mK*, is evidenced. From Figure 7.10, the crack initiation time, N_i, can be determined as *11 000 cycles* while the remaining time until the tensile fracture of the specimen at N_f = *29 500 cycles* is the crack propagation time, i.e *Np = 18 500 cycles*. Then the proportion of N_i/N_f is found to be *37.28 %* which

means that the specimen lifetime is dominated by the crack propagation stage. This result is in contrast with the conclusion from the cross-head displacement based method applied to an identical fatigue test, see Figure 7.2. The root cause of the opposite finding is the much better sensitivity of the thermographic method for crack detection. Its detection threshold equals $54\ \mu m$ compared to $600\ \mu m$ for the cross-head displacement method. This improved finding suggests that the technique used to extend the total lifetime should be based on the crack propagation impediment instead of crack initiation impediment.

4 Summary and conclusions

The developed experimental methodologies yield satisfactory results for the low cycle fatigue tests on bent samples. That includes the rapid determination of the fatigue limit, the on-line detection of crack initiation, and the separation of the crack initiation and crack propagation lifetimes. However, a validation test is still required to confirm the fatigue limit condition, i.e. that the specimen remains intact at $10^7\ cycles$. The fatigue limit is studied base on the second harmonic effect, while the on-line crack detection is based the first harmonic. The detected crack length is rather small, $54\ \mu m$ which is a more than 10 times improvement compared to the conventional method based on the displacement of the cross-head. With such a small detection threshold, the crack initiation and propagation times can be more accurately discriminated. Like fretting fatigue, the thermoelastic effect shows three stages: running-in, stabilization, and crack propagation. Similar to fretting fatigue, the thermoelastic temperature amplitude is not always increased as is expected from the basic thermoelastic relation. It can also drop depending on the location of the initiated crack with respect to the region of interest. The methodologies originally developed for fretting fatigue, are therefore expected to perform well for other types of fatigue tests and also other metals under the condition that the location of the crack can be estimated prior to the tests.

References

Colombo, C., Vergani, L., Burman, M. (2012) Static and Fatigue Characterisation of New Basalt Fibre Reinforced Composites. *Composite Structures*, 94, 1165–74.

Fargione, G., Geraci, A., Rosa, G. La, Risitano, A., Doria, V.A. (2002) Rapid Determination of the Fatigue Curve by the Thermographic Method. *International Journal of Fatigue*, 24, 11–9.

Luong, M.P. (1998) Fatigue Limit Evaluation of Metals Using an Infrared Thermographic Technique. *Mechanics of Materials*, 28, 155–63.

Micone, N., De Waele, W. (2016) On the Application of Infrared Thermography and Potential Drop for the Accelerated Determination of an S-N Curve. *Experimental Mechanics*, 57, 143–53.

Montesano, J., Fawaz, Z., Bougherara, H. (2013) Use of Infrared Thermography to Investigate the Fatigue Behavior of a Carbon Fiber Reinforced Polymer Composite. *Composite Structures*, 97, 76–83.

Risitano, A., Risitano, G. (2010) Cumulative Damage Evaluation of Steel Using Infrared Thermography. *Theoretical and Applied Fracture Mechanics*, 54, 82–90.

Rosa, G. La, Risitano, A. (2000) Thermographic Methodology for Rapid Determination of the Fatigue Limit of Materials and Mechanical Components. *International Journal of Fatigue*, 22, 65–73.

Talemi, R.H., Chhith, S., De Waele, W. (2017) Experimental and Numerical Study on Effect of Forming Process on Low-Cycle Fatigue Behaviour of High-Strength Steel. *Fatigue & Fracture of Engineering Materials & Structures*, 1–18.

Ummenhofer, T., Medgenberg, J. (2009) On the Use of Infrared Thermography for the Analysis of Fatigue Damage Processes in Welded Joints. *International Journal of Fatigue*, 31, 130–7.

Chapter 8 Conclusions and recommendations for future work

"In this chapter, the main contributions of this dissertation towards the extension of the state of the art on the application of infrared thermography for the study of fretting fatigue is summarized. Some suggestions for future research work to further progress in the understanding of fretting fatigue are elaborated"

1 Problem statement and objectives

Fretting can occur when two interacting surfaces are subjected to a small reciprocal relative displacement. Fretting induced stress raisers may accelerate the formation of a fatigue crack so that fatigue lifetime is significantly reduced. Like for plain fatigue, fretting fatigue lifetime is divided into two main parts: crack initiation and crack propagation. A fracture mechanics approach allows to solve the crack propagation stage, but the crack initiation phase is far more challenging. There is a lack of knowledge with respect to the crack formation process, the detection of crack initiation, and the size effect. Fretting fatigue damage occurs at the trailing edge of the contact area, and it is likely to be hidden at the centre of the contact since typical contact damage is more severe under a plane strain than a plane stress condition. This makes it extremely hard to obtain detailed information on the crack initiation. So far the crack formation process is still a mystery and only a very limited number of experimental works have succeeded in detecting the crack initiation.

Developed analytical and numerical models to predict the crack initiation lifetime have been validated by destructive microscopy [Fouvry & Kubiak, 2009], by post-mortem analysis [Lykins, Mall & Jain, 2001], or by total lifetime [Araújo & Nowell, 2002; Szolwinski & Farris, 1996]. These models, validated for typical cylindrical on plane contact, are expected to be applicable to real engineering problems for which the contact type is different and more complex. The size effect raises a debate about this possibility, as it suggests that a stress-based parameter alone is not sufficient to predict crack initiation lifetime under fretting fatigue. The above mentioned authors based their models on an equivalent parameter, a combination of stress and strain, from multiaxial fatigue criteria. Even though [Fouvry, Gallien & Berthel, 2014] claimed to improve their model to incorporate the size effect it was only validated by experiments using a cylindrical on plane contact. A new type of contact within a coupon scale test is required.

The main objectives of this thesis have been defined as follows:

- Develop a thermographic method to investigate fretting fatigue damage of two different metals subjected to a cylindrical on plane contact.

  Develop an on-line thermographic method to detect fretting fatigue crack initiation, and to separate the crack initiation and the propagation lifetimes of the two metals and a cylindrical on plane contact.

- Provide a collection of experimental data on crack initiation lifetime in fretting fatigue tests for two different metals and two different

contact types that would allow validation of analytical and numerical models.

2 Methodologies developed

The methodologies developed in this dissertation are purely experimental and based on infrared thermography. The UGent fretting fatigue test rig with a single actuator has been optimized, and several series of fretting fatigue tests have been performed and monitored by an infrared camera for achieving the above mentioned objectives.

For rapid determination of the fretting fatigue limit, a sequential block loading scheme developed for plain fatigue has been adopted (Figure 8.11). The amplitude of the applied fatigue load together with the magnitude of the tangential force was increased block by block while the normal force was kept constant. Each block was run with a loading frequency of *10 Hz* for *5 000 cycles* and thermal images were recorded with a frame rate of *100 Hz* to obtain *10* data points per loading cycle. The IRBIS3 camera software was used to extract data from the four regions of interest, and then the Matlab Fast Fourier Transform (FFT) was used to analyse the temperature response corresponding to each loading block. The last loading block for which the second harmonic is zero or negligible has been considered as the best estimate of the fretting fatigue limit. Three repeat tests were performed to confirm the observation. Additionally a fretting fatigue test with constant stress amplitude was run for 10^7 *cycles* to verify the infinite life of the specimen at the determined fatigue limit.

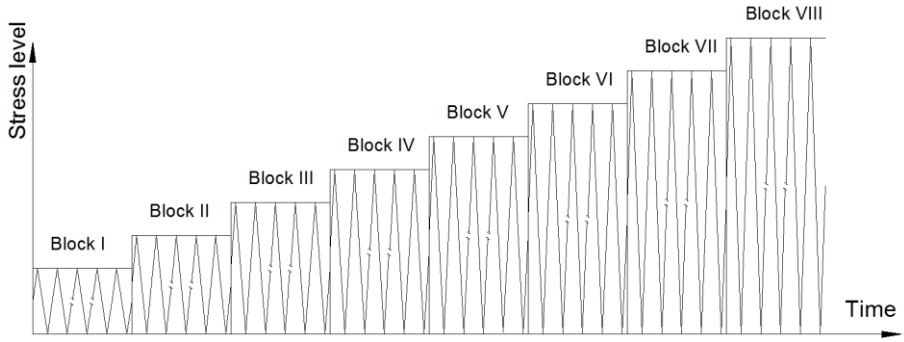

Figure 8.11 Schematic representation of block loading methodology for determination of the fretting fatigue limit

The sequential block loading method allowed not only to predict the fretting fatigue limit but also to indicate the loading blocks generating fretting damage. Test conditions for the validation of the methodology for on-line detection of crack initiation were selected from these load blocks as a crack could never be initiated without accumulation of fretting fatigue damage.

The parameter indicating crack initiation was the first thermoelastic temperature amplitude (the first harmonic). This parameter was monitored at four regions of interest and processed on-line from the overall experimental temperature by the standard lock-in or the FFT algorithm. The maximum on-line data acquisition rate was *50 Hz* and the loading frequency was reduced to *5 Hz* to keep the number of samples per cycle equal to *10*. The coordinates of the four regions of interest were determined from a thermal image captured during the first *1 000 cycles* of the test. The thermoelastic effect was shown to consist of three distinct stages: running-in, stabilization (a horizontal line) and crack propagation. At the moment that the thermoelastic temperature amplitude increased from the stabilization stage by a magnitude of *2 mK* (the filtered signal-to-noise ratio), the test was stopped and the sample inspected by optical microscopy. Figure 8.12 illustrates the methodology of this on-line crack detection technique. The procedure has been extended to enable the determination of the ratio of crack initiation time to total lifetime.

The developed methodologies have been applied to fretting fatigue tests on two different metals and contact types and also to low cycle fatigue tests on a bent specimen in order to confirm if they can be used for general cyclic loading experiments.

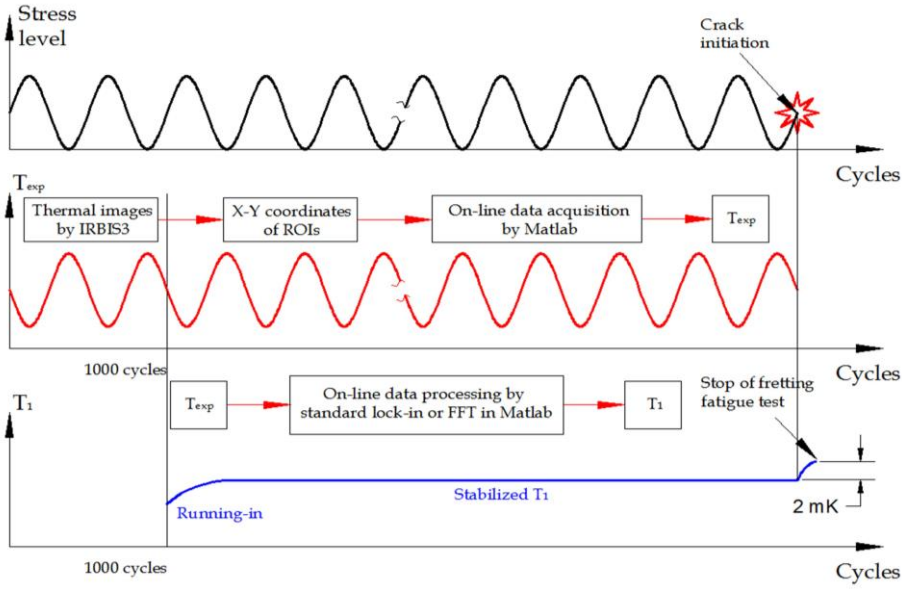

Figure 8.12 Methodology for on-line detection of fretting fatigue crack initiation

3 Main results and conclusions

Fretting fatigue tests on Al2024-T3 and S235JRC specimens have been performed for *40 000 cycles* using a stepwise block loading scheme. The fretting fatigue limit of both materials has been predicted quickly within a few hours of testing by analysing the temperature response with the Matlab FFT algorithm to determine the second harmonic temperature amplitude. This parameter linked to fretting fatigue damage will allow to investigate the origin of the size effect; either a crack is initiated but arrested or either a crack is not initiated below a critical contact area. On the other hand, the possibility of damage monitoring during a fretting fatigue test, allows to study whether there are cases for which micro-slip stops after a few cycles, i.e. the second harmonic effect diminishes, and thus failure of the materials is not to be expected. The methodology is basically non-destructive and has also been successfully applied to find the fatigue limit of a bent specimen.

Fretting fatigue tests with constant fatigue load amplitude have been conducted on both aluminium and steel specimens and were monitored by the infrared camera. The standard lock-in algorithm or FFT allowed an on-line signal processing reducing the nominal signal-to-noise ratio to *2 mK*. A micro-crack in the closed contact within a range from *130* to *220 μm* depth could be detected for several stress levels. The crack initiation lifetime during fretting fatigue tests with line contact takes up to 60% on average of the total lifetime for both metals. The methodology has been applied to fretting fatigue tests with an elliptical contact. Similarly, the crack initiated at the trailing edge of the elliptical contact area and grew into the depth of the specimen. On-line detection of crack initiation could be achieved, and the detected crack length was around *200 μm* on average for several stress levels. The developed data series for both metals and contact types could enable a better validation of multi-axial fatigue models for prediction of crack initiation under fretting fatigue. The developed experimental methodology also allowed to on-line detect crack initiation during a low cycle fatigue test on a bent HSS specimen with a minimum crack length of *54 μm*. Therefore, it is expected to work well for any fatigue tests in which the location of an initiated crack can be accurately estimated prior to the test.

4 Recommendations for future work

4.1 Experiments

4.1.1 Improved crack detection threshold

By comparing the infrared thermography technique with the potential drop technique applied by [Meriaux et al., 2010], it is concluded that the detection threshold cannot yet reach the threshold value of the potential drop method (*50 μm* crack length). However, the main advantage of the IR based method is

the simplicity of the experimental preparation as no calibration is needed. The aim is to achieve the same threshold in future work. As observed in the off-line statistical analysis, the rise of the thermoelastic temperature amplitude occurs actually before stopping the test, but could not be visualized on-line by the operator. Reliable on-line statistical analysis will most probably allow to stop the test at an earlier stage of crack initiation and improve the detection threshold.

On the other hand, the detection threshold could be improved if the test can be performed with a fatigue ratio of -1. With an *R-ratio=-1*, the presence of a crack would lead to a larger increase of the thermoelastic temperature amplitude than with an *R-ratio=0.001* since it affects the thermoelastic temperature at both the minimum and maximum stress values (see Figure 8.13). Because of the crack-induced stress concentration, the thermoelastic temperature drops and rises further at the maximum tensile and compressive stresses respectively. At the maximum compressive stress, the crack faces might touch each other resulting in an additional source for the temperature rise.

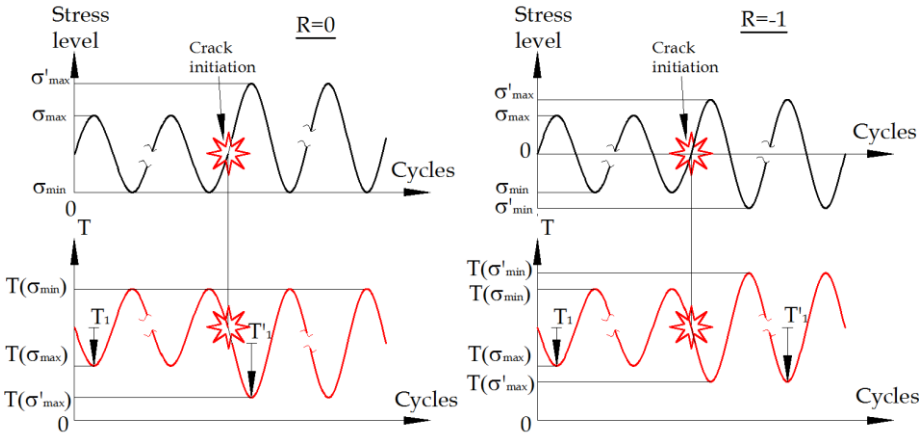

Figure 8.13 The effect of fatigue ratio on the detection threshold

An upgrade of the lens to obtain a smaller pixel size of the thermal image would also enable a smaller detection threshold. The smaller the pixel size, the clearer the spatial temperature distribution at the contact zone. This allows a smaller size of the ROIs since it guarantees the correct location of the ROIs at the highest temperature point (estimated location of the crack initiation). Since the thermoelastic temperature amplitude, the indicator for crack initiation, is averaged over the ROIs, a smaller size of the ROIs would improve the detection threshold and the moment of crack initiation.

4.1.2 Three actuator test rig

Development of a three actuator fretting fatigue test rig is necessary to study interaction effects of the three fretting fatigue forces (σ, P, Q) on the fretting

fatigue limit, crack initiation and propagation lifetimes. In this dissertation the fretting fatigue limit is represented by a combination of three parameters: σ_0, P_0, Q_0. Without independent control of these parameters, one cannot conclude which parameter has the major influence on the fretting fatigue limit. On the other hand, the current fretting fatigue test rig, with a single actuator, does not allow to investigate a combination of low fatigue force with high fretting loads. Because of this disadvantage it is not possible to make a generic conclusion on which proportion of fretting fatigue lifetime, crack initiation or propagation dominates for all combinations of fatigue and fretting forces even though the methodology to separate the crack initiation from the crack propagation is well developed in this work.

4.1.3 Size effect and fretting fatigue damage

The fretting fatigue lifetime might shift from a few hundred thousand cycles to infinity below a critical contact area even though the stress level and the contact pressure are the same. This phenomenon is called the size effect. Two approaches have been used to explain this effect: crack initiation and crack arrest. Following the crack initiation approach, one may argue that below the critical contact area the slipping zone is too small and thus the frictional surface damage too low to accumulate into a crack. Following the crack arrest approach one may argue that the crack can be initiated but arrested due to the nature of the steep stress gradient below the critical contact area. The answer to this debate might be found using the developed thermographic method for detecting the fretting fatigue damage. If the fretting fatigue test with the contact area below the critical area does not generate any fretting fatigue damage, shown by the second harmonic temperature response, it means that the crack initiation approach is likely to be more correct. Otherwise, it is the crack arrest phenomenon which is controlling the size effect.

4.1.4 Size effect of another contact type in fretting fatigue

The size effect is an important challenge to allow a correlation being made between a coupon scale test and real engineering problems. The effect has been observed in fretting fatigue tests with cylindrical on plane contact for different metals such as aluminium alloy, titanium alloy and high strength steel. This effect has not been discovered yet for other contact types like spherical on plane contact and perpendicular cylinders. Hence, it would be interesting to confirm this effect for other contact types too, since it is a critical physical phenomenon for the philosophy of doing research in the field of fretting fatigue. 95% of the researchers might have been trying to correlate the coupon scale test results to real engineering problems, using a multiaxial fatigue criterion which is a purely stress-based approach. They are probably underestimating the size effect.

4.1.5 Frictional shakedown

Frictional shakedown is a phenomenon where friction ceases after the first few cycles. The phenomenon has been observed in several contact problems [Barber, Klarbring & Ciavarella, 2008; Klarbring et al., 2017; Klarbring, Ciavarella & Barber, 2007] and it is therefore speculated if it might also occur for a partial-slip contact [Hills & Nowell, 2014]. If frictional shakedown does occur, micro-slip of the partial slip regime will stop and result in complete sticking between the two interacting surfaces. In this case the stress raiser induced by fretting disappears and will assure that fretting has no effect on lifetime. This shakedown in fretting fatigue can certainly be studied by the thermographic method based on the damage detection developed in Chapter 5.

4.1.6 Microscopic investigation of fretting damage and crack initiation

One of the main challenges in understanding the mechanics of the fretting fatigue is the crack formation process. The author believes that to tackle this issue, further microscopic investigation of the surface damage induced by fretting fatigue damage should be performed. Especially focussing on the moment when a micro-crack is initiated. In this work, the sample has been cross-sectioned to inspect for crack length, but further study should allow in-depth investigation on a microscopic level at the onset of crack initiation. Hopefully, the crack formation process can be revealed.

4.2 Numerical modelling

All results in this dissertation are derived from coupon scale experiments. When the size effect is not yet resolved, these results should not be related to real engineering problems. An additional benefit of these results is their use for validating analytical and numerical models to further understand the crack initiation stage of fretting fatigue. Of course, the developed models need to address the size effect. The author suggests to adopt the model developed by [Fouvry, Gallien & Berthel, 2014] claiming to solve the size effect of the cylindrical on plane contact and to validate it with the data of both materials and the two contact types developed in this work. On the other hand, from a micromechanics point of view, once the crack formation process is revealed, lifetime to crack initiation can be modelled based on this experimental proof as proposed by [Fellows, Nowell & Hills, 1997].

References

Araújo, J.A., Nowell, D. (2002) The Effect of Rapidly Varying Contact Stress Fields on Fretting Fatigue. *International Journal of Fatigue*, 24, 763–75.

Barber, J.R., Klarbring, A., Ciavarella, M. (2008) Shakedown in Frictional Contact Problems for the Continuum. *Comptes Rendus Mecanique*, 336, 34–41.

Fellows, L.J., Nowell, D., Hills, D.A. (1997) On the Initiation of Fretting Fatigue Cracks. *Wear*, 205, 120–9.

Fouvry, S., Gallien, H., Berthel, B. (2014) From Uni- to Multi-Axial Fretting-Fatigue Crack Nucleation : Development of a Stress-Gradient-Dependent Critical Distance Approach. *International Journal of Fatigue*, 62, 194–209.

Fouvry, S., Kubiak, K. (2009) Introduction of a Fretting-Fatigue Mapping Concept: Development of a Dual Crack Nucleation – Crack Propagation Approach to Formalize Fretting-Fatigue Damage. *International Journal of Fatigue*, 31, 250–62.

Hills, D.A., Nowell, D. (2014) Mechanics of Fretting fatigue—Oxford's Contribution. *Tribology International*, 76, 1–5.

Klarbring, A., Barber, J.R., Spagnoli, A., Terzano, M. (2017) Shakedown of Discrete Systems Involving Plasticity and Friction. *European Journal of Mechanics, A/Solids*, 64, 160–4.

Klarbring, A., Ciavarella, M., Barber, J.R. (2007) Shakedown in Elastic Contact Problems with Coulomb Friction. *International Journal of Solids and Structures*, 44, 8355–65.

Lykins, C.D., Mall, S., Jain, V.K. (2001) Combined Experimental – Numerical Investigation of Fretting Fatigue Crack Initiation. *International Journal of Fatigue*, 23, 703–11.

Meriaux, J., Fouvry, S., Kubiak, K.J., Deyber, S. (2010) Characterization of Crack Nucleation in TA6V under Fretting–fatigue Loading Using the Potential Drop Technique. *International Journal of Fatigue*, 32, 1658–68.

Szolwinski, M.P., Farris, T.N. (1996) Mechanics of Fretting Fatigue Crack Formation. *Wear*, 98, 93–107.

Appendices

A. Schematic drawing of the UGent fretting fatigue fixture

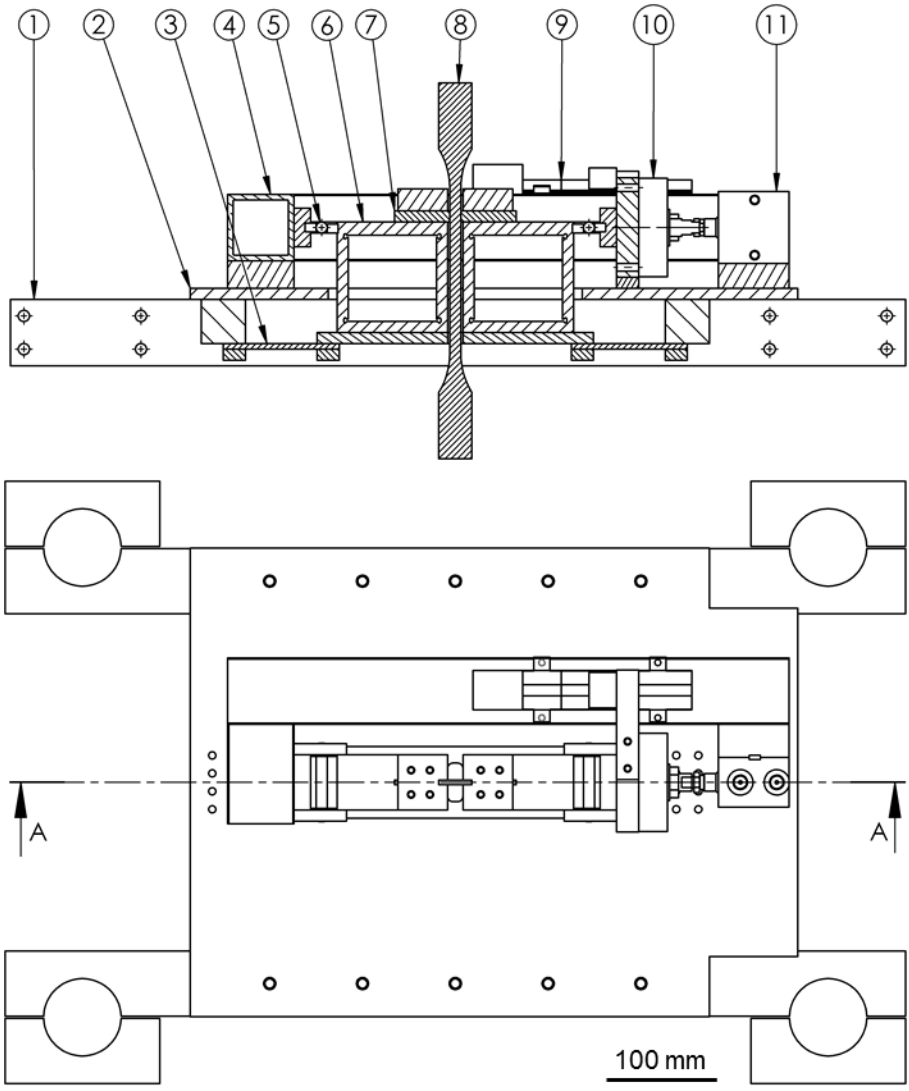

Figure A.1 Section view and top view of the fretting fixture. 1) horizontal support, 2) base plate, 3) leaf springs, 4) C-beam, 5) roller bearing, 6) pad holder, 7) pad, 8) dog-bone specimen, 9) displacement sensor, 10) load cell, 11) hydraulic actuator [De Pauw, 2016]

B. Mathematical background of lock-in correlation

The principal idea of this lock-in correlation is taken from [Breitenstein, O., Warta, W., Langenkamp, 2010], but more detailed mathematical integration is shown in this appendix.

Let us assume:

An input signal: $F(t)=A\sin(2\pi f_{lock\text{-}in}t+\Phi)$

An in-phase harmonic correlation function: $K^0=2\sin(2\pi f_{lock\text{-}in}t)$

A 90° out of phase harmonic correlation function: $K^{90}=2\cos(2\pi f_{lock\text{-}in}t)$

Then,

the in-phase correlation output S^0 can be determined by the integration,

$$S^0 = \frac{1}{t_{\text{int}}}\int_0^{t_{\text{int}}} F(t)K^0(t)dt$$

$$= \frac{1}{t_{\text{int}}}\int_0^{t_{\text{int}}} A\sin(2\pi f_{lock-in}t+\phi)2\sin(2\pi f_{lock-in}t)dt$$

$$= \frac{1}{t_{\text{int}}}\int_0^{t_{\text{int}}} \left(2A\sin(2\pi f_{lock-in}t+\phi)\sin(2\pi f_{lock-in}t)\right)dt$$

$$= \frac{1}{t_{\text{int}}}\int_0^{t_{\text{int}}} A\left(\cos(2\pi f_{lock-in}t+\phi-2\pi f_{lock-in}t)-\cos(2\pi f_{lock-in}t+\phi+2\pi f_{lock-in}t)\right)dt$$

$$= \frac{1}{t_{\text{int}}}\int_0^{t_{\text{int}}} A\left(\cos(\phi)-\cos(4\pi f_{lock-in}t+\phi)\right)dt$$

$$= A\cos(\phi)-\frac{A}{t_{\text{int}}}\int_0^{t_{\text{int}}}\left(\cos(4\pi f_{lock-in}t+\phi)\right)dt = A\cos(\phi)-\frac{A}{t_{\text{int}}}\left(\sin(4\pi f_{lock-in}t+\phi)\right)_0^{t_{\text{int}}}$$

For a large enough integration time, $t_{int} >> t_{lock\text{-}in}$, the second term diminishs as it is a difference between two repeated values of a periodic function. Note well that in case the input signal, F(t), consists of other harmonics with any other frequencies or *D.C.* components, the output is only non-zero at the lock-in frequency of the reference signal because of the same reason, i.e. the difference between two repeated values of a periodic function. This reults in the following simple expression for the in-phase correlation output:

$$S^0 = A\cos(\phi)$$

The quadrature correlation output S^{90} can be determined by the integration,

$$S^{90} = \frac{1}{t_{\text{int}}} \int_0^{t_{\text{int}}} F(t)K^{90}(t)dt$$

$$= \frac{1}{t_{\text{int}}} \int_0^{t_{\text{int}}} A\sin(2\pi f_{lock-in}t + \phi)2\cos(2\pi f_{lock-in}t)dt$$

$$S^{90} = \frac{1}{t_{\text{int}}} \int_0^{t_{\text{int}}} \left(2A\sin(2\pi f_{lock-in}t + \phi)\cos(2\pi f_{lock-in}t)\right)dt$$

$$= \frac{1}{t_{\text{int}}} \int_0^{t_{\text{int}}} A\left(\sin(2\pi f_{lock-in}t + \phi + 2\pi f_{lock-in}t) + \sin(2\pi f_{lock-in}t + \phi - 2\pi f_{lock-in}t)\right)dt$$

$$= \frac{1}{t_{\text{int}}} \int_0^{t_{\text{int}}} A\left(\sin(4\pi f_{lock-in}t + \phi) + \sin(\phi)\right)dt$$

$$= \frac{A}{t_{\text{int}}} \int_0^{t_{\text{int}}} \left(\sin(4\pi f_{lock-in}t + \phi)\right)dt + A\sin(\phi)$$

In a similar way to the in-phase correlation, this output can be simply written as follows:

$$S^{90} = A\sin(\phi)$$

C. Material certificates of the used aluminium alloys

AMAG_
ROLLING

Abnahmeprüfzeugnis 3.1 (EN 10204)
Certificat de réception

Nr.: 85196029 **01 / 1**
Rev.: 0
Seite / Page: 1 von / de 3
Datum / Date: 2014 09 01

Zertifiziert nach / Certifié selon ISO 9001, ISO/TS 16949, EN/AS 9100, ISO 14001, NADCAP

Auftraggeber / Donneur d'ordre: ThyssenKrupp Materials	Bestell Nr. / Votre commande N°: 91273 Datum / Date: 2013 11 26
	Auftragsbest. Nr. / Conf. de comm. N°: 667823 Datum / Date: 2013 12 11
Warenempfänger / Destin. de la march.: Thyssenkrupp Materials	Lieferschein Nr. / Bon de livraison N°: 85196029 Datum / Date: 2014 09 03

Produkt / Produit	**Bedingungen / Conditions**
Form / Forme: tôles Werkstoff / Alliage: 2024 Zustand / Etat: T3 Dim. / dim.: [mm]: 5,00x1250,0x2500,0	Techn. Lieferbedingungen / Cond. de livraisons techniques: AMS-QQ-A-250/4A, 09.1998 ASTM B 209 - 10 AMS 4037P, 12.2011 ASNA 3010, Issue: K, 05.2011, Eurocopter approval only WL 3.1354-1, 12.1987 LN 9073, 09.1991 ABM 1-6015, Issue 2, OCT 2004 AIR9048-110, 26 December 1978 BS 5L 100, 2011 NF L 15-115, Rev. 07, 1973 EN 2071 : 2001 Sondervorschrift / Prescription spéciale:

AB-Pos. Pos. Cde.	BNr/Los/Teillos No. De Trav.	Guss Nr. Coulée	Werkstoff Alliage	Kollo Colis	Gewicht netto Poids net.	Stk. Pcs.
02	67257/01/00	01/0060841/4	2024	6678230001	1088 kg	25
02	67257/01/00	01/0060841/4	2024	6678230002	1088 kg	25

Chemische Zusammensetzung ([%] Gewichtsanteile) / Composition chimique ([%] Quote-part du poids)

Guss Nr./ Coulée	Matériel										
01/0060841/4	2024	Si	Fe	Cu	Mn	Mg	Cr	Zn	Ti	Ti+ Zr	Autres Chaque
	spec. min.	-	-	3,8	0,30	1,2	-	-	-	-	-
	spec. max.	0,50	0,50	4,9	0,90	1,8	0,10	0,25	0,15	0,20	0,05
	actual	0,08	0,12	4,4	0,51	1,5	0,00	0,08	0,04	0,05	0,02
		Autres Somme									
	spec. min.	-									
	spec. max.	0,15									
	actual	0,03									

AMAG_
ROLLING

Abnahmeprüfzeugnis 3.1 (EN 10204)
Certificat de réception

Nr.: 85196029 **01 / 1**
Rev.: 0
Seite / Page: 2 von / de 3
Datum / Date: 2014 09 01

Zertifiziert nach / Certifié selon ISO 9001, ISO/TS 16949, EN/AS 9100, ISO 14001, NADCAP

Zugprüfung L / essai de traction L

BNr/Los No. De Trav.	Zustand Etat	Direction direction	Tests		Rm [MPa]	Rp0.2 [MPa]	A50 [%]			
				spec.min.	450	325	-			
				spec.max.	-	-	-			
67257/01	T3	L	8	from	472	371	17			
67257/01	T3	L		to	483	383	19			

Zugprüfung LT / essai de traction LT

BNr/Los No. De Trav.	Zustand Etat	Direction direction	Tests		Rm [MPa]	Rp0.2 [MPa]	A50 [%]			
				spec.min.	445	290	15			
				spec.max.	-	-	-			
67257/01	T3	LT	8	from	462	352	16			
67257/01	T3	LT		to	465	359	17			

Elektr. Leitfähigkeit GM / Conductivité electr. GM

BNr/Los No. De Trav.	Zustand Etat	Tests		L / ec [MS/m]	ΔL / Δec per batch [MS/m]			
			spec.min.	-	-			
			spec.max.	19,0	1,5			
67257/01	T3	24	from	17,9	0,2			
67257/01	T3		to	18,1	0,2			

Sonstige Prüfungen / Autres contrôles

Biegeversuch: OK. / Essai de pliage: OK.
Interkristalline Korrosion: OK. / Corrosion intercranulaire: OK.
Maßkontrolle: OK. / Contrôle dimensionnel: OK.
Oberfläche: OK. / Surface: OK.

AMAG_
ROLLING

Abnahmeprüfzeugnis 3.1 (EN 10204)
Certificat de réception

Nr.: 85196029 **01 / 1**
Rev.: 0
Seite / Page: 3 von / de 3
Datum / Date: 2014 09 01

Zertifiziert nach / Certifié selon ISO 9001, ISO/TS 16949, EN/AS 9100, ISO 14001, NADCAP

Es wird bestätigt, dass die Lieferung geprüft wurde und den Vereinbarungen bei der Bestellung entspricht.
Il est confirmé que la livraison a été, contrôlée et est conforme aux engagements de l'accusé de réception de commande.

Ausgestellt nach Airbus Zulassung Nr. 30272.
Wir bestätigen, dass die gesamte Lieferung unter Einhaltung und soweit oben nicht anders dargelegt aller Forderungen (Spezifikationen, Zeichnungen, Aufträge) hergestellt und geprüft wurde.
Das Qualitätsmanagementsystem erfüllt die Anforderungen der AUK/SA/001-3.
Hergestellt, kontrolliert und geprüft nach Hawker Beechcraft HBIFSAS/PART3/0771
Agusta Westland Genehmigung Lieferantennummer V21275
Etabli selon l'approbation Airbus N°30272.
Nous confirmons que l'ensemble de la livraison a été fabriqué et contrôlé conformément à toutes les exigences de qualité posées (spécifications, plans, commandes) et pour autant que rien d'autres que celles mentionnées ci-dessus n'aient été exposées.
Le système d'assurance qualité remplit les exigences de l'AUK / SA / 001-3.
Elaboration , contrôles et tests suivant spécification Hawker Beechcraft HBIFSAS/PART3/0771
Agusta Westland, agrément code fournisseur V21275

Werksachverständiger / Expert usine	E-Mail / E-Mail
Klampfer Josef	josef.klampfer@amag.at

Herstellerland: Österreich / Pays d'origine: Autriche.
Maschinell erstellt - Gültig ohne Unterschrift / Établi par machine automatique, valable sans signature.

AMAG rolling
Werkssachverständiger
ROL-Nr. 015

Nuance : 2024 T
Coule : M714890 lot : 8417
Commande : BL :689576 Poste:01
Client : THYSSENKRUPP CHRISTON
CDE 3BA 5403692811

THYSSENKRUPP MATERIALS FRANCE
Une entreprise de ThyssenKrupp Services

Constellium Montreuil-Juigne SAS

Certificat de réception et déclaration de conformité
Inspection certificate and statement of conformity
Abnahmeprüfzeugnis und Übereinstimmungserklärung
DIN 50049-3.1 B - EN 10204-3.1

Commande client-Customer Order-Kundenbestellung	Destinataire - Consignee - Empfänger	Commande Constellium Asturias
THYSSENKRUPP	THYSSENKRUPP	158718/ 100/ 1
		N° de PV
		128047

Alliage - Alloy - Werkstoff	Norme - Standard - Norm	Produit - Product - Produkt
2024	ASNA3351G NCT1023503 MDS	BARRE RONDE FILEE EN2985
Etat - Temper - Zustand	EN2633:1994 EN2338:1552 CCT LA 279/2	56,00 MM 3000 MM
T3511	PROCESS AIR9049	

Coulées - Castings - Schmelze — Composition chimique (% en masse) - Chemical Composition - Chemische Zusammensetzung (1)

	Si	Fe	Cu	Mn	Mg	Cr	Ni	Zn	Ti	Zr	Pb			
R5219	0,11	0,29	4,49	0,76	1,33	0,02	0,01	0,14	0,03	0,13	0,0008			

Désignation des produits / Product description / Bezeichnung der Produkte
Observations - Dérogations/ Remarks - Deregations / Bemerkungen - Abweichungen

FOURNISSEUR HOMOLOGUÉ MESSIER-DOWTY PRIDE QA103 & CO419-1

Colis 468299 M714890	521,000 KG	26 PCS	
M714890 /8419	521,000 KG		
Colis 468300 M714890	520,000 KG	26 PCS	
M714890 /8419	520,000 KG		
Colis 468301 M714890	540,000 KG	27 PCS	
M714890 /8418	540,000 KG		
Colis 468302 M714890	480,000 KG	25 PCS	
M714890 /8418	480,000 KG		

Liste des contrôles par lot - Inspection List per batch - Kontrollen für jedes los
** = Périodiques / Periodic / Periodische Tests

CONTROLE MACROGRAPHIQUE	% :100
ESSAI DE TRACTION SENS LONG	Nb:2
CONTROLE DIMENSIONNEL	Nb:3
CONDUCTIVITE ELECTRIQUE	% :100
CONTRÔLE DIMENSIONNEL	% :10
CONTROLE US PRODUITS CORROYES	% :100

Résultats des essais - Test results - Zugversuche

N° de lot / Coulée / Etat de cuisse / Prélèvements N° sens-emplacement (2) épaisseur en/en/mm	Rm Tensile Strength MPa	Rp 0,2 Yield Strength MPa	A% Elongat %	Y sur éprouvette MS/m
LOT : M714890 /8417				
COULEE : R5219				
1 L D	574	448	12	
1 L F	567	444	13	
2 L D	570	445	13	
2 L F	567	445	13	
CONDUCTIVITE ELECTRIQUE :				
MINI : 16,7 MAXI : 17,1 MS/m				
CONTROLE MACROGRAPHIQUE				
--> RESULTATS CONFORMES				
CONTROLE US PRODUITS CORROYES				
--> RESULTATS CONFORMES				
LOT : M714890 /8418				
COULEE : R5219				
1 L D	570	450	14	
1 L F	566	446	13	
2 L D	569	445	13	
2 L F	562	448	13	
CONDUCTIVITE ELECTRIQUE :				
MINI : 16,9 MAXI : 17,2 MS/m				
CONTROLE MACROGRAPHIQUE				
--> RESULTATS CONFORMES				
CONTROLE US PRODUITS CORROYES				
--> RESULTATS CONFORMES				

Déclaration de conformité (NF L 00-015C)
Statement of conformity - Übereinstimmungserklärung

Nous déclarons que la fourniture citée est conforme aux exigences du contrat et qu'après vérifications et essais, elle répond en tout point, aux exigences spécifiées, aux normes et règlements applicables, sauf exceptions, réservées ou dérogations énumérées dans la présente déclaration de conformité.

Certifiées exactes les indications ci-dessus
I certify that the above is correct / Obige Angaben sie zutreffend bescheinigt

Date 28/07/15 Signature
Audrey BRUNEAU
TECHNICIEN QUALITE BARRES

(1) Autres éléments/other elements: Chaque/Each: ≤0,05% ; Total: ≤0,15% (2) L : Sens long LT : Sens Travers Long D : Début de Filage F : Fin de filage

S.A.S. au capital de 200.000 Euros
712 032 706 RCS NANTES , APE 2442Z
N° TVA CEE : FR 17 712 032 706
6 rue Pierre et Marie Curie - BP 700149 - 49245 MONTREUIL-JUIGNE CEDEX - (FR)

Usine -

Tél : 01.30.69.67.00
Fax : 01.30.50.93.46
Web : www.thyssenfrance.com Code NAF 515 C

Siret 562 068 155 00026
N° TVA FR30562068155

Nuance : 2024 T
Coule : M714890 lot : 8417
Commande : BL :689576 Poste:01
Client : THYSSENKRUPP CHRISTON
CDE 3BA 5403692811

THYSSENKRUPP MATERIALS FRANCE
Une entreprise de ThyssenKrupp Services

Constellium Montreuil-Juigne SAS

Certificat de réception et déclaration de conformité
Inspection certificate and statement of conformity
Abnahmeprüfzeugnis und Übereinstimmungserklärung
EN 10204-3.1 B - EN 10204-3.1

Commande client-Customer Order-Kundenbestellung	Destinataire - Consignee - Empfänger	Commande Constellium Aiastube
THYSSENKRUPP	THYSSENKRUPP	158718/ 100/ 1
		N° de PV
		128047

Alliage - Alloy - Werkstoff	Norme - Standard - Norm	Produit - Product - Produkt
2024	ASNA3551G MCT1023503 MDS	BARRE RONDE FILEE BN2985
Etat - Temper - Zustand	EN2633:1994 EN2318:1992 CCT LA 279/2	56,00 MM 3000 MM
T3511	PROCESS AIR9049	

Coulées - Castings - Schmelze

Composition chimique (% en masse) - Chemical Composition - Chemische Zusammensetzung (1)

Si	Fe	Cu	Mn	Mg	Cr	Ni	Zn	Ti	Zr	Pb			

Désignation des produits / Product description / Bezeichnung der Produkte
Observations - Dérogations/ Remarks - Derogations / Bemerkungen - Abweichungen

Liste des contrôles par lot - Inspection List per batch - Kontrollen für jedes los
** = Périodiques / Periodic / Periodische Tests

Colis 468303 M714890 521,000 KG 26 PCS
M714890 /8417 521,000 KG
Colis 468304 M714890 521,000 KG 26 PCS
M714890 /8417 521,000 KG

Résultats des essais - Test results - Zugversuche

N° de lot / Coulée / Etat de cuisse / Prélèvements N° sens-emplacement (2) épaisseur en/in/emax	Rm Tensile Strength N/mm²	Rp 0,2 Yield Strength N/mm²	A% Elongat %	Y sur épaisseur MS/m
LOT : M714890 /8419				
COULEE : R5219				
1 L D	564	441	14	
1 L F	564	446	13	
2 L D	569	451	13	
2 L F	564	442	14	
CONDUCTIVITE ELECTRIQUE :				
MINI : 16,7 MAXI : 17,2 MS/m				
CONTROLE MACROGRAPHIQUE				
--> RESULTATS CONFORMES				
CONTROLE US PRODUITS CORROYES				
--> RESULTATS CONFORMES				

Déclaration de conformité (NF L 00-015C)
Statement of conformity - Übereinstimmungserklärung

Nous déclarons que la fourniture citée est conforme aux exigences du contrat et qu'après vérifications et essais, elle répond en tout point, aux exigences spécifiées, aux normes et règlements applicables, sauf exceptions, réserves ou dérogations énumérées dans la présente déclaration de conformité.

Certifiées exactes les indications ci-dessus
I certify that the above is correct / Obige Angaben als zutreffend bescheinigt

Date 28/07/15 Signature
Audrey BRUNEAU
TECHNICIEN QUALITE BARRES

(1) Autres éléments/Other elements: Chaque/Each: ≤0,05% ; Total: ≤0,15% (2) L : Sens long LT : Sens Travers Long D : Début de Filage F : Fin de Filage

S.A.S. au capital de 200.000 Euros
712 032 705 RCS NANTES , APE 2442Z
N° TVA CEE : FR 17 712 032 705
6 rue Pierre et Marie Curie - BP 700149 - 49245 MONTREUIL-JUIGNE CEDEX - (FR)

Usine -

Tél : 01.30.60.67.00
Fax : 01.30.50.93.46
Web: www.thyssenfrance.com Code NAF 515 C

Siret 562 068 155 00028
N° TVA FR30562068155

D. Elliptical contact

All content of this appendix is summarized from the book of [Johnson, 1985]. Contact of two perpendicular cylinders with different radii, R_1 and R_2, (also incomplete and non-conformal) cannot be solved using analysis of half-planes as the line contact of a cylinder on a plane. Three dimensional analysis is required which makes the problem more complex. A special case rises and the problem becomes simple when radii of the two cylinders are equal, Figure . This contact configuration is equivalent to the contact between spheres since their contact shape is identical. It is a point when no load but spreads to be circular under loading. Otherwise, it becomes an elliptical contact under loading. Let a be major semi-axis and b the minor semi-axis of the ellipse. $R', 1/R'=1/R_{1x1}+1/R_{2x1}$, and $R'', 1/R''=1/R_{1x2}+1/R_{2x2}$, are major and minor relative radii of curvature. x_1 and x_2 are axes of the two cylinders.

The ratio of the major to minor semi-axis of the elliptical contact area can be estimated by equation (D-1).

$$a/b \approx \left(R'/R''\right)^{2/3} \tag{D-1}$$

Equivalent contact area, $c=(ab)^{1/2}$, is given by equation (D-2), where F_1 is a correction factor which can be determined from Figure D.2, and $R_e=(R'R'')^{1/2}$ is equivalent contact radius.

$$c = (ab)^{1/2} = \left(\frac{3PR_e}{4E^*}\right)^{1/3} F_1(R'/R'') \tag{D-2}$$

The maximum contact pressure can be calculated by equation (D-3).

$$p_0 = \frac{3P}{2\pi ab} = \left(\frac{6PE^{*2}}{\pi^3 R_e^{\,2}}\right)^{1/3} \left[F_1(R'/R'')\right]^{-2/3} \tag{D-3}$$

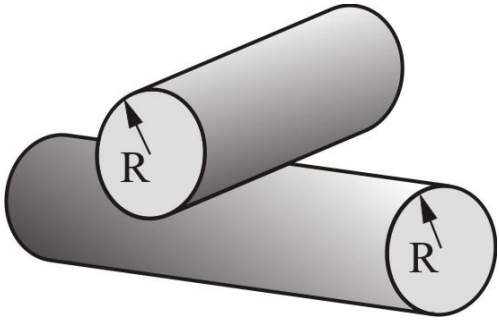

Figure D.1 Representation of a contact of two perpendicular cylinders
[Contact mechanics, 2017]

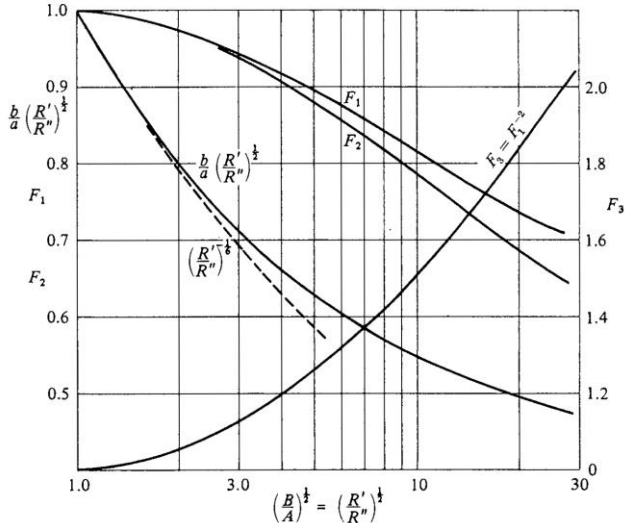

Figure D.2 Correlation between the ratio *R′/R″* and the correction factor F_1

References

Breitenstein, O., Warta, W., Langenkamp, M. (2010) *Lock-in Thermography, Basics and Use for Evaluating Electronic Devices and Materials*, Second. Springer Verlag, Heidelberg.

Contact Mechanics (2017) *Wikipedia*.

De Pauw, J. (2016) *PhD Dissertation: Experimental Research on the Influence of Palliatives in Fretting Fatigue*. Ghent University, Ghent.

Johnson, K.L. (1985) *Contact Mechanics*. Cambridge University Press.

Publications

List of scientific publications of Saosometh Chhith

A1– Peer reviewed journal publications included in Science Citation Index

Chhith, S., De Waele, W., and De Baets, P. "Rapid Determination of Fretting Fatigue Limit by Thermograhy." *EXPERIMENTAL MECHANICS (2017)*.

Talemi, RH, **Chhith, S.**, and De Waele, W. "Experimental and Numerical Study on Effect of Forming Process on Low-cycle Fatigue Behaviour of High-strength Steel." *FATIGUE & FRACTURE OF ENGINEERING MATERIALS & STRUCTURES* (2017): Vol. 40 (12), 2050-2067.

Chhith, S., De Waele, W., and De Baets, P. "On-line Detection of Fretting Fatigue Crack Initiation by Lock-in Thermography." *TRIBOLOGY INTERNATIONAL* (2017): Vol. 108 (SI), 150-155.

P1/C1– Conference proceedings

Somers, M., **Chhith, S.**, De Waele, W., and H. Talemi, R., Fatigue Fracture Assessment of High Strength Steel Using Thermographic Analysis, *International Journal of Sustainable Construction & Design* (2017): Vol. 8 (1), 8 pages.

H. Talemi, R., **Chhith, S.,** and De Waele, W. "On Effect of Pre-bending Process on Low Cycle Fatigue Behaviour of High Strength Steel Using Lock-in Thermography." *Procedia Structural Integrity* (2016): Vol. 2, 3135–3142.

Micone, N., De Waele, W. and **Chhith, S**. "Towards the Understanding of Variable Amplitude Fatigue." *Mechanical Engineering Letters* (2015): Vol. 12, 110–121.

Chhith, S., De Waele, W., and De Baets, P. "Detection of Fretting Fatigue Crack Initiation by Thermography." *Mechanical Engineering Letters* (2015): Vol. 12 36–42.

C3– Abstracts and posters

Chhith, S., Marnick, S., De Waele, W. "Fatigue Fracture Assessment of High Strength Steel Using Thermographic Analysis." *Second Structural Integrity* Seimnar (2017).

Chhith, S., De Waele, W., and De Baets, P. "On-line Detection of Fretting Fatigue Crack Initiation Under Perpendicular-cylindrical Contact by Thermography." *FEA PhD Symposium* (2017).

Chhith, S., De Waele, W., and De Baets, P. "On-line Detection of Fretting Fatigue Crack Initiation by a Lock-in Thermography." *International Symposium on Fretting Fatigue 8* (2016).

Chhith, S., De Waele, W. and De Baets, P. "On-line Detection of Fretting Fatigue Crack Initiation by Lock-in Thermography." *FEA PhD Symposium* (2015).

Chhith, S., De Waele, W., and De Baets, P. "Crack Initiation of Fretting Fatigue by Thermography." *FEA PhD Symposium* (2013).

Chhith, S., De Waele, W., and De Baets, P. "On the Applications of Infrared Thermography." *FLIR Seminar* (2013).